

New sensing platforms
based on nanoscopic devices
for probing protein-membrane interactions

Dissertation zur Erlangung des Grades
"Doktor der Naturwissenschaften"

am Fachbereich
Chemie, Pharmazie und Geowissenschaften
der Johannes Gutenberg-Universität Mainz

vorgelegt von

Cristina-Luminita Baci
geboren in Ploiești /Rumänien

Mainz, 2009

Dekan:

1. Berichterstatter:
2. Berichterstatter:

Tag der mündlichen Prüfung:

Contents

Introduction.....	7
Chap.1 Basic concepts	9
1.1 Biological membranes	9
1.2 Model lipid bilayer systems	11
1.3 Adsorption of proteins to lipid membranes	12
1.4 Analysis of equilibrium coverage fluctuations for quantification of reversible adsorption of proteins: a theoretical approach.....	13
1.5 When small is different: Localized Surface Plasmon Resonance (LSPR)	15
1.5.1 Absorption and scattering by small ellipsoidal particles	16
1.5.2 Nanohole plasmons in optically thin films	18
1.5.3 Beyond the quasi-static approximation.....	18
1.5.4 Shape dependence of the plasmonic particle resonance.....	19
Chap.2 Instrumentation.....	23
2.1 Atomic Force Microscopy (AFM).....	23
2.1.1 Basics.....	23
2.1.2 The cantilevers and the piezo scanners.....	24
2.1.3 The PID controller	24
2.1.4 Imaging modes	25
2.2 Ellipsometry.....	26
2.2.1 Basic principles	26
2.2.2 Nulling ellipsometry	28
2.2.3 Optical models for determination of ellipsometric thickness.....	29
2.2.4 Imaging ellipsometry	30
2.3 Epifluorescence and Confocal Microscopy	31
2.3.1 Fluorescence.....	31
2.3.2 Epifluorescence microscopy.....	32
2.3.3 Confocal laser scanning microscopy (CLSM).....	33
2.4 Dark field microscopy (DFM).....	34
2.5 Single particle spectroscopy.....	36
Chap.3 Materials and experimental procedures.....	37
3.1 Materials	37
3.1.1 Lipids	37
3.1.2 Proteins	41
3.1.3 Gold nanorods	42
3.2 Preparation of solid substrates for supported lipid membranes.....	44
3.2.1 Hydrophilization of the glass substrates and silica wafers	44
3.2.2 Functionalization with EDSPA.....	44

3.3 Formation of large unilamellar lipid vesicles (LUVs)	45
3.4 Formation of giant unilamellar vesicles (GUVs)	46
3.5 Microstructuring lipid membranes on solid supports	46
3.6 Fluorescence recovery after photobleaching (FRAP)	48
3.6.1 Experimental	48
3.6.2 Data analysis	48
3.7 Monte Carlo simulations	49
 Chap.4 Lipid bilayers on solid supports	 51
4.1 Formation of lipid bilayer patches on silicon dioxide substrates	51
4.2 Micro-domains and nano-domains in multicomponent lipid bilayers	55
4.3 Conclusions	59
 Chap.5 Reversible and irreversible adsorption of proteins	 61
5.1 Calcium-induced and annexin A1-induced clustering of acidic phospholipids in ternary lipid membranes	 63
5.2 Ellipsometric characterization of reversible adsorption of prothrombin on mixed anionic lipid bilayers	 65
5.3 Conclusions	70
 Chap.6 Fast imaging with conventional AFM for detecting surface coverage fluctuations: pitfalls and drawbacks	 71
6.1 Thermal drift and small scan areas	72
6.2 Image resolution and long-time imaging stability and repeatability	74
6.3 How fast? How long ? – a matter of the chosen system	76
6.4 Conclusions	78
 Chap.7 Nanostructuring Gold Surfaces	 79
7.1 Nanosphere lithography	80
7.2 Regular arrays of triangle shaped gold nanoparticles	81
7.3 Random arrays of nanoholes in thin gold layers	85
7.4 Conclusions	89
 Chap.8 Lipid membrane coated gold nanorods as sensing elements	 91
8.1 Self-assembling of gold nanorods on glass substrates	92
8.1.1 Immobilization of gold nanoparticles on amine-functionalized glass	92
8.1.1.1 Influence of CTAB on the particles' adsorption efficiency	93
8.1.1.2 Incubation time	93
8.1.2 Self-assembling of gold nanorods on hydrophilic glass surface	95
8.2 Lipid bilayer formation on glass substrates with gold nanorods	96
8.2.1 FRAP analysis	98
8.2.2 Imaging with AFM	100
8.3 Sensing the lipid membrane with single particle spectroscopy	102
8.4 Configurational limitations of membrane-nanoparticle interaction	105
8.5 Conclusions	109

Chap.9 Protein-membrane interaction probed by single plasmonic nanoparticles....	111
9.1 Sensing the adsorption of streptavidin to biotinylated lipid membranes	112
9.2 Detection sensitivity	114
9.3 Potential extension of the nanosensor applicability	115
9.4 Conclusions	117
Chap.10 Phase imaging with AFM reveals increased activity of PLA ₂ on highly curved membranes	119
10.1 Structure and function of phospholipase PLA ₂	120
10.2 Characterization of PLA ₂ activity with ellipsometry	121
10.3 Phase imaging with AFM.....	123
10.4 Conclusions	126
Chap.11 Influence of the nano-scale gold surface topography on the lipid vesicles adhesion.....	127
11.1 Introduction	127
11.2 Experimental	128
11.3 Results and discussion	129
11.4 Conclusions	135
Summary	137
Bibliography	139
A. Annexes.....	149
A1 Materials	149
A2 Instruments and auxiliaries.....	150
A3 Abreviations	151

Introduction

Multi-component lipid bilayers determine the basic structure of biological membranes. Their properties and interactions with different ions and molecules are essential for the well controlled interplay, material exchange and signaling between compartments performing different functions. The complexity of the biological membranes and their interactions with intra- and extra-cellular matrices makes direct investigations very difficult. Since their first implementation by McConnel^{1,2}, solid supported lipid bilayers have become the most commonly used experimental model systems for cell membranes due to their simplicity and capability to maintain excellent mechanical stability without losing their fluid nature. Moreover, the emergence of surface analytical techniques (e.g. SPR, AFM, QCM, ellipsometry), which allow the investigations of biosystems in physiologically relevant aqueous environments, actuated a growing interest in the development of biofunctionalized surfaces. A large variety of different model systems has been successfully established and the approaches include simple self-assembled lipid bilayers on various supports such as glass, metal electrodes, or semiconductors³. Lately, more advanced systems were created employing porous supports or using tethered lipids that allow functional insertion of membrane proteins⁴. Only few studies report on particles successfully covered with lipid bilayers^{5,6}. This is mostly because parameters such as membrane curvature and adhesion properties need to be carefully adjusted. High throughput screening devices required in the contemporary analytical chemistry for detection of non-covalent binding events rely heavily on the miniaturization of the sensing areas. It is in principle possible to extract relevant kinetic parameters, without interference with mass transport, from the analysis of coverage fluctuations in a small system that is inherently at equilibrium⁷. Nanoscale miniaturization is a requisite for the next generation of stochastic sensing on surfaces.

In this work I report on the creation of a nanosized and addressable sensing platform based on lipid membrane coated gold nanorods for detection of protein adsorption. Protein induced changes in the local refractive index at the membrane interface are recorded as resonance shifts of the plasmonic particles that are individually interrogated with dark field scattering spectroscopy. The motivation for single-particle based detection of membrane protein interaction is also provided by the possibility to simultaneously detect the nature of this interaction as a function of the lateral composition of the heterogeneous lipid membranes.

Lateral organization of cellular membranes plays important functional roles in several processes including trafficking and sorting of proteins. Despite numerous experimental and theoretical studies focused on the dynamic compartmentalization of natural membranes, there remain open questions (i.e. related to the size of domains^{8,9} or to the elusive nature of lipid rafts¹⁰⁻¹²). As the artificial lipid bilayers constitute tractable systems for understanding how the molecular association controls the domain formation and the

interaction with proteins, they have been extensively employed in the present experimental investigations.

This work is organized as follows: After a brief introduction of the basic concepts in Chap.1, I present the main experimental techniques, calculation methods and sample preparation procedures in Chap.2 and Chap.3, respectively.

In Chap.4, I analyze the formation of bilayer patches on oxidized silicon substrates and I approach the topic of lateral phase separation as a function of membrane composition. It is shown that, in the presence of divalent calcium ions, acidic lipids accentuate the tendency for phase segregation in gel and fluid phase lipid mixtures.

Adsorptions of two proteins annexin A1 and prothrombin to multicomponent lipid bilayers are investigated in Chap.5 by means of AFM and ellipsometry. I demonstrate the capacity of Annexin A1 to induce phase separation in membranes with low anionic lipid content and I characterize the adsorption kinetics of prothrombin.

The capability of a conventional AFM to detect surface coverage fluctuations for different adsorption kinetics of proteins is estimated by comparisons with results obtained from Monte Carlo simulations in Chap.6. The main pitfalls, drawbacks, and potential alternatives are presented.

The requisite of small sensing areas imposed by stochastic sensing on surfaces lead to the implication of nano-constructions such as plasmonic particles.

In Chap.7, colloidal nanolithography is employed to build plasmonic gold nanostructures on transparent substrates. Technical issues, mainly related to the optimization of the mask deposition, are successfully addressed such that extended arrays of nanoholes or truncated tetrahedron shaped particles are achieved.

In Chap.8 and Chap.9 I present the proof of concept for the construction of an optical biosensor using gold particles as sensing elements for monitoring lipid membrane mediated interactions. The factors that influence the deposition of gold particles on differently functionalized glass substrates as well as the conditions for successfully coating the nanorods with lipid bilayers are analyzed.

The hydrolytic activity of phospholipase PLA₂ is investigated in Chap.10 through complementary techniques such as AFM, fluorescence microscopy and ellipsometry. Corroborated evidence demonstrates the hypothesis of increased enzymatic activity of lipase on highly curved regions of the lipid membrane.

In Chap.11, I report on the experimental finding that topographic modifications on a nanometer scale of the gold surfaces change drastically the adhesion properties for large unilamellar lipid vesicles. This observation unravels, at least in part, the controversial question about the behavior of lipid vesicles on bare gold substrates. The possibility of assembling monolayers of lipid vesicles on gold surfaces decorated with gold nanorods can be exploited in new biosensing applications that involve the radiative decay engineering of plasmonic particles.

Chapter 1

Basic concepts

1.1 Biological membranes

Biomembranes are complex and dynamic structures which define the entity of cells and cytosolic organelles, displaying a large variety of functions that are essential for the viability of the cells. The main constituents of biological membranes are lipids and proteins hold together mainly by non covalent interactions. As amphipathic molecules, the lipids are arranged in a continuous double layer based on the propensity of the hydrophobic moieties to self associate via hydrophobic interactions and on the tendency of the polar head groups to interact with the aqueous environment (Fig.1.1). The presence of integral and peripheral proteins perturbs the regularity of this arrangement and induces changes in the surface topography and membrane dynamics. In turn, the lipids themselves regulate the location and the activity of many membrane proteins, and also define microdomains that serve as platforms for the interacting signaling proteins.

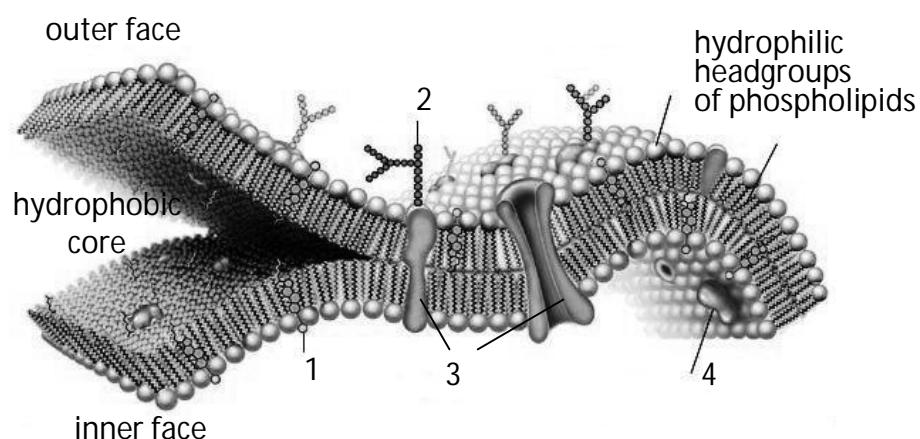


Fig. 1.1 Schematic of the cell membrane which is consisting of a double layer of phospholipids and cholesterol (1). Integral proteins (3) penetrate and bind tightly to the lipid bilayer while extrinsic proteins (4) are only loosely bound to the hydrophilic surface. Some of the intrinsic proteins exhibit sugar side chains (2) on the extracellular membrane surface.

In eukaryotic cells there are thousands of lipid species and they represent about 50% of the total mass of most animal cell membranes, the rest being represented by proteins. However, four major lipids are predominant in the plasma membrane of many mammalian cells: phosphatidylcholine (PC), sphingomyelin (Sph), phosphatidylserine (PS) and phosphatidylethanolamine (PE). Excepting the endoplasmic reticulum membrane, all the other biological membranes exhibit asymmetric lipid distribution between the two leaflets. For instance, plasma membrane of human erythrocytes displays Sph and PC mostly on the non-cytosolic side while the cytosolic leaflet is enriched in PS and PE lipids (Fig.1.2). This asymmetry has important functional effects. As an example, binding of the enzyme protein kinase C to the cytoplasmic face of the plasma membrane requires the presence of negatively charged PS lipids in order to act.

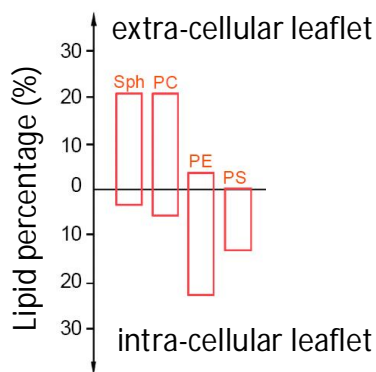


Fig.1.2 Asymmetric distribution of lipid membrane between the extra and intra cellular leaflets of human erythrocyte plasma membrane¹³.

Translocation of PS lipids to the cell surface may serve as susceptibility signal for phagocytosis or as a propagation signal in blood coagulation. The lipid quantity imbalance created across the bilayer and also lateral heterogeneities may contribute to the membrane bending that is required in processes (i.e. budding, tubulation, fusion or fission) that are essential for cell division and intracellular membrane trafficking.

Since biomembranes are fluid systems, the component lipids and integral proteins can diffuse laterally. These movements take place at a much higher rate than the flip-flop movements. As a consequence, certain lipids may segregate into transitory domains that exhibit different biophysical properties (i.e. different spatial arrangement, motional freedom, local curvature or surface electrostatics) with respect to the neighboring. These domains may recruit proteins from the cytosol that will subsequently organize secondary signaling or effector complexes.

Several proteins and enzymes are not permanently or intrinsically associated with the biomembranes. They can be extrinsically adsorbed, depending on the environmental conditions and on the composition, interactions or dynamic changes of the membrane topology. Protein adsorption may affect in turn the biomembrane organization and functionality

Numerous investigation techniques have been taking advantage of the simplicity of model membranes to address the complex topic of protein adsorption.

1.2 Model lipid bilayer systems

Direct investigation of biological membranes is very difficult due to their complexity and to their interactions with intra- and extra- cellular networks. Therefore, model bilayer systems have been created and largely employed in experiments aimed to understand and analyze biological processes that take place at the level of the native membranes. Such models of biological membranes include liposomes and giant vesicles in solution, supported vesicular lipid bilayers, lipid monolayers at the air water interface, black lipid films, surface confined lipid bilayers or freely suspended lipid membranes. Fig. 1.4 shows few examples of such model lipid bilayer systems. Solid supported lipid bilayers (SLB) are most commonly used model membranes because they offer excellent mechanical stability while maintaining their fluid character. SLB are also relatively readily achieved on large areas (few cm^2) of different support materials such as glass, silicon oxide, mica, (also gold or indium tin oxide in case of hybrid bilayers). Deposition of lipid vesicles on hydrophilic substrates leads to formation of two dimensional fluid bilayers of about 4-5 nm thickness, separated from the underlying support by a 5-20 Å thick layer of water (Fig.1.3).

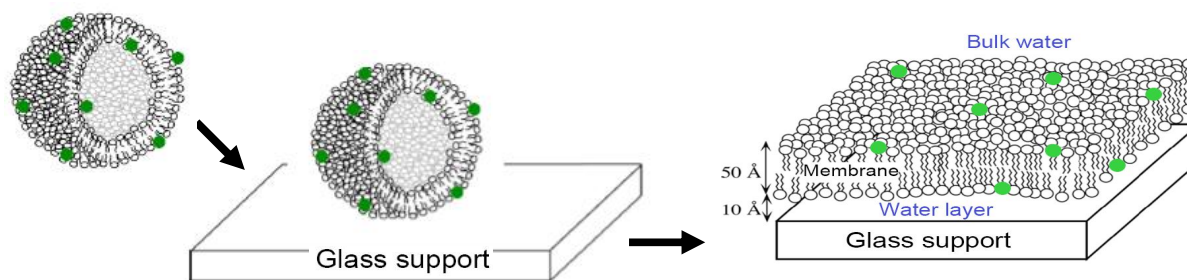


Fig. 1.3 Formation of solid supported lipid bilayers on glass substrates by vesicles fusion

The supported lipid bilayers offer the advantage of being feasible to several surface-sensitive inspection methods based on mechanical or optical principles such as atomic force microscopy (AFM), ellipsometry, surface plasmon resonance (SPR), etc. When proteins need to be incorporated into supported lipid membranes, an important drawback is represented by the potential direct contact between the substrate and peripheral portions of the bilayer integrated proteins. Such direct contact may be avoided by intercalating a polymer layer of typically less than 100 nm thickness that cushions or tethers the membrane.

Lipid bilayers can be micropatterned on their supporting substrates via different techniques such as micro molding in capillaries, micro contact printing, employment of wetting contrast or grid-like diffusion barriers. The possibility of constructing membrane arrays or individually addressable lipid bilayers offers attractive opportunities for biosensing applications and parallel screening of the membrane-active analytes.

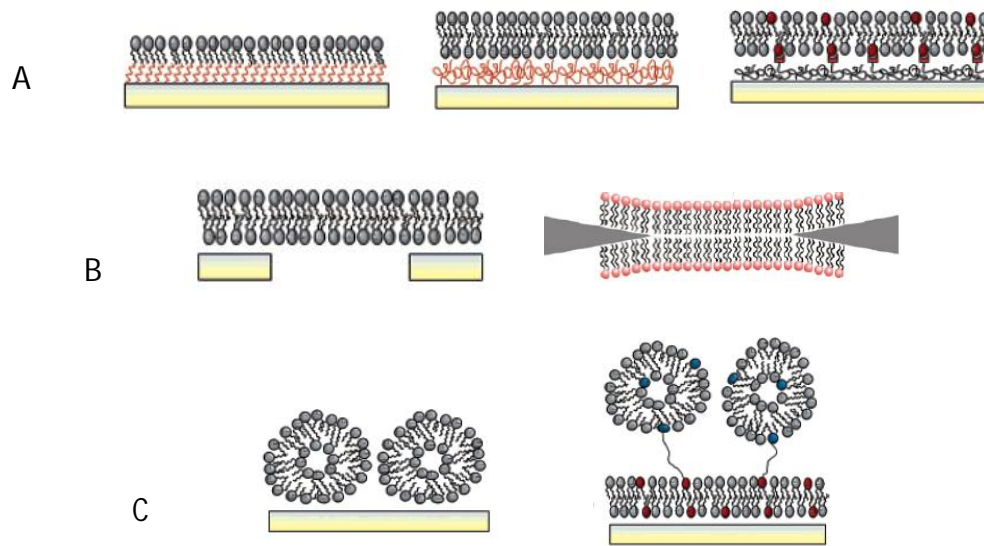


Fig. 1.4 Artificial lipid bilayers as models for biological membranes: A) surface confined lipid membranes (from left to right: hybrid bilayer, polymer-cushioned lipid bilayer, tethered lipid bilayer; B) freely suspended lipid bilayers (left) and black lipid membranes (right); C) supported vesicular layers. (schematic representation according to ^{14, 15})

1.3 Adsorption of proteins to lipid membranes

Proteins are major structural and functional components of the living systems. They fulfill a large variety of functions as receptors, enzymes, structural elements, intra- or extra-cellular signaling molecules. Proteins consist of one or several polypeptide chains, each of them being made of various combinations of 20 amino acids that define the protein primary structure. Either organized as alpha helices, beta sheets or random coils, the polypeptide chains define the three-dimensional structure which is essential for the protein functionality.

Adsorption of proteins to model lipid membranes is largely studied *in vitro* under well controlled conditions in order to understand the mechanisms of protein interaction with biological membranes. A large set of parameters that describe the protein (molecular shape, charge, size, conformation, interior stability), the ambient conditions (pH, ionic strength, temperature, etc), the membrane properties (fluidity state, compositional heterogeneity or surface charge distribution) play an important role in the adsorption process. The concentration of proteins in solution and their diffusion velocity influence the kinetics of the adsorption via mass transport effects and competition for the binding sites. The proteins may change their conformation during adsorption; they may remain adsorbed on the top of the membrane or insert them self into the hydrophobic part of the bilayer, forming channels or segregating into domains.

The driving forces of protein adsorption may have an enthalpic or an entropic character. Coulomb or van der Waals interactions between the proteins and the lipid bilayer lower

the enthalpy of the system ($\Delta H < 0$) while changes in the protein conformation or hydrophobic interactions with the membrane (via release of water molecules) may determine the increase of entropy such that the total free energy of the system is globally lowered ($\Delta G = \Delta H - T\Delta S < 0$). The reversibility of adsorption depends on the strength of interaction between the proteins and the membrane. For proteins adsorbing on solid interfaces, the interaction energies may range between $0.5k_B T$ and few $k_B T$ in case of electrostatic and van der Waals interactions, and from few $k_B T$ up to more than a hundred $k_B T$ when the hydrophobic interactions and protein conformational changes take place¹⁶.

Several experimental techniques have been used to study the kinetics of protein adsorption to lipid membranes, the most commonly used being the optical techniques (i.e. ellipsometry, surface plasmon resonance), the electrical methods (i.e. quartz crystal microbalance) or the spectroscopic techniques (i.e. infrared adsorption, Ramann scattering or fluorescence emission)

1.4 Analysis of equilibrium coverage fluctuations for quantification of reversible adsorption of proteins: a theoretical approach

Despite of their great diversity, the adsorption phenomena can be classified in two main categories, namely reversible and irreversible adsorptions. In an irreversible process, the interaction energy between the surface and the interacting macromolecules is much larger than the thermal energy $k_B T$ such that the molecules do not desorb and also do not diffuse along the surface. When reversibly adsorbed, the molecules/proteins can dissociate from the surface or diffuse along it, such that the system can explore all possible configurations and thus can be described in the framework of equilibrium statistical mechanics.

Adsorption kinetics of macromolecules on solid surfaces has been and is still usually described by the Langmuir model that was first introduced by Irving Langmuir in 1916. The model describes the kinetic law of a reversible adsorption as following¹⁷:

$$\frac{d\theta}{dt} = k_{on} c_p \varphi(\theta) - k_{off} \theta \quad (1.1)$$

where θ is the surface coverage of the adsorbing species p (in our case protein) having the concentration c_p in the bulk close to the adsorbing surface, k_{on} and k_{off} represent respectively the adsorption and desorption constants while $\varphi(\theta)$ denotes the available surface function accounting for the crowding of particles on the surface. For the system

described by the Langmuir model $\varphi(\theta) = \left(1 - \frac{\theta}{\theta_{max}}\right)$ where θ_{max} is the maximum

attainable surface coverage. Experimental studies on the kinetics of colloidal particle adsorption on planar surfaces demonstrated that Langmuir model accounts correctly only for the initial adsorption times^{18, 19}. The main limitations of the Langmuir model stem from the fact that the surface exclusion effects are not appropriately considered.

In 1939 Flory²⁰ has introduced the one dimensional Random Sequential Adsorption model (RSA) that was generalized by Widom²¹ for a space of dimension larger than one. In RSA model the particles are sequentially deposited onto the surface and the initial location of the deposition trial is chosen randomly and uniformly above the adsorbing surface. RSA model takes into account the surface exclusion effects. Assuming that the adsorbing particles are hard spherical objects, if they are also free to diffuse along the surface such that they organize themselves as hexagonal crystals, the maximum coverage is 0.91. If the particles can not move along the surface, the saturation coverage (or jamming limit) is reached at 0.547²². Studies on the kinetics of protein adsorption found that the experimental results are well described by Langmuir model, in agreement with RSA model, only at low bulk concentrations when the characteristic adsorption time is long compared to the characteristic diffusion time of the proteins, along the surface²³. Monte Carlo simulations also demonstrated that Langmuir model describes well the adsorption process if the surface coverage does not exceed 10%⁷.

When the system reaches the dynamic equilibrium, $d\theta/dt = 0$, that means that per unit time there are globally as much particles adsorbing as there are desorbing. In this stage, the mass transport phenomenon or depletion of the ligand in solution, factors that may influence dramatically the ascending part of the adsorption curve, are here unaccountable. Lüthgens et al. have proposed a new detection scheme for determination of the rate constants that are governing the adsorption process from the analysis of equilibrium coverage fluctuations⁷. By Fourier transformation of the fluctuating signal it was possible to extract precisely the rate constants k_{on} and k_{off} in the low- and intermediate- coverage regime. The authors proved theoretically the validity of this new approach with data supplied from Monte Carlo simulations that model the situation of a real experiment as close as possible. Fig.1.1a represents the coverage versus time of a reversible RSA simulation for which the mean equilibrium coverage was reached at $\langle \theta \rangle = 6.1\%$. Only the part of the curve that correspond to equilibrium coverage is subsequently used to calculate the Fourier transform of the signal $\theta(t) - \langle \theta \rangle$. The frequency response $\langle \delta\theta(\nu)^2 \rangle$ can be described by a single Lorentzian:

$$f(\nu) = c\tau / (1 + (2\pi\nu\tau)^2) \quad (1.2)$$

where the amplitude c and the time constant τ contain the kinetic parameters k_{on} and k_{off} . By fitting the power spectra (Fig.1.1b) with a Lorentzian (Eq.1.2) it is possible to extract the rate constants of adsorption and desorption from one single experiment, without any interference from mass transport, drift, depletion and high surface coverage. Moreover, as also shown in Fig.1.1b, the method allows the detection of the parameters of interest even for a high noise level, almost ten fold higher than the coverage fluctuations. This aspect is especially important since the instrumental noise is unavoidable in the real experimental detection of the small coverage fluctuations.

According to the scaled particle theory, the variance of fluctuations around equilibrium can be expressed by the equation^{24, 25}

$$\langle \delta\theta^2 \rangle = \frac{\pi a^2 \langle \theta \rangle (1 - \langle \theta \rangle)^3}{A (1 + \langle \theta \rangle)} \quad (1.3)$$

From this equation one can deduce that the highest fluctuations are found for a mean coverage $\langle \theta \rangle = 0.21$. Higher sensitivity, or with other words higher fluctuations

amplitude is reached for adsorbing particles with higher radius a and for smaller detection (adsorbing) areas A . It is therefore a prerequisite to conceive the experimental setup for recording coverage fluctuations as having very small sensing areas.

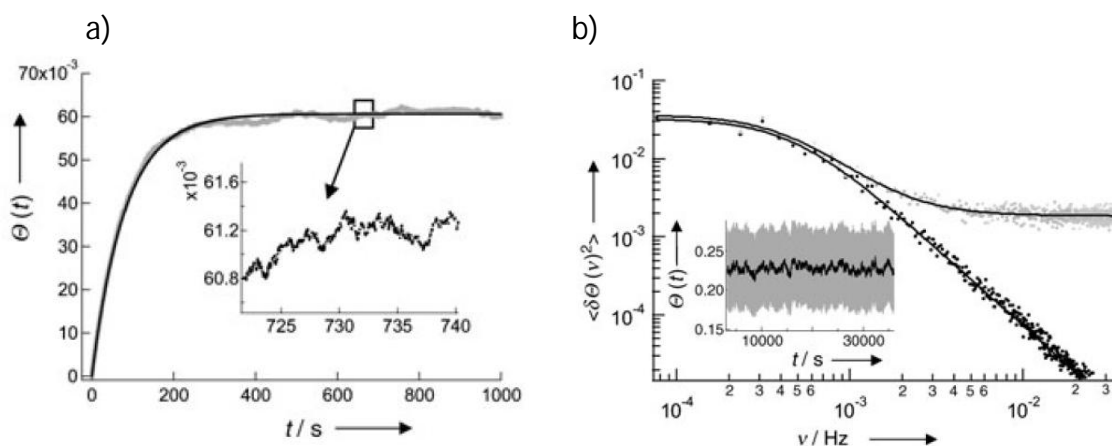


Fig. 1.5 a) Surface coverage versus time of a reversible RSA simulation for which the equilibrium coverage $\langle \theta \rangle = 6.1\%$ is reached. The inset displays a magnification of the equilibrium coverage fluctuations. b) Power spectra of equilibrium coverage fluctuations obtained from the data displayed in the inset. The fit of Eq. 1.2 are shown as solid lines. The black curve corresponds to the unperturbed signal while the gray curve corresponds to a signal with a noise level (white noise added) that is almost 7.5 fold larger than the coverage fluctuations (figures are reproduced from Luthgens and Janshoff, 2005).

1.5 When small is different: Localized Surface Plasmon Resonance (LSPR)

The extraordinary optical properties of gold nanoparticles interacting with light have been employed in this work in relation to the construction of a sensing platform for detection of protein adsorption on lipid membranes. Such optical properties of metallic nanostructures are due to the interaction between the metal conduction electrons and the electric field component of the incident electromagnetic radiation. When localized surface plasmons (SP) defined as collective surface charge density oscillations confined to the small particle volume are excited at the resonance wavelength, the particle exhibits properties that are not observed in the bulk material: intense and characteristic adsorption bands, strong scattering, and enhancement of the local electromagnetic field. The frequency and the intensity of the SP bands are characteristic to the type of material (i.e. gold, silver, platinum) and are highly sensitive to the size, shape and size distribution of the nanostructures as well as to the dielectric properties of the closely surrounding environment.

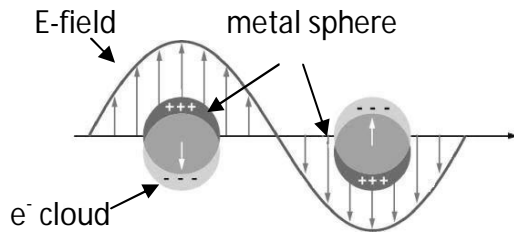


Fig. 1.6 Schematic of plasmon oscillations for a metallic nanosphere placed in an electromagnetic field, showing the displacement of the conduction electron cloud relative to the positive nuclear framework.

As compared to the propagating surface plasmons that may be generated at the planar metal-dielectric interfaces, the decay length (δ_{LSPR}) of the evanescent field of the localized plasmons is considerably smaller^{* 26}, fact that confers on the plasmonic particles highly localized refractive index sensitivities.

The basic principle for the detection of protein adsorption in Chap. 9 is based on the dependency of the SP resonance wavelength on changes in the refractive index in the immediate vicinity of gold nanoparticles coated with lipid membranes. The dimensions of the employed gold particles are larger than 10nm such that the extrinsic size effects dominate the plasmon resonance. In this case, the dielectric constant of the metal nanoparticle equals the bulk value $\epsilon(\omega)$. For very small particles ($2R < 10\text{nm}$), size dependent dielectric function $\epsilon(\omega, R)$, so called intrinsic size effects, have to be considered.

1.5.1 Absorption and scattering by small ellipsoidal particles

As long as the dimension "a" of a metallic nanoparticle interacting with an electromagnetic field is much smaller than the wavelength λ of the incident wave in the surrounding medium ($a \ll \lambda$), the phase of the harmonically oscillating field is practically constant over the particles volume. Under these conditions, the nanoparticle acts as an electric dipole, resonantly adsorbing and scattering electromagnetic fields. The dipole moment P induced inside of a particle by the external electric field is proportional to the magnitude of the electric field $|E_0|$ through the relation $P = \epsilon_m \alpha E_0$, where ϵ_m is the electric permittivity of the medium surrounding the nanoparticle. For an ellipsoidal particle with electrical permittivity ϵ , the polarizability α_i along one of its principal axis i is calculated, under quasi static approximation, according to the equation²⁷:

$$\alpha_i = 4\pi abc \frac{\epsilon - \epsilon_m}{3\epsilon_m + 3L_i(\epsilon - \epsilon_m)} \quad (1.4)$$

were a, b, c refer to the length of the ellipse along the i axes (see Fig.1.7) and L_i are the corresponding geometrical factors ($\sum L_i = 1$), related to the shape of the particle.

* δ_{LSPR} is ~5-15nm as compared to δ_{SPR} which is ~200-300nm

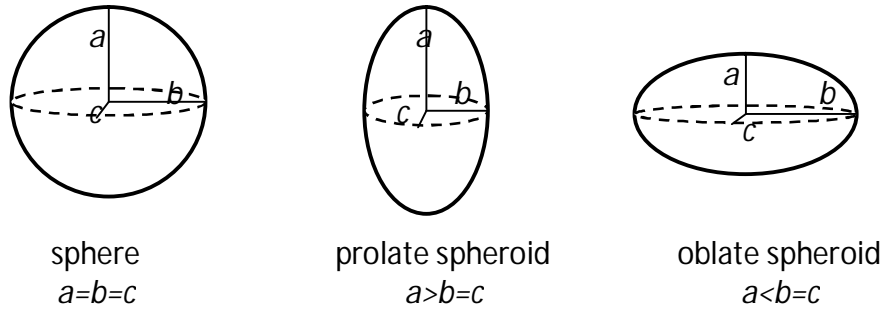


Fig. 1.5: Representation of the main axis for a sphere, prolate (cigar-shaped) spheroid and for an oblate (pancake-shaped) spheroid.

For a prolate spheroid ($a>b=c$), which is generally accepted (as well in this work) as a good approximation for the nanorod shape, the analytical expressions of L_i are functions of the aspect ratio a/b ²⁷:

$$L_x = \frac{1-e^2}{e^2} \left(-1 + \frac{1}{2e} \ln \frac{1+e}{1-e} \right) \quad (1.5)$$

$$L_{y,z} = \frac{1-L_x}{2} \text{ with } e^2 = 1 - \frac{b^2}{a^2}$$

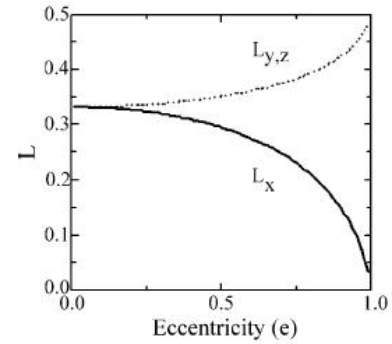


Fig. 1.6 Geometrical factors $L_{x,y,z}$ versus eccentricity e for a prolate ellipsoid

In the simplest case of a sphere ($e=0$), the geometrical factors $L_x=L_y=L_z=1/3$ and the expression for the polarizability α is reduced to $\alpha = 4\pi a^3 \frac{\epsilon - \epsilon_m}{\epsilon + 2\epsilon_m}$. In this case, the

polarizability experiences an enhancement under the condition $\text{Re}[\epsilon]=-2\epsilon_m$, known as Fröhlich condition for plasmon resonance of spherical particles.

Both, absorption and scattering cross sections are dependent on the nanoparticle polarizability thru the following equations:

$$C_{sca} = \frac{k^4}{6\pi} |\alpha|^2 = \frac{8\pi}{3} k^4 a^6 \left| \frac{\epsilon - \epsilon_m}{\epsilon + 2\epsilon_m} \right|^2 \quad (1.6)$$

$$C_{abs} = k \text{Im}[\alpha] = 4\pi k a^3 \text{Im} \left[\frac{\epsilon - \epsilon_m}{\epsilon + 2\epsilon_m} \right] \quad (1.7)$$

with $k=2\pi/\lambda$. For small particles ($a \ll \lambda$), the extinction cross section $C_{ext}=C_{sca}+C_{abs}$ is dominated by the absorption which scales with a^3 as compared to scattering that become significant with increasing particle size. According to the Eqs. 1.6 and 1.7 the plasmon resonance of nanoparticles characterized by the dielectric function ϵ is dependent on the dielectric properties (represented by ϵ_m) of the surrounding media.

As it results from Eq.1.4, a spheroidal nanoparticle exhibits two spectrally separated plasmon resonances, corresponding to the oscillations of the conduction electrons along the major and minor axis, respectively. The plasmon resonance along the major axis is visible in scattering and adsorption spectra as a sharp peak, the spectral position of which is strongly dependent on the dielectric properties at the nanoparticle interface. Considering the metallic particle according to Drude model and assuming negligible damping, the resonance wavelength along the major axis can be derived by minimization of the denominator in Eq. 1.4:

$$\lambda = \lambda_p \sqrt{1 + \varepsilon_m \left(\frac{1}{L} - 1 \right)} \quad (1.8)$$

Here, λ_p is the plasma frequency. According to the Eq. 1.8, the higher is the aspect ratio (smaller L) of the plasmonic particle, the greater is the sensitivity to the surrounding dielectric changes. The resonance wavelength is however shifting to larger values, towards IR, for particles with too large eccentricity and therefore, their visibility due to the color effects becomes less apparent.

The resonance wavelength increases almost linearly with the aspect ratio of the plasmonic particles and shifts to larger values with increasing refractive index of the embedding medium. The red shift of the resonance is due to the shielding of the surface charges caused by the polarization of the closely surrounding medium.

1.5.2 Nanohole plasmons in optically thin films

Pretty similarly to metallic nanoparticles, dielectric inclusions (of characteristic dimensions $a \ll \lambda$) in metallic structures can also support localized plasmon modes^{28, 29}. Experimental investigations performed by Prikulis et al. on two dimensional nanoholes in optically thin metallic films showed clear optical resonances in the visible to near-infrared range of the scattering and extinction spectra³⁰. The observed well defined excitation of single nanoholes and the similarity in their resonance behavior with Au nanodiscs conducted to the hypothesis that the hole resonance is a dipolar localized surface plasmon^{31, 32}. An exact electrodynamic calculation for holes in thin gold films is not yet available. However, in the quasi-static approximation, the resonance wavelength dependency of nanoholes in very thin films on the increasing aspect ratio (hole diameter divided by the hole depth) is similar to that of an oblate spheroid, in accordance with Eqs.1.4 -1.5. It was observed that, for nanoholes arranged in a short range ordered array, inter-holes electromagnetic coupling may occur only for average center-to-center distances smaller than 1 μ m. This coupling is expected to be rather mediated by launching surface plasmon polariton (SPP) in the thin metallic field than to be a radiative dipole coupling³³.

In Chap. 8, optimized conditions for the construction of extended areas of short range ordered arrays of nanoholes with different inter-holes spacing are presented.

1.5.3 Beyond the quasi-static approximation

The quasi-static regime previously considered is not justified for larger particles interacting with electromagnetic fields for that retardation effects over the particles

volume and higher modes of plasmon excitation cause significant spectral shifts and broadening of the resonances.

When the condition for the quasi-static approximation ($2\pi na/\lambda \ll 1$) is not fulfilled, a solution is offered, within the frame of electrodynamics, by Mie theory. This theory calculates the response of a metallic sphere (of any size) to the incident electromagnetic field by solving analytically the Maxwell equations with appropriate boundary conditions in spherical coordinates. The calculations use multipole expansions of the incident field and take into account the particle dimensions and the dielectric functions of the sphere material and of the surrounding medium. However, Mie theory calculations are restricted to neutral particles of spherical shape. The resonance energy of the metal sphere shifts to lower values for increasing particle sizes.

The plasmon resonance of particles beyond the quasi-static regime is damped by two competing processes: a radiative decay into photons which is dominating for larger particles, and a non-radiative decay process due to the absorption. The non-radiative decay is due to either interband or intraband excitations. Intraband excitations occur with the formation of electron-hole pairs within the conduction band while interband transitions represent the transitions of electrons from lower-lying *d*-bands to the *sp* conduction band. Dephasing of the coherent excitation and therefore broadening of the plasmon resonance is induced by both energy decay processes (radiative and non radiative) and also by pure dephasing processes represented by scattering events that do not change the electron energy but its momentum. However, it was shown that the contribution of these elastic collisions to the total dephasing time is generally very small³⁴.

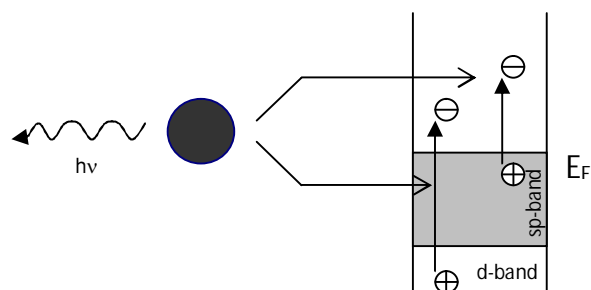


Fig. 1.7: Schematic of radiative and non-radiative decay of particle plasmons.

For particles whose sizes are significantly smaller than the electron mean free path (which is of the order of 30-50nm), an additional damping process called chemical interface damping occurs. This process is due to surface scattering that leads to additional collisions of the conduction electrons with a rate that depends on the particle radius ($\sim 1/a$) and on the Fermi velocity ($\sim v_F$). Besides the resonance broadening there is a spectral shift (either to blue or to red) in the resonance energy that depends strongly on the chemical terminations of the particle surface³⁵.

For even smaller particles (with radius of the order or below 1 nm), the notion of a plasmon as coherent electron excitation breaks down and the problem has to be treated in the framework of quantum mechanics.

1.5.4 Shape dependence of the plasmonic particle resonance

For particles of arbitrary shapes and/or surrounded by a complex environment, numerical methods such as discrete dipole approximations (DDA) make possible to

perform a quantitative evaluation of the optical response of the plasmonic particles. DDA method divides the particle of interest into a cubic lattice of finite polarizable points, each having a polarizability that is derived from the bulk dielectric constant of the particle material. The response of this lattice to an applied electromagnetic field is described by self-consistently describing the polarization induced in each element as a result of the interaction with the local field which is a sum of the incident field and a contribution from all the other dipoles in the particle. In this way one can determine the far-field properties such as absorption and scattering cross sections and also near-field properties like surface electric fields.

The particle shape effect on the spectral position of the plasmon resonance is shown in Fig 1.8, as it results from DDA calculations for a truncated tetrahedron and an oblate spheroid made of silver. The particles were chosen for comparison to have the same aspect ratio $b:a = 2:1$. The field polarization direction was taken along the major axis b . The truncated tetrahedron plasmon resonance is significantly shifted to a longer wavelength that is in fact similar to that of an oblate spheroid having the aspect ratio $5:1$ ³⁶.

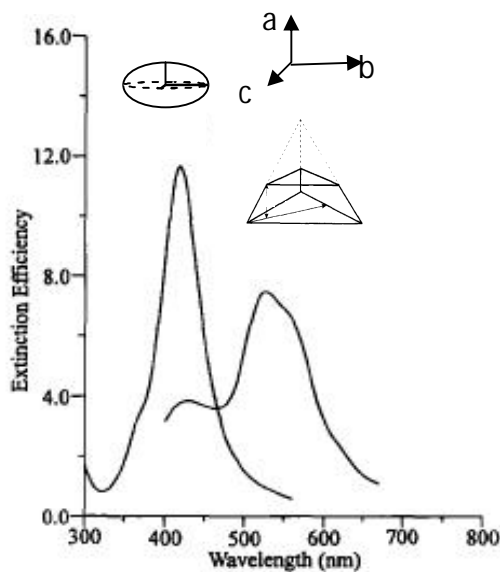


Fig. 1.8: Extinction efficiency calculated with DDA method (according to Jensen et al., 1999) for a truncated tetrahedron and for an oblate spheroid, made of silver. Both particles have the same aspect ratio $b:a=2:1$ and the field polarization is on the direction of the major axis b . The dimensions of the truncated tetrahedron are the length "a" of the perpendicular bisector on the opposite face and the distance "b" between the two parallel planes.

The optical field associated with the surface plasmon is strongest near the nanoparticle surface. This makes the resonance extremely sensitive to small changes in the refractive index at the particle interface, a property that can be used for various nanosensing applications. Jensen et al. has calculated the field enhancement around the plasmonic particle at the resonance which is dependent on the particle geometry. The representation of the electric field ($|E|^2$) contour for a sphere, a 2:1 spheroid and a truncated tetrahedron shows that the field is enhanced 500 times (compared to the incident plane value) for a tetrahedron and *only* 50 times for a sphere (Fig.1.9). The region of high field intensity is however localized at the high curvature periphery of the particle so, it is very much a local field effect. The drop in intensity to the asymptotic

value "1" vary from about 60 nm from the particle surface on the polarization direction to 15 nm on the perpendicular direction of polarization.

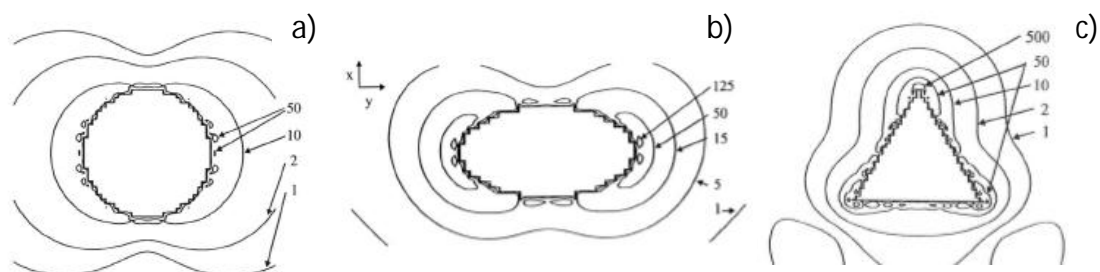


Fig. 1.9: Contours associated to $|E|^2$ at the particle plasmon resonance for different shapes: a) sphere; b) 2:1 spheroid; and c) truncated tetrahedron (views from the top). The contours labels are normalized such that the incident plane wave field is unity³⁶.

Superior enhancement of local fields around the truncated tetrahedron shaped like particles make them very attractive in biotechnological applications, (i.e. as sensing elements for ligand-receptor interactions). Spectroscopic measurements shown that the resonance wavelength sensitivity to changes in the refractive index of the surrounding environment for triangle shaped particles made of silver is about three times higher than the sensitivity of the gold nanorods, disks or nanoholes in optically thin gold layers, having comparable aspect ratios^{31, 37-39}.

Chapter 2

Instrumentation

A brief description of the main experimental techniques that were employed in this study is presented, with accents on the features that were mostly exploited.

2.1 Atomic Force Microscopy (AFM)

2.1.1 Basics

As a surface sensitive technique, AFM imaging is well suited to characterization with high spatial resolution (about 0.1 nm in the vertical direction and several nanometers in the lateral dimension) of flat and smooth surfaces such as supported lipid membranes or/and proteins adsorbed on these membranes. AFM does not require sample labeling or staining and most importantly, it is compatible with imaging in physiologically relevant aqueous environment.

Since 1986 when, following the invention of scanning tunneling microscopy (STM), Binnig and colleagues⁴⁰ announced the birth of AFM as a second member of the Scanning Probe Microscopy (SPM) family, AFM evolved as a powerful technique, that has been extensively applied both in industry and fundamental research. Atomic force microscopes allow surface topography imaging as a result of piezoelectric actuation combined with the sharpness of the scanning tip. The tip is mounted on a cantilever and is raster scanned over the sample surface (Fig.2.1). The small force of interaction between the tip and the sample is measured by sensing the reflection changes of a laser upon the cantilever movement. As the tip moves in response to the sample topography during scanning, the angle of the reflected laser beam changes, and so changes the laser spot position falling on the photodiode (position-sensitive detector). In the simplest operating mode, the cantilever deflection is maintained at a constant predefined level (force set point) by a control loop (PID controller) which moves the sample or the tip in the appropriate direction at each imaging point. The XYZ displacements of the piezoelectric scanner are recorded and displayed to produce an image of the sample surface.

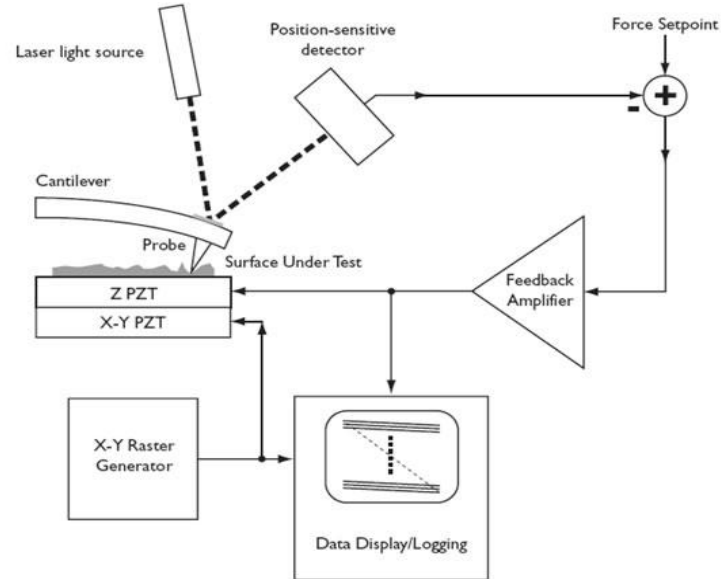


Fig. 2.1 Schematics of a basic atomic force microscope

2.1.2 The cantilevers and the piezo scanners

A low force of interaction of the scanning tip with the sample is crucial for imaging soft biological samples. Therefore, cantilevers with low spring constants are preferable. Silicon nitride (Si_3N_4) is generally used as a material for soft cantilevers. A cantilever with a high resonance frequency has a lower thermal noise density. Short cantilevers give higher optical deflection sensitivity. To minimize twisting or torsional motions of the cantilever whilst scanning the sample, the triangular geometry of the lever is suitable for purely topographic imaging. Rectangular cantilevers have a greater degree of rotational freedom and are more sensitive to the lateral forces if one wishes to measure frictional properties of the sample. The in plane resolution depends on the geometry of the probe that is used for scanning. In general, the sharper the probe is, the higher the resolution of the AFM image. The tip radius of curvature can vary between 2nm and 100nm. The vertical resolution is affected by relative vibrations of the probe above the surface. Sources of vibrations are acoustic noise, floor vibrations and thermal vibrations.

Piezoelectric scanners for AFM are constructed from amorphous PdBaTiO_3 . Their resonance frequency depends on their size and shape. Below the resonance frequency, the ceramic follows an oscillating frequency, at resonance there is a 90 degree phase change, and above there is 180 degree phase change. To a great extent, the resonance frequencies of the employed piezoelectric ceramics limit the scan rates of atomic force microscopes.

2.1.3 The PID controller

The feedback control circuit takes the input from the force sensor and compares the signal to a set-point value. The error signal (Z_{err}) is then sent through the proportional, integral, derivative (PID) controller that process it as follows:

$$Z_v = P Z_{err} + I \int Z_{err} dt + D \frac{dZ_{err}}{dt} \quad (2.1)$$

Appropriate selection of P, I, D terms allow tracking the surface with the tip during scanning. The integral term facilitates the probe moving over large surface features and the P and D terms allow the probe to follow the smaller, high frequency features. The Z_v output of PID controller drives the Z piezoelectric ceramic (Z PZT). When PID parameters are optimized, the error signal image will be minimal.

2.1.4 Imaging modes

AFM can operate in two modes: in *static-mode* (also named *contact-mode*) or in *dynamic-mode* (that can be either *non-contact* or *intermittent-contact*). The distance regimes for these operating modes are shown on the representation of the van der Waals force upon the interatomic distance between the tip and the sample, in Fig.2.2. In the contact regime, the cantilever is held less than a few angstroms from the sample surface; the interacting force is repulsive. In the non-contact regime, the cantilever is held on the order of tens to hundreds angstroms from the sample surface and the interacting force is attractive, mainly as a result of the long-range van der Waals interactions. Dependent on the ambient conditions (imaging in air or in liquid) and on the sample properties, other forces such as capillary forces or electrostatic forces may contribute to the tip sample interaction during the AFM operation.

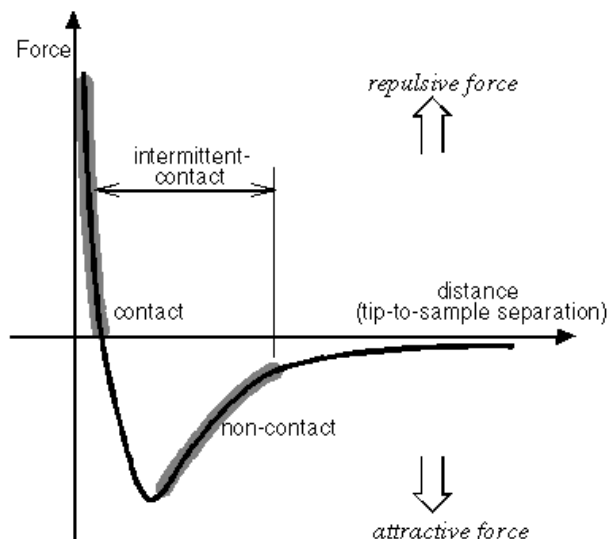


Fig. 2.2 The dependence of the van der Waals force upon the distance between the tip and the sample surface.

In the static (or contact) AFM mode the cantilever is in permanent contact with the sample. As the scanner gently traces the tip across the sample, the contact force causes the cantilever to bend to accommodate changes in topography. Once the AFM detects the cantilever deflections, it can generate the topographic data set by operating either in *constant-height* mode or in *constant-force* mode.

In constant-height mode the height of the scanner is fixed while the spatial variation of the cantilever deflection is used directly to generate the topographic data.

In constant-force mode the deflection is maintained constant by the feed-back circuit that moves the scanner along Z direction according to the sample topography.

In the dynamic AFM mode the cantilever is externally oscillated at or close to the resonance frequency. The oscillation amplitude, phase and resonance frequency are modified by the tip-sample interaction forces and these changes provide information about the sample topography. The most common scheme for dynamic-mode operation is the amplitude modulation for that the changes in the oscillation amplitude provide the feedback signal for imaging.

In non-contact mode the probe is vibrated above the adsorbed fluid layer on the sample surface (at about 50-150 Angstrom distance) and the topography of the sample is constructed by detecting the attractive van der Waals forces acting between the tip and the sample. The amplitude of the oscillations is typically lower than 10nm and stiff cantilevers must be used. The image has generally low resolution but the tip-sample interaction forces are very low (10^{-12} N) such that this mode is suitable for imaging very soft or elastic samples.

In the *intermittent contact* (called also *tapping*) mode the amplitude of cantilever oscillation is large (typically 100 to 200nm). In this mode the vibrating cantilever may overcome the capillary forces such that it can easily move in and out of the adsorbed fluid layer on the surface. The oscillating tip contacts alternately the sample surface and the reduction in the oscillation amplitude is used to identify and measure the surface features. The feedback loop adjusts the tip-sample separation to maintain constant amplitude and force on the sample. Tapping mode overcomes problems with friction and adhesion forces and allows imaging with high resolution of soft samples or samples that are loosely hold on their substrates.

2.2 Ellipsometry

Ellipsometry is a non invasive optical technique that allows the characterization of a range of properties of thin layers including the layer thickness, optical constants, anisotropy and uniformity. The method is based on polarization changes that occur upon reflection of polarized monochromatic light at an oblique incidence on the boundary between two (or more) media of different refractive indexes. These changes in the polarization state are expressed and quantified by the ellipsometric angles Psi (ψ) and Delta (Δ) that are measured and used in model calculations for extracting the relevant physical information about the sample.

2.2.1 Basic principles

When linearly polarized light reaches the interface between two media of different refractive indexes, the reflected light as well as the refracted light becomes elliptically polarized. The coordinate system used to describe the ellipse of polarization is the p-s coordinate system. Both p- and s-direction are taken to be perpendicular to the direction

of propagation. s-direction is parallel to the sample surface while p-direction is contained in the plane of incidence (Fig.2.3).

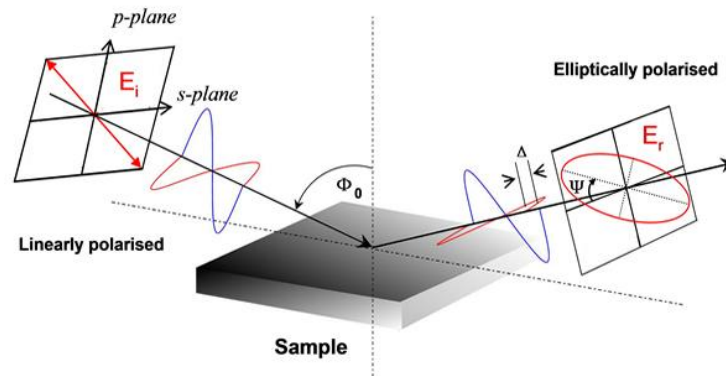


Fig. 2.3 Reflection of a linearly polarized light beam on a planar surface. The plane of incidence contains the normal to the surface as well as the incoming and outgoing light beams

The electric component of the electromagnetic wave can be represented by Jones vectors:

$$\vec{E} = \begin{pmatrix} |E_P| e^{i\delta_P} \\ |E_S| e^{i\delta_S} \end{pmatrix} = \begin{pmatrix} E_P \\ E_S \end{pmatrix} \quad (2.2)$$

where $|E_P|$ and $|E_S|$ are the amplitudes and δ_P and δ_S are the phases of the electric field decomposed on p- and s-directions respectively.

The state of polarization can be:

- linear, if $\delta_P - \delta_S = 0$ or $\delta_P - \delta_S = \pi$;
- elliptical, if $\delta_P \neq \delta_S$ and $|E_P| \neq |E_S|$;
- circular for the spherical case $\delta_P - \delta_S = \pi/2$ and $|E_P| = |E_S|$

The change in the polarization state upon reflection on a surface is dependent on the angle of incidence, the direction of polarization of the incident light, and the reflection properties of the surface. Incident and reflected electric vectors are connected by the reflection matrix R through the relation:

$$\begin{pmatrix} E_P^r \\ E_S^r \end{pmatrix} = \begin{pmatrix} R_{PP} & R_{SP} \\ R_{PS} & R_{SS} \end{pmatrix} \begin{pmatrix} E_P^i \\ E_S^i \end{pmatrix} \quad (2.3)$$

where i stands for incident and r for reflected. For isotropic materials, the matrix R is diagonal ($R_{SP}=R_{PS}=0$).

Ellipsometry is primarily interested in how p- and s- components of the electric field change upon reflection in relation to each other. The ellipsometric angle Ψ reflects the ratio of the amplitude change while Δ denotes the relative phase shift:

$$\Psi = \arctan\left(\frac{R_{PP}}{R_{SS}}\right) \quad \text{and} \quad \Delta = (\delta_P^r - \delta_S^r) - (\delta_P^i - \delta_S^i) \quad (2.4)$$

Typical samples in ellipsometry consist of various thin layers of different optical properties, covering a highly reflective surface. Multiple reflections at the interfaces of the layers superimpose to finally form the reflected light wave with an altered state of polarization. The elements of the reflection matrix R are defined by the square root of the Fresnel reflection coefficients that can be calculated as functions of the layer thicknesses.

Among the different ellipsometer arrangements, the most used are: null ellipsometer, polarization modulation ellipsometer, rotating polarizer/analyzer ellipsometer. The null ellipsometer operates by adjusting the orientation of the polarizer, compensator, and analyzer so that the light incident on the detector is extinguished or "nulled". In the configuration of the polarization modulation ellipsometer, a time dependent retarder (modulator) runs at very high speed allowing for very fast acquisition. The rotating polarizer/analyzer ellipsometer works without retarder with continuously rotating polarizer or analyzer. Different ellipsometer setups may combine the possibility to perform measurements at variable angles of incidence and at different wavelengths (spectroscopic ellipsometry). In particular, spectroscopic measurements provide information about the sample and also provide the ability to acquire data in the spectral regions where the measured data are most sensitive to the model parameters which are to be determined.

2.2.2 Nulling ellipsometry

The successful formation of solid supported lipid bilayers and their degradation under the activity of phospholipase as well as the kinetics of protein adsorption were ellipsometrically characterized by means of a commercially available ellipsometer (EP3-SW, Nanofilm, Göttingen, Germany) that has a nulling configuration, as presented in Fig.2.4. The ellipsometer is equipped with a Nd:YAG laser ($\lambda=532\text{nm}$) with adjustable power, a rotating polarizer (P) and a quarterwave plate (C) to get elliptically polarized light that is reflected from the sample surface resulting in linearly polarized light. The reflected beam is gathered by and analyzer (A) that is rotated to set the zero intensity (null). From the rotational position P and A, the ellipsometric angles ψ and Δ are calculated. The sample can be imaged with a CCD camera to that a 20x objective is attached.

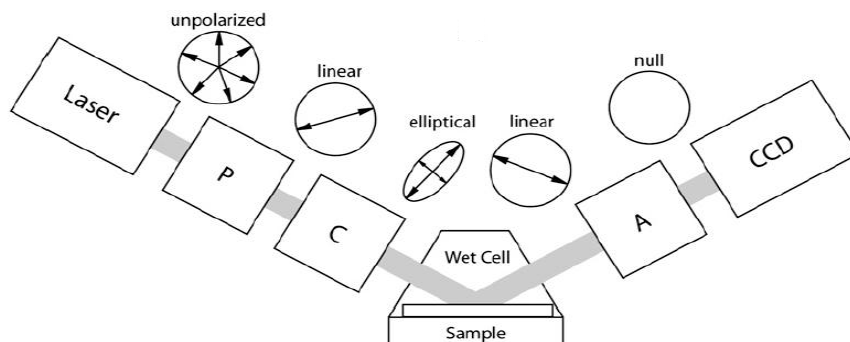


Fig. 2.4 Schematic representation of the PCSA (polarizer-compensator-sample analyzer) configuration of nulling ellipsometer

The measurements were performed at an incidence angle of 60° . For characterization under aqueous conditions, a fluid chamber made of teflon with glass windows was used. The ellipsometric nulling conditions are fulfilled at four distinguished optic settings in relation to the rotational positions of the polarizer and analyzer. The variation range of A and P as well as the relations for ψ and Δ corresponding to each nulling zone are presented in the following table:

zone i	P_i ($^\circ$)	A_i ($^\circ$)	C_i ($^\circ$)	Δ_i ($^\circ$)	ψ_i ($^\circ$)
1	(-45, 135)	(0, 90)	45	$270^\circ - 2P_1$	A_1
2	(135, 45)	(-90, 90)	45	$90^\circ - 2P_2$	$-A_2$
3	(45, -135)	(0, 90)	-45	$90^\circ + 2P_3$	A_3
4	(-135, 135)	(-90, 0)	-45	$270^\circ + 2P_4$	$-A_4$

The mean value at two- or four-zone measurements is free of multiple systematic errors and increases the accuracy depending on the measurement conditions by an order of magnitude.

In kinetic experiments, the monitoring of lipid bilayer formation and protein adsorption was performed by one-zone nulling procedure at an acquisition rate of 6 data points/min.

2.2.3 Optical models for determination of ellipsometric thickness

For calculation of film thicknesses, optical models were implemented based on classical electromagnetic theory and on the assumption that the sample consists of semi-infinite parallel slabs of homogenous composition described by a single set of optical constants (Fig.2.5). The amorphous silicon oxide and crystalline silicon phases as well as any adsorbed phase associated with the substrate were treated as optically isotropic and were assigned scalar optical functions.

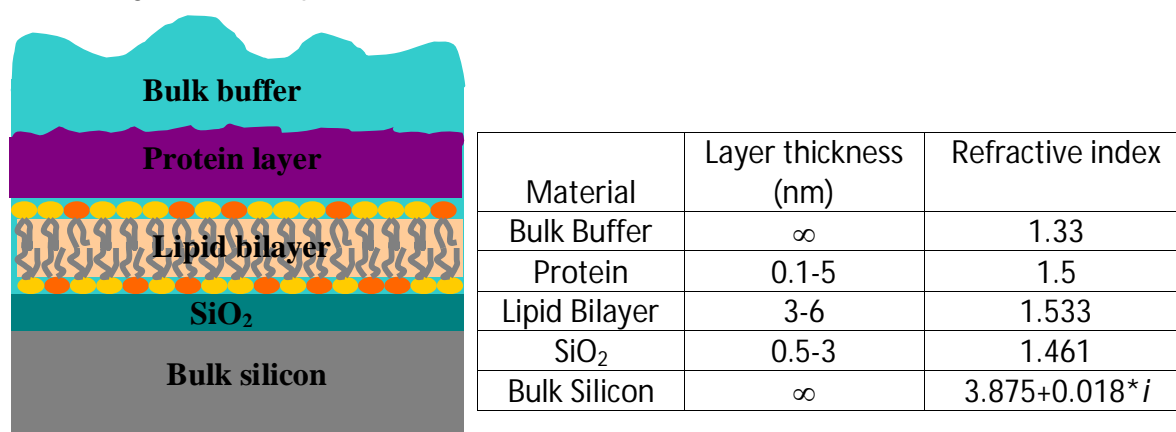


Fig. 2.5 left: Schematics of the parallel-slab optical model for the SiO₂/Si supported lipid bilayer on that a protein layer is adsorbed; right: Table with the possible range of values for the layer thicknesses and the corresponding refractive indexes of the applied materials used in the optical model as it is resulting from the literature⁴¹⁻⁴⁴.

The optical model simulates Δ and ψ as a function of the optical properties of the sample (fixed refractive indexes of the layers). The film thicknesses are determined through a fitting procedure that searches the best agreement between the simulated and measured values of Δ and ψ . The mean square error (MSE) of measured and simulated data averaged over n data points is minimized within the smallest number of iteration using the Levenberg-Marquardt algorithm⁴⁵.

For ultrathin films (<10 nm) like lipid membranes or protein layers, the ellipsometric angle Δ is more sensitive than ψ and has a linear dependency with respect to the layer thickness. Under these conditions the values of Δ alone are sufficient for determination of the film thicknesses within Angstroms accuracy from measurements performed at a single wavelength and fixed angle of incidence.

2.2.4 Imaging ellipsometry

The topography of samples that exhibit lateral structures can be resolved with imaging ellipsometry that operates on the principle of null ellipsometry and real-time ellipsometric contrast imaging. The ellipsometer is equipped with a sensitive CCD camera to that a motorized focusing mechanism is adapted such that a series of images with different foci can be recorded within the field of view. The images are then superimposed by digital imaging processing to obtain an overall focused image. In this way, contrast images appropriately focused can be generated at incrementally increased polarization angles. The areas of the sample surface that have different optical properties show null signals in the camera image at different polarization angles. By applying dedicated algorithms to the assemble of the recorded contrast images one can determine the null condition for each point comprised of a 2x2 region of pixels binned together. This yields a two dimensional map of the ellipsometric angle Δ that can be transformed into a thickness map of the sample, with 1 μ m lateral resolution (Fig.2.6).

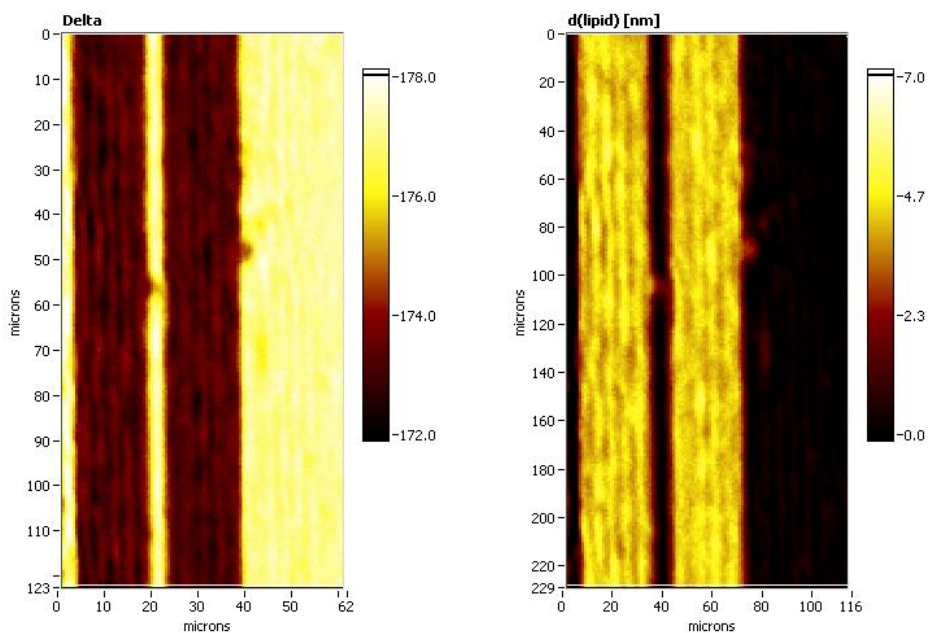


Fig. 2.6 Delta map (left) and the resulting thickness map (right) of POPC lipid membranes microstructured on Si/SiO₂ solid support. 5 μ m separates the lipid stripes of 15 μ m width.

2.3 Epifluorescence and Confocal Microscopy

Although the fluorescence microscopy cannot provide spatial resolution of specific specimen features below the diffraction limit, the detection of fluorescing molecules below such limits is readily achieved.

2.3.1 Fluorescence

Fluorescence is generated when a molecule, atom or nanostructure absorbs light at a particular wavelength and subsequently emits light of a longer wavelength. The energy gained by absorption of a photon causes the promotion of an electron on a higher electronic energy level (Fig. 2.7). The excitation happens in femtoseconds (10^{-15} s), while vibrational relaxation of excited state electrons to the lowest energy level is much slower and can be measured in picoseconds (10^{-12} s). The fluorescence occurs only as a result of electron transition from the lowest vibrational level of the singlet state S_1 to the ground state. This is because the higher singlet states (i.e. S_2) decay so rapidly by internal conversion that fluorescence from these states can not compete. Several other relaxation pathways that have varying degrees of probabilities may compete with the fluorescence emission process: non-radiative dissipation thru heat, collision with other molecules to that the energy is transferred, or intersystem crossing. The probability of intersystem crossing is however low because the molecules have to undergo first spin conversion to produce unpaired electrons. Transition from the excited triplet state to the ground state is accompanied by photon emission (so called phosphorescence process).

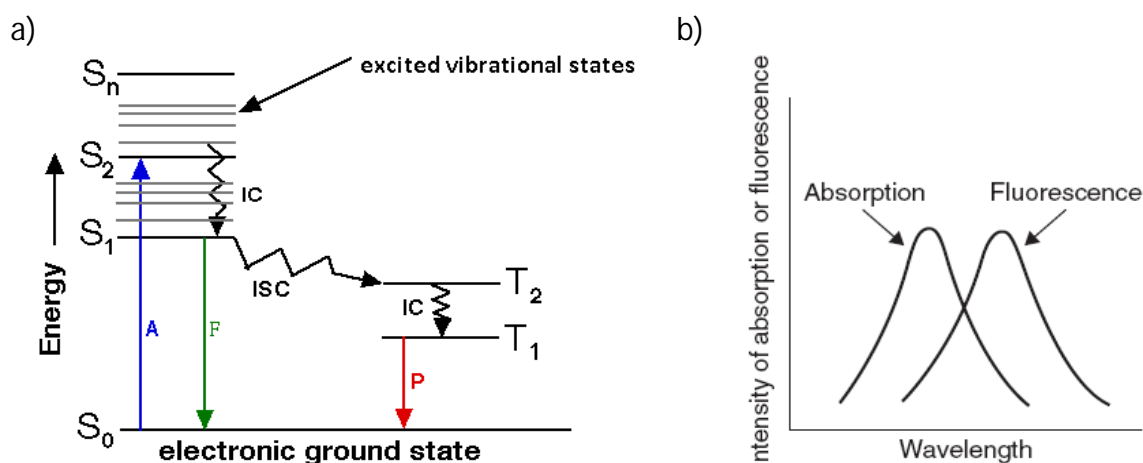


Fig. 2.7 a) Jablonsky diagram: S_0 is the electronic ground state, S_1 , S_2 , S_n are excited single states, T_1 and T_2 are excited triplet states. The electronic transitions are: A-absorption (10^{-15} s), IC-internal conversion and vibrational relaxation (10^{-14} - 10^{-11} s), F -fluorescence (10^9 - 10^7 s), P-phosphorescence (10^3 -100s), ISC-intersystem crossing; b) Absorption and emission spectra. Because some of the original radiant energy is converted to kinetic energy, the wavelength of the emitted photon is greater than the wavelength of the absorbed photon (Stokes' Law).

The ratio between the number of absorbed photons and the number of photons emitted by fluorescence is called the fluorescence quantum yield. The fluorescence quantum yield depends on the chemical nature of the fluorescing molecule, fluorophore or fluorochrome, on the excitation wavelength, and on other factors, including pH, temperature, hydrophobicity, and viscosity. The greater the fluorescence quantum yield, the better is the dye for fluorescence microscopy. The fluorescence quantum yield can be decreased by quenching or photobleaching. Quenching can be static or dynamic (collisional). A wide variety of elements or compounds behave as collisional quenching agents (i.e. oxygen, halogens, amines and many deficient electron organic molecules). They induce the decrease in fluorescence as a result of fluorophore transition from the excited state to the ground state through a radiationless pathway of energy transfer between molecules. In the static quenching, fluorescence emission is reduced without altering the excited state lifetime. This is because the population of active, excitable molecules is reduced due to the formation of non-fluorescent complexes between the quencher and the fluorophore.

In contrast to quenching, the bleaching results from the destruction of the molecule directly by light or through the light-induced production of free radicals. The average number of excitation-emission cycles that occur before bleaching depends on the molecular structure and the local environment of the fluorophore.

2.3.2 Epifluorescence microscopy

In fluorescence microscopy there are three methods of illuminating the specimen: bright-field, dark-field, and reflected light (or epi-illumination) method. The first two methods are either affected by low contrast (bright-field) or low resolution (dark-field) while the last, epi-illumination, permits high contrast and high resolution without compromise.

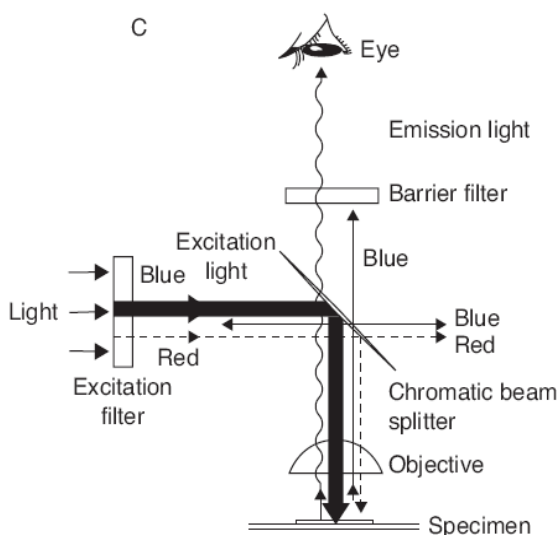


Fig.2.8 Diagram of the reflected light fluorescence microscope.

The fluorescence microscopes have to filter the fluorescence light which, is often extremely weak, from the excitation light. This filtering is done based on the difference in the wavelength between excitation and emission. In an epifluorescence microscope, the light filtering is accomplished by a chromatic beam splitter and a barrier filter. The chromatic beam splitter is an interference filter (tipped at 45° angle) that separates the excitation and emission light paths. Typically, it reflects about 90% of the light at wavelengths below the transition wavelength value and transmits 90% of the light at wavelengths above this value.

Ideally, the transition wavelength value (the cut off) is chosen to be between the wavelengths of excitation and emission. The fluorescent light that passes through the chromatic beam splitter is then filtered again by a barrier filter that further removes the excitation light. The more selective the filter, the dimmer the image is. Filters with different bandwidths (long pass filter, wide or narrow pass filter) are selected based on the tradeoff between brightness and selectivity. The numerical aperture of the objective lens is especially important in the epi-illumination mode because the objective lens is used both as condenser and objective. The brightness of the image depends on the fourth power of the numerical aperture divided by the square of the magnification.

2.3.3 Confocal laser scanning microscopy (CLSM)

Confocal microscopy offers several advantages over conventional widefield optical microscopy, including the ability to control the depth of field, elimination or reduction of the background information away from the focal plane and the capability to collect serial optical section from thick specimens.

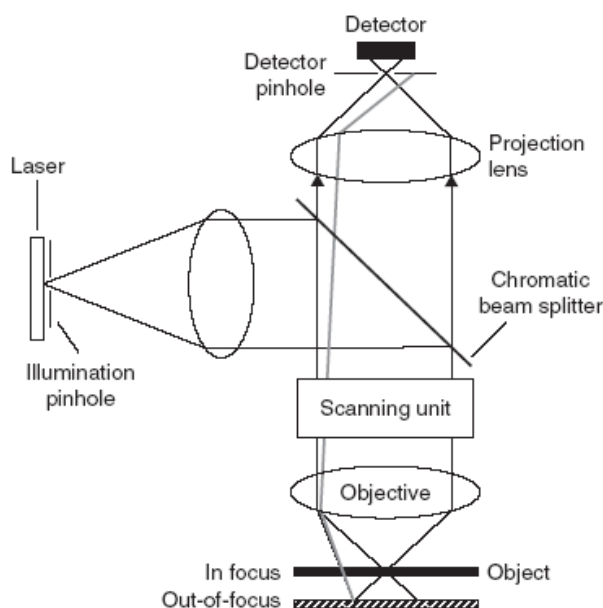


Fig. 2.9 Schematics of the confocal microscope.

The term confocal relates to the fact that the plane containing the illumination pinhole, the plane containing the specimen and the plane containing the detector pinhole are all conjugate planes (Fig. 2.9). Therefore, the image of the illumination pinhole is in focus at the specimen plane and at the detector plane. The confocal microscopes are typically used for fluorescence microscopy because the pinhole eliminates much of the out-of-focus fluorescence that reduces the contrast of images acquired with conventional microscopes. The image is created point by point from the scanned object. To accomplish this, lasers are used as very high intensity light sources such that the illumination time can be decreased.

The scanning is performed by moving the light spot across the specimen by means of a series of moving mirrors or slits in a rotating disk. The size of the field is limited by the objective lens. Because at any instant only one point of the specimen is observed, the detector is attached to a computer which builds up the image.

Since single point illumination scanning and single point detection are employed in a CLSM configuration, only the fluorophores in the shared volume of the illumination and detection point spread function can be detected. As a result, the lateral resolution defined as the separation of points required to produce acceptable contrast is about 30% lower in CLSM than in the widefield microscopes: $r_{\text{lateral}} = 0.4\lambda/\text{NA}$. Regardless of the

instrument configuration, the lateral resolution is proportional to the radiation wavelength (λ) and inverse proportional to the objective lens numerical aperture (NA). The axial resolution in CLSM is additionally dependent on the refractive index (n) of the specimen medium through the relation $r_{axial}=1.4 n \lambda / (NA)^2$.

When low numerical aperture and magnification objectives are employed, the image spatial resolution may be considerably improved in a scanning confocal microscope by utilizing the zoom factor. This feature offers the possibility to adjust the magnification electronically, by varying the area scanned with the laser. Reducing the specimen scanned area, the scanning rate is increased and therefore an increased number of samples along a comparable length are acquired which results in increased image spatial resolution.

In CLSM the detector needs to be highly sensitive to the incoming light since the use of the pinhole along with the preceding optics diminishes considerably the number of incident photons from the specimen. The fluorescence can be increased by dyeing the specimen with a larger concentration of fluorophores or by raising the intensity of the excitation light. However, at high concentrations, the fluorophores can quench each other. Increasing the excitation light leads to photobleaching. It is believed that this process occurs when the fluorescence molecules react irreversibly with oxygen and/or oxygen radicals. The reaction occurs after the fluorophore transition from the singlet to the triplet excited state characterized by much longer lifetimes and increased reactivity. One technique that takes advantage of the fluorescence photobleaching is FRAP (fluorescence recovery after photobleaching), technique that is typically employed to determine quantities such as the diffusion coefficient of the dye structures.

2.4 Dark field microscopy (DFM)

Dark field microscopy is often used to visualize individual objects which are much smaller than the limit of resolution. The visibility of such features is due to their light scattering abilities. While the resolving power (the capacity to distinguish two close objects as separate structures) is limited by diffraction, the minimal size of a single particle that can be detected is determined by the amount of contrast attainable between the object and the background. To obtain a maximal contrast, the rays that illuminate the object must be extremely bright and the zeroth-order rays (unscattered light) must not be collected by the objective lens. In dark field microscopy this can be achieved in two ways: either via reflected dark field illumination or via transmitted illumination.

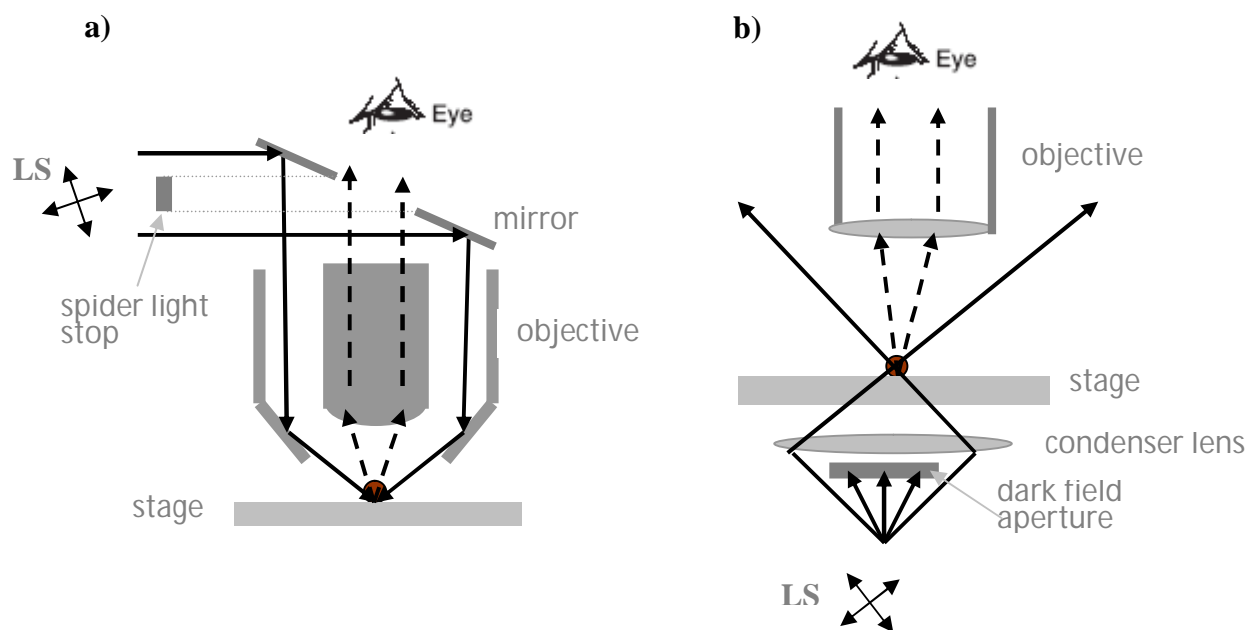


Fig. 2.10 Schematic of dark field microscopy in reflection (a) and in transmission (b).

A dark field microscope in reflection geometry requires especial objectives with significantly larger diameters that serve as two coaxially coupled but separated optical systems (Fig. 2.10a). The outer part of the objective functions as a dark field condenser and the inner part as a typical objective. The central portion of the light beam coming from the source is blocked by a spider light stop such that only a hollow cylinder of light enters through the periphery of the objective. Circular mirrors and prisms located at the bottom of the objective's hollow chamber transform the light into a hollow cone of illumination focused on the sample. Only light scattered from the specimen enters then the front lens of the objective and eventually reaches the eye or the camera. In the absence of the specimen, the viewfield is totally black. The main advantage of using dark field microscopy in reflection is given by the possibility to inspect non-transparent surfaces. Drawbacks are related to the low collection efficiency of the objectives and the need for additional adjustments to include the reflected light illuminator.

Dark field in transmission can be applied to transparent samples. Almost any bright field microscope can be used with dark field illumination in transmission by attaching a sub-stage dark field condenser (Fig.2.10b). The condenser blocks the central part of the illuminating beam such that only the oblique rays are emerging from the condenser and form a hollow inverted cone of light which is centered in the plane of the specimen. If the specimen is missing, the oblique rays travel further undeviated and do not enter into the objective because the objective is chosen to have a smaller numerical aperture than the numerical aperture of the sub-stage condenser. When the specimen is present, the scattered light enters the objective and therefore the specimen appears bright on a dark background. The contrast of the dark field images can be increased if the top lens of the sub-stage condenser is immersed in water or oil and an objective with low numerical aperture is used. In this way the illuminating rays are more oblique with respect to the optical axis of the microscope and the objective captures very less from the remnant background noise. For a better resolution, objectives with higher numerical apertures can be used.

2.5 Single particle spectroscopy

Scattering spectra of individual plasmonic particles can be recorded by means of a spectrometer attached to a dark field microscope (Fig.2.11). The sample is visualized under dark field illumination and the scattered light from the particles is directed either to the ocular or to the imaging spectrometer. The spectrograph can operate in imaging mode using a mirror instead of the grating such that one can identify and select the particles of interest. The selection can be performed either by closing the entrance slit of the spectrometer until only those particles that are to be investigated are visible or, by means of an electronically addressable liquid crystal device (LCD). The LCD replaces the entrance split of the spectrometer and act as a spatially addressable shutter. Each pixel of the LCD corresponds to one distinct point in the focal plan of the objective. On LCD the location of several particles can be simultaneously detected and the particles of interest are selected and measured by setting the corresponding pixels on transparent. Employment of a LCD eliminates the cumbersome procedure of selecting each particle by overlapping its position with the spectrometer slit and therefore the scattering spectra of several particles can be recorded faster, without additional adjustments ⁴⁶. In spectroscopy mode the light from selected particles is spectrally dispersed in the horizontal direction and read out by a CCD camera. The scattering spectra are generated by software integration of light from the region of interest for each selected particle. Each recorded spectra is corrected for the background and normalized to the spectral characteristic of the setup.

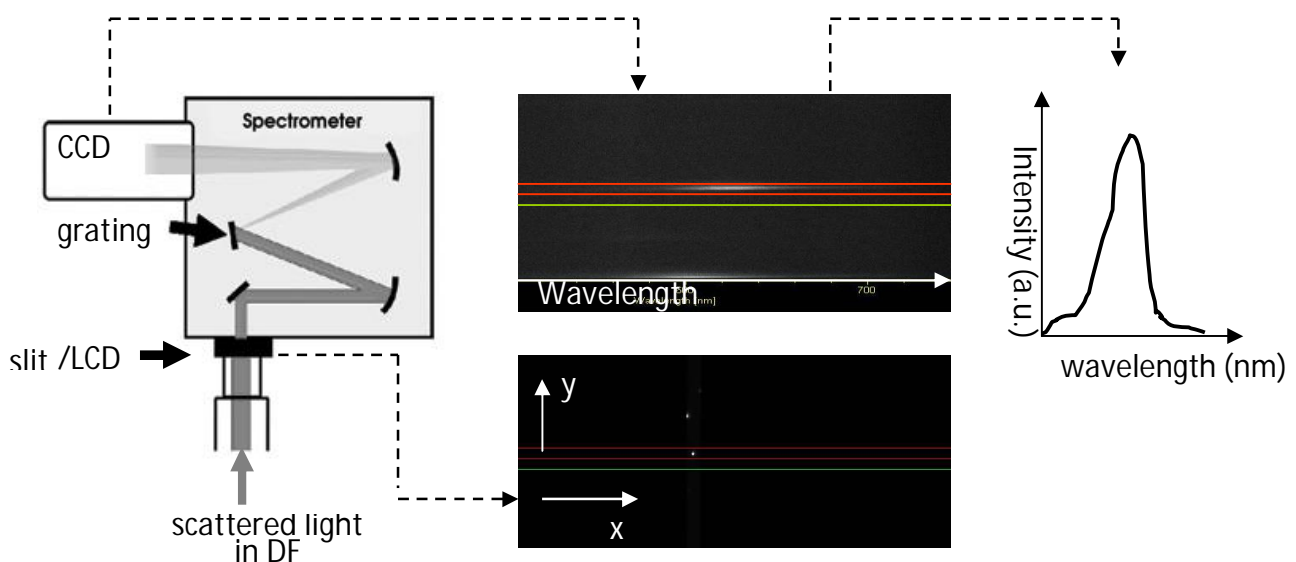


Fig. 2.11 Working principle for the dark field scattering spectroscopy of single particles: a) schematic of the imaging spectrometer that receive the scattered light from the attached dark field microscope; b) single particle (white dot on a black background) selected in imaging mode (here the selection is done by closing the entrance slit of the spectrometer); c) spectrally diffracted light of the selected particle. The region of interest is delimited by red horizontal lines; d) scattering spectra of the selected particle.

Chapter 3

Materials and experimental procedures

3.1 Materials

A succinct description of the materials (lipids, proteins and gold nanorods) used in this work is given. The rest of materials and their provenience are mentioned in Annex 1.

3.1.1 Lipids

The lipid composition of cellular and intracellular membranes is mostly represented by phospholipids, cholesterol and a small amount of glycolipids.

Most phospholipids are derived from glycerol and therefore they are also called phosphoglycerides. The only significant membrane phospholipid that is not a phosphoglyceride is sphingomyeline which is derived from the amino alcohol sphingosine. In phosphoglycerides, the three hydroxyl groups of glycerol are esterified to two fatty acids and to one phosphoric acid. The esterified phosphate forms an additional linkage with an alcohol that can be choline (resulting phosphatidylcholine, PC) serine (resulting phosphatidylserine, PS), ethanolamine (phosphatidylethanolamine, PE), etc. (Fig.3.1).

Glicolipids are lipids that contain sugars. They are derived from sphingosine and do not contain esterified phosphate.

Both phospholipids and glycolipids are amphipathic molecules. The fatty acid chains form the hydrophobic end of the molecule while the polar glycerol-phosphate-alcohol or sphingosine-sugar portion forms the hydrophilic end of the molecule.

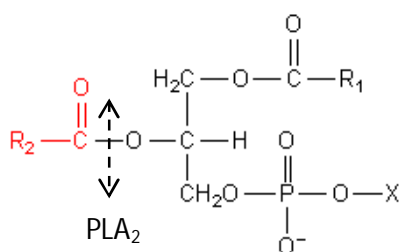


Fig.3.1 Phosphoglyceride structure: the hydrocarbon moieties R_1 and R_2 are esterified at sn-1 and sn-2 position of the glycerol backbone. The headgroup X is bound via a phosphoric acid ester to sn-3 position. Phospholipase PLA_2 may recognize specifically the sn-2 acyl bond of a phospholipid and catalytically hydrolyzes it releasing one fatty acid (red) and one lysolipid (black).

The enzymatic action of phospholipase PLA₂ on phospholipids may liberate fatty acids and lysophospholipids (Fig.3.1). Fatty acids are aliphatic monocarboxylic acids and can be either saturated or unsaturated. Some fatty acids (i.e. arachidonic acid) are important in cell signaling. Lysophospholipids are in fact phospholipids that are missing one of their two acyl chains. With a relatively large hydrophilic head group in relation to the hydrocarbon tail, lysolipid molecules tend to drive lipid assemblies into structures with increased positive curvature. When incorporated in lipid bilayers they induce packing stresses that may influence the conformation and the activity of membrane proteins, increase the membrane permeability, lower the electrical resistance or may even induce the membrane disruption.

From the physical point of view lipids are characterized by three structural features: 1) the size and electrical property of their head groups which may be charged (as PS, sulfolipids and some gangliosides), zwitterionic (as PC, PE, sphingomyelin) or neutral (as cerebroside or galactosides); 2) the number of carbon atoms (varying between 16 and 24 for the most abundant fatty acids) and the number of double bonds (ranging from 1 to 6); 3) the structural difference between the two acyl chains of each lipid.

Dependent of their structural features and in relation with the temperature and hydration conditions, the lipids can adopt various packing shapes, as shown in Fig.3.2. In a given solution environment, different lipids may be characterized by the packing parameter P expressed as the volume v of the hydrophobic tail divided by the product between the critical chain length l_c and the optimal cross-sectional area a_0 of the head group: $P = v / (l_c a_0)$. According to this parameter, the lipids may form spherical micelles (for $P < 1/3$), cylindrical micelles (for $1/3 < P < 1/2$), flexible bilayer (for $1/2 < P < 1$), planar bilayers (for $P = 1$) or inverted micelles (for $P > 1$)⁴⁷.

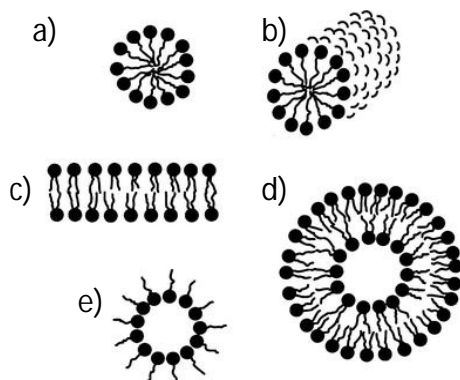


Fig. 3.2 Schematic of various structures formed by amphiphilic molecules depending on their critical packing parameter P : a) spherical micelle; b) cylindrical micelle; c) planar bilayer; d) flexible bilayer (vesicle); e) inverted micelle.

In lamellar phases lipid bilayers are repetitively stacked upon each other, being separated by water layers of defined thickness. At high temperature lipids are in *liquid-crystalline phase* (L_α). In this phase, individual molecules are highly mobile; they can rotate rapidly around their molecular axis and diffuse freely in the bilayer plane. The hydrocarbon chains of lipids show *trans-gauche* isomerization. Almost all biological membranes are in the liquid-crystalline state. When the temperature is lowered, ordered lamellar phases are formed, called *gel phases*. The gel-like behaviour is caused by predominant all-trans configuration of the hydrocarbon chains. The rotational motions and particularly lateral diffusion of individual lipids are reduced. Several lamellar gel phases are distinguished by

the orientation of the acyl chains with respect to the bilayer normal, by the packing of acyl chains, by the presence or absence of surface distortions or by the degree of hydration of the head groups. In Fig. 3.3 are illustrated the ripple gel P_{β} , the tilted gel L_{β} , and the lamellar crystalline gel L_c phases. With increasing temperature, some lipids (i.e. phosphatidylethanolamines) may change directly from L_{α} to L_{β} state, while other lipids (i.e. phosphatidylcholines) pass through intermediate phases like P_{β} .

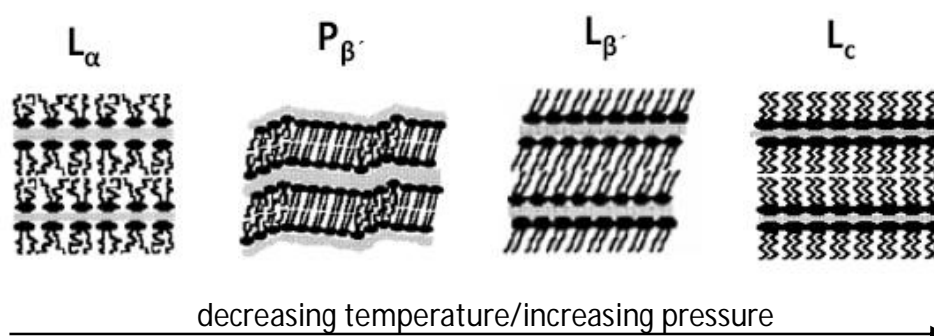
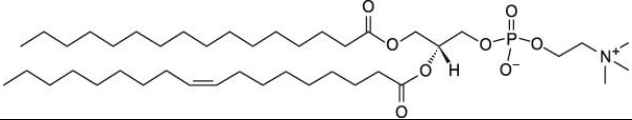
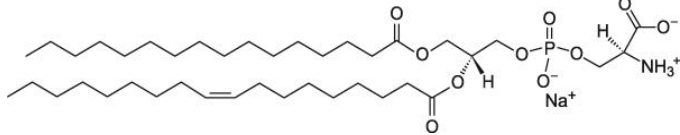
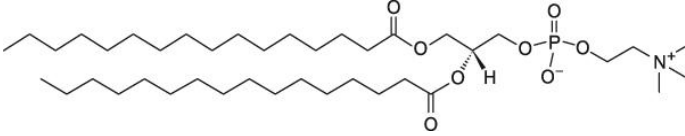
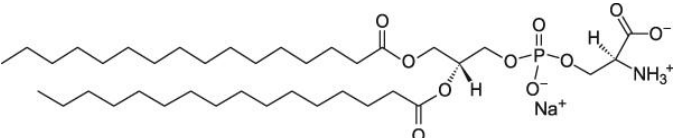


Fig. 3.3 Schematic illustration of different thermotropic phases of lipid bilayers.

The phase transition temperature is defined as the temperature required for inducing a change in the physical state from the ordered gel phase to the disordered liquid crystalline phase. The length of the acyl chains, unsaturation, charge and headgroups species affect the transition (melting) temperature of the lipids. Saturated lipids have a higher melting temperature because the residues will react with each other causing the acyl chains to be in a more rigid state. The specific type of double bonds also affects the melting temperature. *Cis* double bonds have a higher melting point compared to *trans* double bonds because they cannot pack themselves into a crystal as well as *trans* double bonds do. With increasing length of the hydrocarbon chains, the van der Waals interactions become stronger and require more energy to disrupt the ordered packing of lipids and therefore the transition temperature increases.

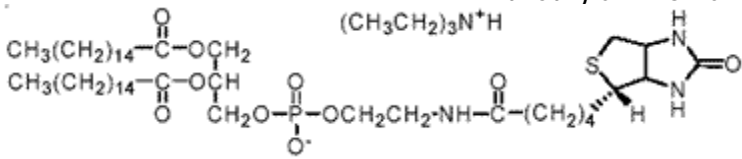
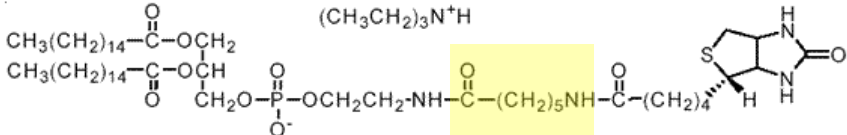
PC and PS lipids are major components of biological membranes and therefore they have been used in this study for the reconstitution of lipid membranes on solid supports. The primary role of PC lipids is to provide a structural framework for the membrane and to maintain the permeability barrier. The negatively charged PS lipids are important components of cell and blood platelet membranes. These lipids are typically located in the inner leaflet of the membranes. During platelet activation, PS is translocated from the cytoplasmic side to the plasma-oriented side where it facilitates assembly of the prothrombinase complex, a key element in the conversion of prothrombin to thrombin in the coagulation cascade. Unsaturated lipids with or without charged headgroups (POPS and POPC respectively) as well as uncharged saturated lipids (DPPC) and charged saturated lipids (DPPS) have been employed. The structure and the main transition temperature of these lipid molecules are given in Table 1.

Table 1

lipid	full name and structure	T _m (°C)	MW
POPC	1-palmitoyl-2-oleoyl- <i>sn</i> -glycero-3-phosphocholine 	-2	760
POPS	1-palmitoyl-2-oleoyl- <i>sn</i> -glycero-3-phospho-L-serine 	14	784
DPPC	1,2-dipalmitoyl- <i>sn</i> -glycero-3-phosphocholine 	41	734
DPPS	1,2-dipalmitoyl- <i>sn</i> -glycero-3-phospho-L-serine 	54	758

Biotinylated lipids, biotin-DHPE and biotin-X-DHPE, have been used for doping (up to 5% mol) the lipid membranes so that streptavidin molecules were subsequently adsorbed. The difference between biotin-DHPE and biotin-X-DHPE is represented by a seven-atom aminohexanoyl spacer between biotin and the reactive carboxylic acid. This spacer helps to separate the biotin moiety from its point of attachment, potentially reducing the interaction of biotin with the lipid to which it is conjugated and enhancing its ability to bind to the relatively deep biotin binding sites in streptavidin. The structures of the biotinylated lipids employed in this study are presented in Table 2.

Table 2

lipid	full name and structure	MW
Biotin-DHPE	<i>N</i> -(biotinoyl)-1,2-dihexadecanoyl- <i>sn</i> -glycero-3-phosphoethanolamine, triethylammonium salt 	1019
Biotin-X-DHPE	<i>N</i> -((6-(biotinoyl)amino)hexanoyl)-1,2-dihexadecanoyl- <i>sn</i> -glycero-3-phosphoethanolamine, triethylammonium salt 	1133

Fluorescently labeled lipids β -Bodipy C12-HPC and sulforhodamine-DHPE have been used for visualization of solid supported lipid membranes or of giant unilamellar vesicles with fluorescence microscopy.

Bodipy fluorophores are intrinsically lipophilic; they localize themselves readily in the membrane's interior. Excitation and emission wavelengths are 500nm and 510nm respectively. Despite their good photostability, bodipy lipids are useful for fluorescence recovery after photobleaching (FRAP) measurements of lipid diffusion

Sulforhodamine-DHPE lipids are labeled on the head group with the red-fluorescent rhodamine B fluorophore with excitation/emission maxima at ~560/580 nm.

3.1.2 Proteins

Three different proteins namely annexin A1, prothrombin and streptavidin have been employed in this study either to investigate the reversibility/irreversibility of protein adsorption to lipid membranes (the case of annexin A1 and prothrombin) or to probe the sensitivity of membrane coated plasmonic particles to the specific adsorption of proteins (the case of streptavidin).

Annexin A1 is a small protein (38kDa) preferentially located on the cytosolic face of the plasma membrane. Recombinant porcine annexin A1 was received from the group of Prof. Dr. Volker Gerke (Wilhelms University, Münster) where the protein was purified according to Rosengarth et al.⁴⁸. The protein purity was analyzed by SDS-PAGE and the concentration of proteins in solution was determined by UV absorption ($\epsilon_{280} = 0.6\text{cm}^2\text{mg}^{-1}$).

Prothrombin is a 72kDa vitamin K-dependent plasma protein which is synthesized in liver. Prior being secreted into plasma, prothrombin undergoes post translational modification by a vitamin K-dependent carboxylase which converts ten glutamic acid residues to γ -carboxyglutamic acid (gla). The ten gla residues are located within the first 40 amino acids of the mature protein and contribute to the ability of prothrombin to bind to negatively charged phospholipid membranes.

Both, annexin A1 and prothrombin adsorb to lipid membranes in a calcium dependent manner.

Streptavidin is a tetrameric bacterial protein (53kDa) produced by *streptomyces avidinii*. The protein consists of four identical units, each with one binding site for biotin. Crystallographic data indicate that the molecule has the dimensions 54/58/48Å⁴⁹. The high specificity and affinity of biotin-streptavidin binding offers an attractive system for studying the reaction between a receptor bound to a planar substrate (solid supported biotinylated lipid membranes) and a ligand (streptavidin) diffusing from the adjacent aqueous medium at the solid/solution interface. Neutron reflection and surface plasmon optical experiments demonstrate that streptavidin may form a well ordered protein monolayer with the biotin units of the functionalized lipids fully embedded into the binding pockets of the proteins⁵⁰. Ellipsometric characterization of streptavidin binding to biotin-functionalized lipid monolayers demonstrated that the kinetic parameters and the final thickness of the adsorbed protein monolayer are dependent on the phase state

of the lipids. Streptavidin binding is completely blocked if the lipids are in the solid-condensed phase⁵¹.

3.1.3 Gold nanorods

Among different synthesized nanoparticles, gold nanorods are of special interest due to their large amplitude of SPR whose spectral position can be tuned from visible to infrared by adjusting their shape and aspect ratio. As shown in Fig.3.4, the transmitted color of gold nanorods changes drastically for very small differences in the mean aspect ratio. The nanoparticles were imaged with transmission electron microscopy (TEM).

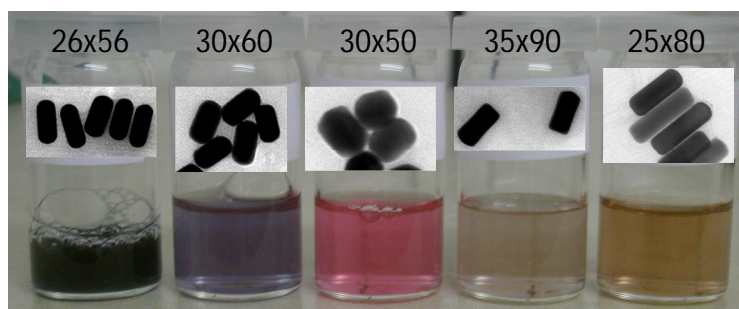


Fig. 3.4 Different colors are transmitted by suspensions of gold nanorods characterized by different aspect ratios. From left to the right, the aspect ratios are: 2.2, 2, 1.7, 2.6, 3.2, with the corresponding longitudinal LSPR wavelengths: 657nm, 628nm, 560nm, 695nm, 738nm, respectively. The insets are TEM images of the gold nanorods present in aqueous suspension.

One can observe that the longitudinal SPR wavelength shifts to the red with increasing aspect ratio of nanorods. The increase in the resonance wavelength is almost linearly dependent on the particles' aspect ratio⁵². The shape of nanorods, in particular the shape of the end caps has an important impact on the spectral position and amplitude of SPR⁵³. It has been calculated in DDA approximation that the red-shift and peak amplitude of the longitudinal SPR increase when flattening the nanorods caps, namely when nanorods evolve from prolate ellipsoids (I) to a quasicylinders (IV) keeping the same aspect ratio (Fig.3.5).

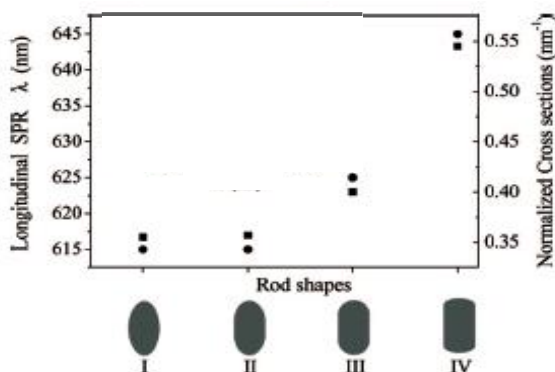


Fig. 3.5 Longitudinal SPR wavelength (dots) and peak extinction cross section per unit nanorod volume (squares) computed for four nanorod shapes (I-IV) that correspond to a total rod length of 30nm and a diameter of 15nm. The graphic is reproduced according to Muskens et al.⁵³.

For this study the nanorods were either supplied by Nanopartz (Concurrent Analytical Inc, Salt Lake City) or received from NanoBioTechnology group (Institute for Physical Chemistry, Mainz) who synthesized the nanoparticles using seed mediated growth method according to Nikoobakht⁵⁴. With this method, small spherical gold seed crystals are grown in a aqueous solution containing gold tetrachloride (HAuCl_4) and silver nitrate (AgNO_3) in sub-milimolar concentrations, a mild reducing agent (ascorbic acid) and a concentrated surfactant namely hexadecyl-trimethyl-ammonium-bromide (C_{16}TAB). The cationic surfactant adsorbs on the gold particles in a bilayer fashion and forms rod-shaped micelles acting as a template for the anisotropic particle growth. The seeds were initially produced by a rapid reduction of the gold salt (HAuCl_4) in aqueous solution with freshly prepared sodium borohydride (NaBH_4).

By controlling the growth conditions in the aqueous surfactant media it is possible to synthesize gold nanorods with tunable morphology. A fine tuning of the nanorods aspect ratio can be simply achieved by adjusting the amount of silver ions in the growth solution or, at a constant Ag^+ concentration, by adjusting the amount of seeds added to the growth solution⁵². It was observed that by altering the amount of ascorbic acid solvent one can modify the shape of gold nanoparticles from rod structures to dogbone-like structures⁵⁵. In Fig. 3.6 are shown TEM images of the nanorods resulted from slightly different preparations performed according to the seed mediated growth method. Bone-shaped gold nanorods (a), nanorods of various aspect ratios (b) or size and shape monodispersed nanorods (c) have been used for the experiments of the present work.

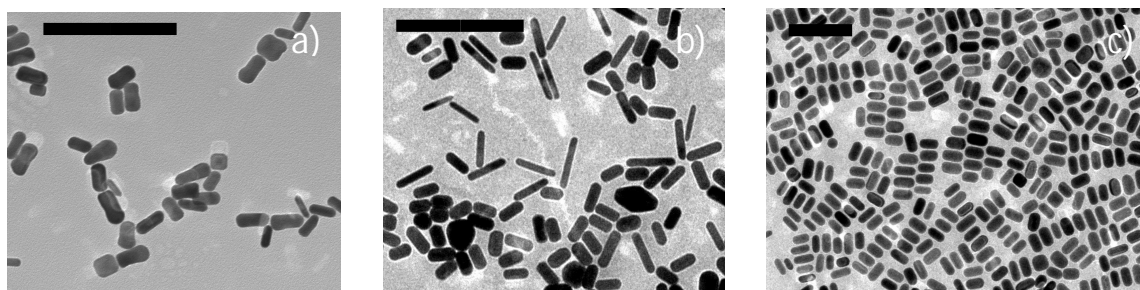


Fig. 3.6 TEM images of gold nanorods synthesized by seed-mediated growth method. Small variations in the preparation procedure determine changes in the nanoparticles geometry: a) backbone shaped nanorods; b) nanorods with large aspect ratio, c) nanorods with 26nm and 56 nm along the short and long axes respectively. The black scale bar stands for 200nm.

3.2 Preparation of solid substrates for supported lipid membranes

For ellipsometry and most of the AFM experiments the lipid membranes were supported on clean hydrophilic silica wafers while for microscopy (fluorescence, DFM) and single particle spectroscopy, transparent substrates such as hydrophilic or amine functionalized glass coverslips were employed. Colloidal nanolithography was performed on glass substrates previously treated in piranha solution.

3.2.1 Hydrophilization of the glass substrates and silica wafers

The glass coverslips were cleaned by sonication in 2% alkaline cleaning solution Hellmanex (Hellma, Müllheim, Germany) for 15 minutes followed by another two times sonication (15 minutes each) in fresh Milli-Q water. The hydrophilic properties of the glass surface could be preserved under Milli-Q water for at least two days.

The silicon wafers were first immersed for 15 minutes in diluted aqueous solution of hydrofluoric acid (1% v/v) and then rinsed thoroughly with Milli-Q water. A thin SiO₂ layer was formed on the surface of silica wafers by keeping them for 20 minutes in a mixture of NH₄OH/H₂O₂/H₂O (1:1:5, v/v) at 75°C. Afterwards the wafers were rinsed with Milli-Q water and used for experiments on the same day.

For colloidal lithography the glass coverslips were cleaned and rendered hydrophilic by treating them in a piranha solution (1:3 30% H₂O₂/H₂SO₄) at 80°C for 30 minutes. Once cooled, the glass slides were rinsed with copious amounts of water and used immediately for experiments.

3.2.2 Functionalization with EDSPA

The protocol of glass substrates functionalization with 3-Ethoxydimethylsilyl propylamine (EDSPA) was optimized to obtain flat surfaces and avoid polymerization of silane groups and multilayers formation.

Before functionalization with amine terminal groups, the glass coverslips were cleaned in piranha solution (1:3 30% H₂O₂/H₂SO₄) at 80°C for 30 minutes. Afterwards the substrates were thoroughly rinsed with Milli-Q water, dried under nitrogen stream and then immersed in a solution of 10% EDSPA in anhydrous ethanol for 15 minutes. Next, the glass coverslips were repetitively rinsed and washed by sonication in anhydrous ethanol (3X 15 min). Finally, the samples were baked for 3 hours at 120°C.

The formation of high quality EDSPA monolayers is important to prevent aggregation of subsequently adsorbed gold nanoparticles. AFM imaging indicates the absence of polymerized silane and shows that the roughness of the monolayer is lower than 1 nm (Fig.3.7)

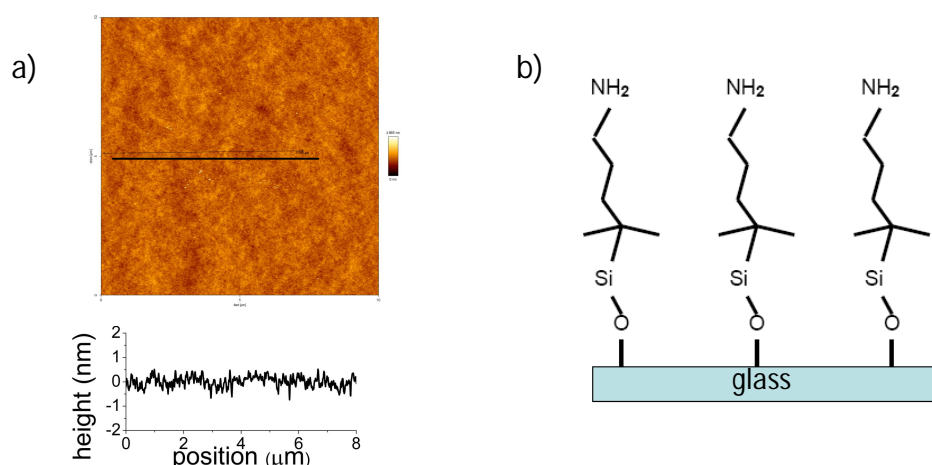


Fig. 3.7 a) AFM-CM image of a self-assembled monolayer of EDSPA on glass substrate cleaned with piranha. The line cross section shows a surface roughness lower than 1 nm. b) Schematics of the hydrophilic glass substrate that was functionalized with amine terminal groups (3-ethoxydimethylsilyl-propylamine)

3.3 Formation of large unilamellar lipid vesicles (LUVs)

Large unilamellar vesicles (LUVs) were prepared by extrusion method⁵⁶ and used to form supported lipid bilayers. The lipids were dissolved in chloroform or in methanol/chloroform (3:1 v/v) and mixed to obtain the desired proportions and compositions required by the experiments. The mixtures were afterwards dried under nitrogen stream followed by desiccation for 3 hours in vacuum to remove any trace of organic solvent. The resulted lipid films were hydrated in buffer (20 mM Tris/HCl, 100 mM NaCl, 1mM CaCl₂, pH 7.4) for about 15 minutes and the lipid suspension was then vortexed five times for 20s, every five minutes, to form multilamellar vesicles (MLV).

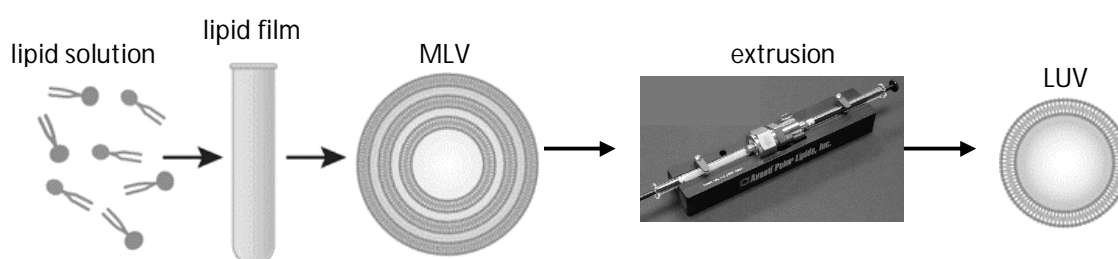


Fig. 3.8 Formation of large unilamellar vesicles (LUVs) by extrusion method (see text).

Using a LiposoFast miniextruder (Avestin, Ottawa, Canada) the resulting suspensions of vesicles were extruded by passing them 31 times through a polycarbonate membrane (100 nm pore diameter). The vesicles suspension was extruded at a higher temperature than the main transition temperature of any of the component lipids. In this way LUVs vesicles were formed (the final concentration of lipids was usually 1mg/ml).

3.4 Formation of giant unilamellar vesicles (GUVs)

Large unilamellar vesicles were obtained in two ways, either by “the gentle hydration method” or by “the solvent evaporation method” as described by Bagatolli⁵⁷ and by Moscho⁵⁸ respectively.

Briefly, for the gentle hydration method the lipids were dissolved in chloroform and mixed in the desired ratio in a glass vial. The solvent was afterwards completely evaporated under the nitrogen stream and by desiccation in vacuum for three hours. The formed lipid film (0.4 mg) was gently hydrated in 2 ml buffer (100mM NaCl, 20mM Tris-Cl, 1mM CaCl₂ pH=7.4) over the night, at a temperature higher than the main transition temperature of any of the component lipids. Resulting GUVs were observed with fluorescent light microscopy or/and bright field microscopy.

For the solvent evaporation method the desired mixture of lipids in chloroform was additionally mixed with Milli-Q water (1:8 v/v). The sample was transferred to a round-bottom flask that was placed simultaneously into a rotary evaporator (Büchi) and a water bath at (55°C). After 4 min evaporation of the organic solvent the lipid suspension became opalescent and GUVs are formed.

Solvent evaporation method generates mostly large vesicles, with diameters larger than 20µm while gentle hydration method provides vesicles with variable diameters up to 20µm. Multilamellar vesicles or vesicles exhibiting internal structures are observed in the GUV suspensions obtained with either of the two methods (Fig. 3.9).

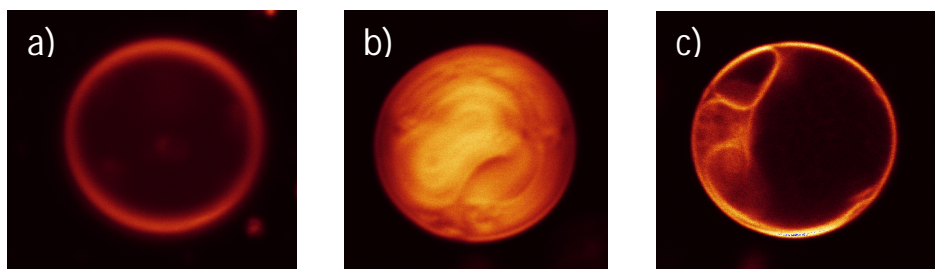


Fig. 3.9 Giant unilamellar vesicle (a), giant multilamellar vesicle (b) and giant vesicle exhibiting diverse internal structures; here the vesicles (POPC/POPS 4:1) are fluorescently labeled with sulforhodamine DHPE and visualized in CLSM.

3.5 Microstructuring lipid membranes on solid supports

The formation of individually addressable micropatterned solid-supported lipid bilayers was achieved by means of micromolding in capillaries according to the method described previously⁵⁹.

Briefly, polydimethylsiloxane (PDMS) stamps were formed by pouring the degassed resin into metallic frames placed on a silicon wafer displaying the inverted master structure (Fig.3.10). PDMS was formed by mixing in the ratio 10:1 two components of Sylgard 841 silicon elastomer kit (Dow Corning), namely the liquid PDMS prepolymer and a curing agent containing a platinum complex and copolymers of methylhydrosiloxane and

dimethylsiloxane. After 4 hours at 65°C the PDMS was vitrified and the stamps with the relief pattern were released from the metallic shapes and exposed to oxygen plasma for 2 min (with Plasma Cleaner, Harrick, NY). Plasma oxidation renders the PDMS surface hydrophilic and in this way water wetting is facilitated as well as the seal formation between the stamp and the substrate.

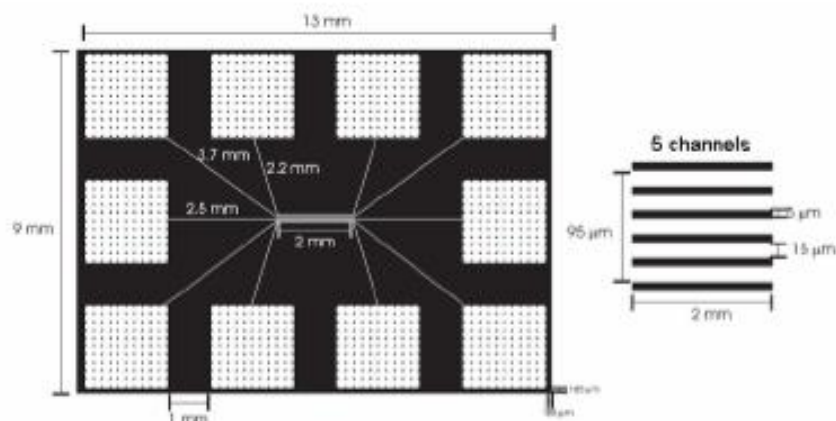


Fig.3.10 The master structure in a silicon wafer that was used for preparation of hydrodynamically coupled networks of capillaries in PDMS stamps.

By conformal contact between the PDMS mold and the hydrophilic substrate (glass or clean silicon oxide) capillaries were formed and individually filled with 0.4 μl suspension of LUVs (0.5 mg/ml) of the desired lipid composition. The vesicles adsorption and rupture induce the formation of supported lipid bilayer stripes confined by the geometry of the capillaries. After 10 minutes the PDMS stamp was removed and the surface was extensively rinsed with buffer to flush the excess of lipid vesicles.

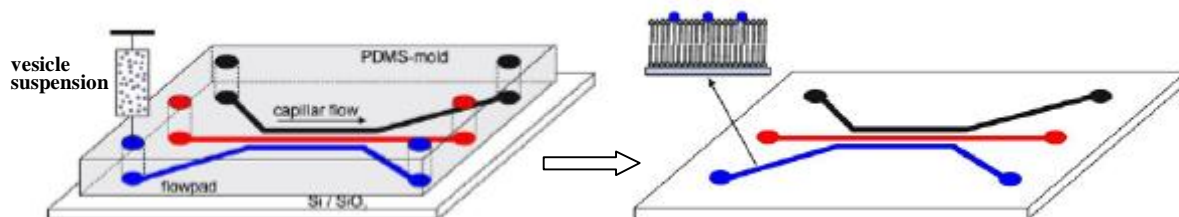


Fig.3.11 Preparation of individually addressable microstructured lipid membranes on solid supports by micromolding in capillaries.

3.6 Fluorescence recovery after photobleaching (FRAP)

3.6.1 Experimental

Fluorescence recovery after photobleaching (FRAP) was measured with a Leica LCS SL confocal laser scanning microscope (Leica Microsystems, Bensheim, Germany) equipped with a 50mW Argon ion laser ($\lambda=488\text{nm}$). A very short laser pulse (1s) compared to the duration of fluorescence recovery was applied at maximum intensity to destroy the fluorescent molecules in a small region of interest. When FRAP experiments were performed on microstructured lipid membranes the bleaching laser was focused in the center of the lipid stripes to minimize any geometric confinement of the lipid diffusion. The resulted bleached spot had a Gaussian shaped intensity of about 2-3 μm radius. Immediately thereafter, recovery of the fluorescence inside the bleached spot due to the diffusion of unbleached lipids from the surroundings was recorded through at least 20 time-lapse images collected with the highly attenuated laser beam (10%), every 1.8s, at a scanning rate of 800Hz. FRAP experiments were performed on supported lipid membranes of different lipid composition, fluorescently labeled with 1mol% β -Bodipy C12-HPC.

3.6.2 Data analysis

Analysis of experimental FRAP data was performed according to Axelrod theory based on the assumptions that 1) photobleaching occurs as an irreversible first-order reaction, 2) the laser beam has a Gaussian intensity profile, 3) fluorescence recovery is the result of pure 2D diffusion, in the absence of any flow and 5) the duration of the bleaching pulse is short compared to the characteristic time for fluorescence recovery.

Two parameters can be deduced from FRAP: the mobile fraction of the fluorescent molecules M and the diffusion coefficient D of the fluorescent species, which is related to the characteristic diffusion time τ_D :

$$\tau_D = \omega^2 / 4D \quad (3.1)$$

where ω is defined as the half-width at e^{-2} height of the Gaussian intensity profile of the laser beam. The mobile fraction M was determined by comparing the fluorescence in the bleached region after full recovery (F_∞) with the fluorescence before bleaching (F_i) and just after bleaching (F_0):

$$M = (F_\infty - F_0) / (F_i - F_0) \quad (3.2)$$

The mobile fraction is determined by discontinuities in the membrane such as membrane barriers or microdomains that can prevent or restrict temporarily the free diffusion of the fluorescent molecules.

The fluorescence intensity observed at a time $t \geq 0$ is dependent on the intensity profile of the laser beam $I(r)$ and on the concentration of the unbleached fluorophore $C(r, t)$ at the position r and time t through the relation:

$$F(t) = (q/A) \int I(r)C(r,t) d^2r \quad (3.3)$$

where q is the product of all quantum efficiencies of light adsorption, emission and detection, and A is the attenuation factor of the laser beam during observation of the fluorescence recovery.

For a numerical evaluation of the fluorescence intensities from the time-lapse recorded images, a series solution dependent on the amount of bleaching induced in the time T and expressed by a parameter K was applied into a home made IGOR Pro analysis software.

$$F_K(t) = (qP_0C_0/A) \sum_{n=0}^{\infty} [(-K)^n / n!] [1 + n(1 + 2t/\tau_D)]^{-1} \quad (3.4)$$

P_0 is the total laser power and $C_0 = C(\infty, t)$. The amount of bleaching K is directly proportional with the bleaching time T and the bleaching intensity $I(0)$.

The time course of the fluorescence intensity in the region of interest (ROI) that marked the bleached area was obtained calculating the average intensities for ROIs in all images that were experimentally recorded before and during the fluorescence recovery. To account for the overall bleaching of the background during monitoring of the fluorescence recovery the time dependency of the fluorescence intensity in another region of interest far from the bleached spot was simultaneously monitored and used to correct the recovery curve of the fluorescence intensity. The background corrected curve was normalized and fitted to the Axelrod series function (Eq.3.4) in order to get the characteristic diffusion time τ_D as a fitting parameter. The Gaussian profile of the bleached spot was obtained from the fluorescence image recorded immediately after bleaching and was used to calculate the Gauss radius ω . Finally, the diffusion coefficient was calculated from Eq. 3.1.

3.7 Monte Carlo simulations

Reversible adsorption of proteins on a homogenous surface was simulated with the program *VESAD* developed by Eike Lüthgens^{7, 60}. The program is based on reversible RSA algorithm. The proteins are modeled as discs with radius a and the adsorption/desorption process takes place on a square with periodic boundaries and variable area A . The input parameters for simulation are the adsorption and desorption rate constants \bar{k}_{on} (ms^{-1}) and k_{off} (s^{-1}) respectively, the transport rate constant k_{tr} , the protein concentration reflected in the number density ρ (m^{-3}), the protein size (a) and the adsorption area A . The simulation algorithm is consistent with the kinetic law of reversible adsorption (Eq.1.1) that was adapted to incorporate the effects of transport phenomena via the transport rate constant k_{tr} in the following equation:

$$\frac{d\theta}{dt} = \frac{\bar{k}_{on}\pi a^2 \rho \varphi(\theta) - k_{off}\theta}{1 + \varphi(\theta)\bar{k}_{on}/k_{tr}} \quad (3.5)$$

Once the adsorption conditions are set, the proteins adsorb randomly in the x-y plane. The adsorption takes place if there is a free area within $2a$ radius available around the x-y adsorption coordinates. If not, the adsorption is rejected. The time is incremented exponentially by $\Delta t = (-\ln r)/(\bar{k}_{on}A)$ where $0 \leq r \leq 1$ is a random number. An increment of time $\Delta t = 1/(k_{tr}A\rho_s)$ is added to take into account the mass transfer when the number density of proteins at the interface is zero. The adsorbed discs are assigned with an exponentially distributed time $\Delta t = (-\ln r)/k_{off}$. Any adsorption event leads to a decrease in the number density of proteins while desorption contributes to the increase of this number. The surface coverage $\theta(t)$ is generated when the final simulation time is reached.

The analysis of equilibrium coverage fluctuations is applied, after the truncation of the starting slope of the original data-set, only to the remaining part corresponding to the equilibrium. The mean coverage value $\langle\theta\rangle$ is subtracted and the time spacing is adjusted to be equally spaced. Fast Fourier transform is applied to this data-set to generate the power spectra which is subsequently fitted with the Lorentzian function given by Eq. 1.2.

Chapter 4

Lipid bilayers on solid supports

Solid supported lipid bilayers are simplified and yet representative experimental model systems that maintain the basic structural and dynamic properties of the biological membranes. They are designed not only for fundamental understanding of membrane mediated processes but also for their potential biotechnological applications. Due to their configuration, solid supported bilayers are amenable to quantitative characterization by a large and complementary set of surface science –based analytical methods such as atomic force microscopy (AFM), ellipsometry, surface plasmon resonance (SPR), quartz crystal microbalance (QCM), x-ray and neutron reflectivity (NR). When appropriately formed, supported membranes are separated from the substrate surface through a hydration layer of about 5-15 Å⁶¹ and exhibit two-dimensional fluidity and contiguity. Lateral heterogeneity and phase separation in multicomponent membranes are of considerable importance for understanding how molecular distributions influence the localization of many generic membrane processes of great biological relevance. Atomic force microscopy is employed in this study in order to differentiate among coexisting phases on the base of differences in surface topography.

The possibility of forming individual bilayer patches of sub-micrometer sizes, or the possibility of controlling and addressing lipid molecules in domains may lead to original biotechnological applications. One of these applications concerns the investigation of reversible adsorption of proteins on lipid membranes via analysis of equilibrium coverage fluctuations at intermediate coverage⁷.

4.1 Formation of lipid bilayer patches on silicon dioxide substrates

Lipid bilayer patches were formed by fusion with silica substrates of large unilamellar vesicles consisting of mixtures of charged and uncharged lipids. Several parameters are determinant for the formation of bilayer patches on solid supports. They are mainly related to the substrate properties (surface charge, roughness and chemical compositions), to the lipid vesicles properties (composition, charge, size and physical state) as well as to the aqueous environment (pH and ionic strength).

Diluted suspensions (3.5µg/ml) of liposomes in buffer (20mM Tris, 100mM NaCl, 1mM CaCl₂, pH=7.4) were incubated for about 30 minutes on previously hydrophilized silica wafers. The process of bilayer formation on solid supports implies the adsorption of

vesicles on the surface, their rupture and spreading into planar bilayers. Before AFM imaging, the samples were thoroughly washed with the same buffer as used for the lipid suspension in order to remove the unbound lipid vesicles. As it is shown in Fig.4.1, the bilayer patches made of POPC/POPS 4:1 lipids exhibit a large variety of sizes and shapes. The line cross section and the histogram of height AFM images prove the existence of bilayer patches of about 4nm thickness, value that is typical for lipid membranes in fluid phase. An obvious phase contrast is observable on the phase images recorded with AFM-TM, as a consequence of large differences in adhesive and viscoelastic properties between the lipid patches and the substrate. The presence of round, isolated bilayer patches (with diameters up to 150-200nm, indicated with black arrows in Fig.4.1a) demonstrates that the process of bilayer formation on silica substrate does not necessarily require, in this case, a critical vesicular coverage to initiate the transformation of the surface-bound vesicles into planar membranes. In the presence of calcium ions, the interaction energy between the adsorbed vesicles and the solid support is sufficiently high to overwhelm the cost in the vesicles curvature energy and to induce vesicles deformation. As a result, individual vesicles rupture and spread on the surface.

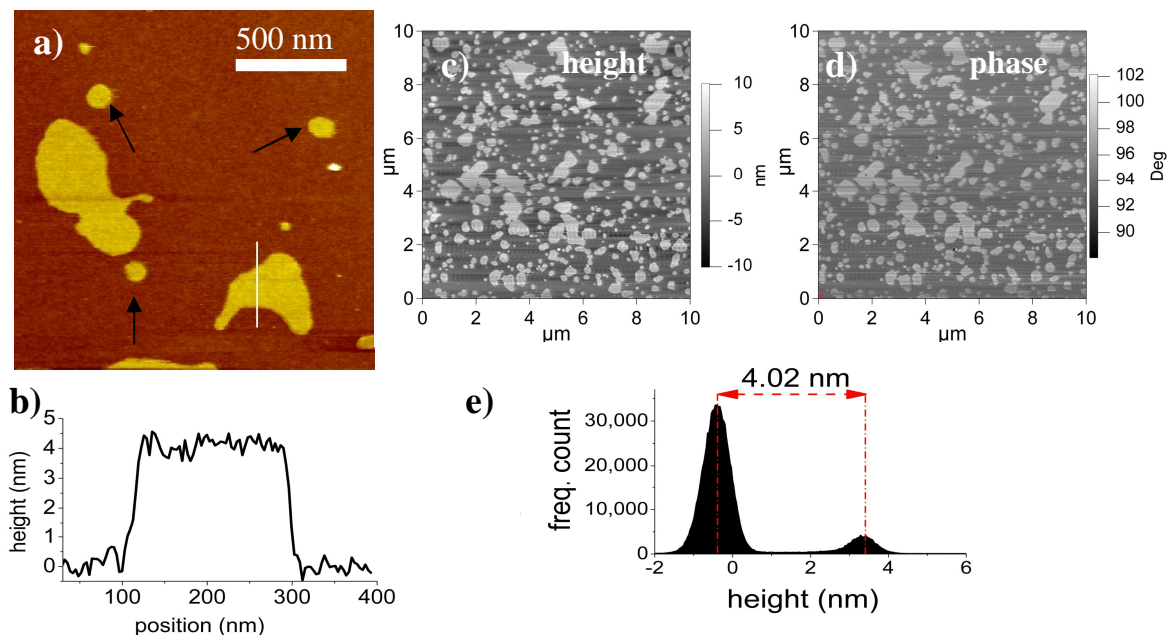


Fig. 4.1 Bilayer patches of POPC/POPS 4:1 lipid composition are formed by adhesion and rupture of lipid vesicles on hydrophilic silica substrate; a) detailed AFM-CM image: the small membrane patches (indicated by the black arrows) demonstrate that individual vesicles can rupture on the substrate without additional cooperation from neighboring vesicles; c) and d) are, respectively, the height and phase images recorded with AFM-TM in liquid. The height profile b) corresponding to the line cross section in a) and the histogram e) corresponding to the image c) show typical membranes thickness of about 4 nm.

According to the theoretical calculations of Seifert⁶², a lipid vesicle adhered to the substrate would rupture if its radius is larger than a critical radius derived from the condition that the free energy of the bound vesicle exceeds the corresponding free

energy of the bound disk. It is generally observed that divalent calcium ions are able to promote the rupture of lipid vesicles that otherwise would remain intact on the substrate. One explanation for this observation could be that Ca^{2+} may modify the bending modulus of the lipid membrane via modifying the phospholipids packing⁶³. Ca^{2+} may also affect the effective interaction potential between the bilayer and the supporting substrate.

Large (few μm size) bilayer patches of irregular shapes could be obtained (Fig.4.2) from lipid mixtures containing saturated lipids (80% POPC, 16 % DPPC, 4 %DPPS). The AFM histograms indicate an average membrane thickness of 4.63nm, value that is slightly higher than the thickness of the bilayer patches consisting of only saturated lipids in fluid phase.

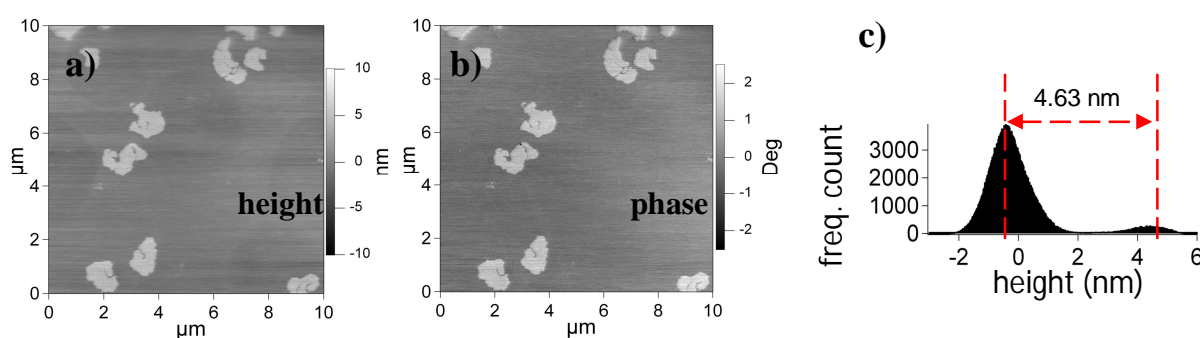


Fig.4.2 AFM-TM images (a-height and b-phase) of bilayer patches formed from vesicles containing mixtures of charged and saturated lipids (80% POPC, 16 % DPPC, 4 %DPPS). The histogram c) indicates patches of about 4.63nm thickness.

Two scenarios are conceivable for the formation of bilayer patches that are much larger than the dimensions ($\sim 100\text{nm}$) of the lipid vesicles used in this work. One alternative is that the vesicles that are adjacently adsorbed on the substrate fuse, before they rupture, into larger vesicles which are easier deformed thru interactions with the adhesive substrate. The second alternative is that the neighboring vesicles do not necessarily fuse but rather rupture in a cooperative way. An AFM snapshot that was caught at an intermediate step during the process of lipid bilayer formation on silica substrate is shown in Fig.4.3. The image was recorded shortly after deposition of the liposomes suspension on the substrate, at an intermediate moment during the processes of vesicles rupture. One can see that a part of the vesicles already formed bilayer patches while many others are still intact on the substrate. This image supports the hypothesis of the cooperative effect. Many large patches are adjacent to groups of vesicles that are still intact (as those indicated with the black arrows). These membrane patches expose active edges made of the hydrophobic segments of the acyl chains which can promote, through hydrophobic interactions, additional deformation and eventual rupture of the neighboring vesicles. The height information extracted from the recorded AFM images shows that upon adhesion on the silica substrate, the lipid vesicles adopt a flattened configuration, presenting an average height of about 50nm. The bilayer patches that are formed upon individual or cooperative vesicles rupture may grow afterwards as a result

of coalescence with other adjacent bilayer patches (see Fig.4.3a, the indication with the red arrow).

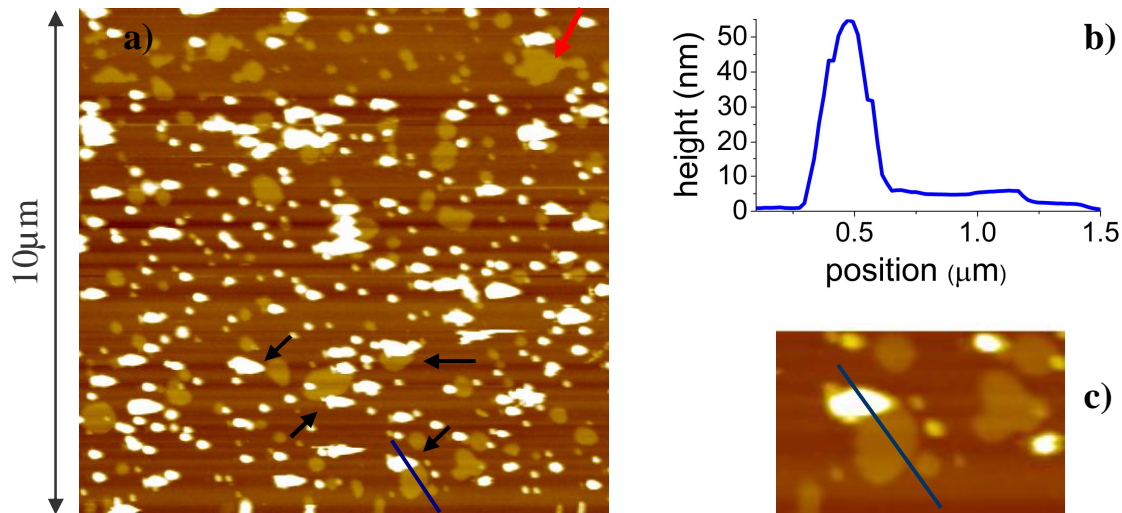


Fig. 4.3: a) AFM-CM image recorded at an intermediate step, shortly after deposition of the lipid vesicles suspension (4:1 POPC/POPS) on the silica substrate. A part of the vesicles already formed bilayer patches while many others are still intact on the substrate. The black arrows indicate large patches that are adjacent to groups of vesicles that did not rupture yet. Image c) is an enlarged view from the image a). The line cross section b) shows that the vesicles that adhered on the substrate are deformed due to their interactions with the substrate and adopt a flattened aspect (around 55nm height). The active edges of the bilayer patch (about 4 nm thickness) may induce additional deformation to the adjoining lipid vesicles and promote further ruptures until complete, isolated bilayer patches of irregular shapes are formed (an example is indicated with the red arrow). Before AFM imaging the sample was washed with buffer to remove the unbound vesicles. The tails along the scan direction are believed to be due to a combination of weak tip-sample interaction and low feedback gains chosen for the image acquisition.

The coverage of the surface with lipid bilayer patches increases if more lipid vesicles are supplied to the incubation solution. At low lipid concentrations, as used in this study, the patches remained as isolated islands of non spherical shapes. This indicates support-induced constraints in the lipid assemblies' lateral mobility that impede the minimization of the line tension via collective shape changes into circular patches. The explanation for the immobility of lipid assemblies on silica substrates may lay in the nature of calcium mediated interaction between the solid support and the lipid membrane, in the roughness of the underlying surface or in the water layer thickness between the lipids and the substrate.

4.2 Micro-domains and nano-domains in multicomponent lipid bilayers

Continuous, multicomponent lipid bilayers supported on hydrophilic silica substrates were formed by spreading liposomes at higher lipid concentrations than that used for membrane patches formation. A droplet of 0.5 mg/ml LUVs suspension in Ca^{2+} containing TRIS buffer was deposited on the substrate for about 30 min. After membrane formation, the excess of lipid vesicles was flushed away by rinsing the surface with buffer. DPPC containing lipid vesicles were spread at a higher temperature than the main transition temperature of DPPC (41°C).

Separation of lipids into membrane domains of various sizes and shapes was visualized with AFM (Fig.4.4) as a function of the membrane content, at room temperature, under identical buffer conditions (pH, ionic strength, Ca^{2+} conc.). Membranes with the following lipid compositions were investigated: (A) 80%DPPC, 16%POPC, 4%POPS; (B) 60%POPC, 32%DPPC, 8%DPPS; (C) 80%POPC, 16%DPPC, 4%DPPS; (D) 50%POPC, 50%DPPC. AFM imaging was performed in tapping mode (A, B, C) and in contact mode (D). The concentration of calcium ions in buffer was 5mM for all cases (A-D).

The successful formation of continuous lipid membranes on glass substrates is demonstrated by the AFM phase images. In comparison to the bilayer patches shown in the previous section, almost no phase contrast is observable for the lipid domains, a clear prove that the scanned surfaces are entirely covered and present similar viscoelastic and adhesive properties. The solid phase DPPC/DPPS enriched domains are, on average, $1\pm 0.2\text{nm}$ higher than the fluid phase of POPC/POPS lipids and appear, according to the colour code, as brighter areas on the height AFM maps.

Phase segregation is essentially dependent on the percentage of charged and gel phase lipids. No domains are formed in membranes containing only 20% DPPC/DPPS (4:1)- Fig.4.4C- but they appear in membranes with increased content of lipids in gel phase: 40% DPPC/DPPS (4:1)-Fig.4.4B. One can confirm therefore that, under similar conditions, there is a threshold value of the solid phase lipids' percentage from that the lateral phase separation occurs. The presence of charged lipids (in this case DPPS) influences the value of this threshold and may affect the size and the aspect of the membrane domains. For a bilayer consisting of only zwitterionic lipids in a ratio 1:1 DPPC/POPC (case D) the domains are uniform in size and shape, and are considerably smaller than the domains formed in bilayers containing additionally charged lipids-DPPS (case B). It is interesting to observe that the neutral bilayer with 50% lipids in gel phase presents an overall uniform distribution of small, circular domains (of 55nm mean diameter -histogram D3 in Fig. 4.4). These nanodomains are about 1nm higher than the surrounding fluid phase. A defect (lipid free glass substrate) found in the supported membrane allowed the measurement of the membrane thickness which is about 4-5nm (Fig. 4.4D2). The stability of these small circular domains was critically dependent on the ambient temperature. An increase of only few degrees in the ambient temperature determined the disappearance of the domains. No lateral phase separation occurred in neutral membranes with a lower content than 50% of lipids in gel phase (data not shown). These observations may lead to the conclusion that the state of composition 1:1 DPPC/POPC is located in the metastable region of the phase diagram, delimited by the spinodal and binodal curves.

Totally different is the lateral organization in a membrane that contains a small fraction of charged lipids. Even for only 40% lipids in gel phase, when the 4th fraction of them is represented by anionic lipids (DPPS), lateral phase separation takes place. The domains are large (in μm range, predominantly convex but not circularly shaped, and stable with respect to small fluctuations in the ambient temperature. By lowering the percentage of DPPC/DPPS lipids to 20%, no lateral segregation is observable, neither in the height image nor in the phase image – Fig.4.4C. At high content of lipids in gel phase (e.g. 80%DPPC) the lipids segregate in irregular shaped islands of various sizes that cover most of the surface and are separated by channels of fluid phase lipids- Fig. 4.4 A.

A change in the lipid domains morphology was observed by Reviakine⁶⁴ in binary lipid membranes (DPPC/DOPS mixtures) when Ca^{2+} in the samples' buffer was chelated with EDTA. The role of the divalent calcium ions that are supposed to bind preferentially to PS lipids, to modify the chain packing density, and to intermediate the interaction between the lipid head groups and the underlying substrate is however complex and, so far, not comprehensively understood. In the experiments here, Ca^{2+} was permanently present in the buffer, at the same concentration, for all samples. The changes observed in the bilayers topography are solely the result of modifications of the membrane content.

For binary mixtures, the process of phase separation in the lipid membrane can be satisfactorily described by adapting the Bragg-Williams formula⁶⁵ for the free energy of mixing in regular solutions as following:

$$\Delta F_m / k_B T = \sum_i n_i \ln \phi_i + \chi n \prod_i \phi_i + \Delta E_{add} \quad (4.1)$$

where $\phi_i = n_i / n$ is the mol fraction of the lipid species "i" in the membrane. The first term in eq. 4.1 represents the entropy of mixing and is always negative; the second term stands for the enthalpy of mixing, while the last term accounts for the line tension on the border of lipid domains and/or for additional interactions in the membrane such as dipolar or electrostatic interactions between the headgroups of the constituent lipids. The non-ideality parameter χ is a measure of the chemical mismatch between the different lipid species. For a given lipid composition and at constant temperature, its value is decisive for the lateral segregation of lipids. In the case of lipid bilayer shown in Fig. 4.4D1 the lipid composition is $\phi_{DPPC} = \phi_{POPC} = 0.5$ that imply that, according to Eq.4.1 when the last term is neglected ($\Delta E_{add} = 0$), the calculated value of nonideality parameter should fulfil the condition $\chi \geq 2$ such that the lateral segregation appears. In a more accurate description of the real lipid mixtures, the contribution of ΔE_{add} to the free energy of the membrane is not neglected and therefore the critical value of non-ideality parameter is shifted towards larger values. For instance, if the binary membrane contains charged lipids and only monovalent ions are present in the buffer, the electrostatic contribution of ΔE_{add} can be analytically calculated in the framework of mean field theory. The resulting condition for phase separation is $\chi \geq 3.7$, values for that the free energy curve has regions of negative curvature. Estimation of ΔE_{add} is however very complex and beyond the mean field theory when divalent ions (e.g. Ca^{2+}) are present in the buffer.

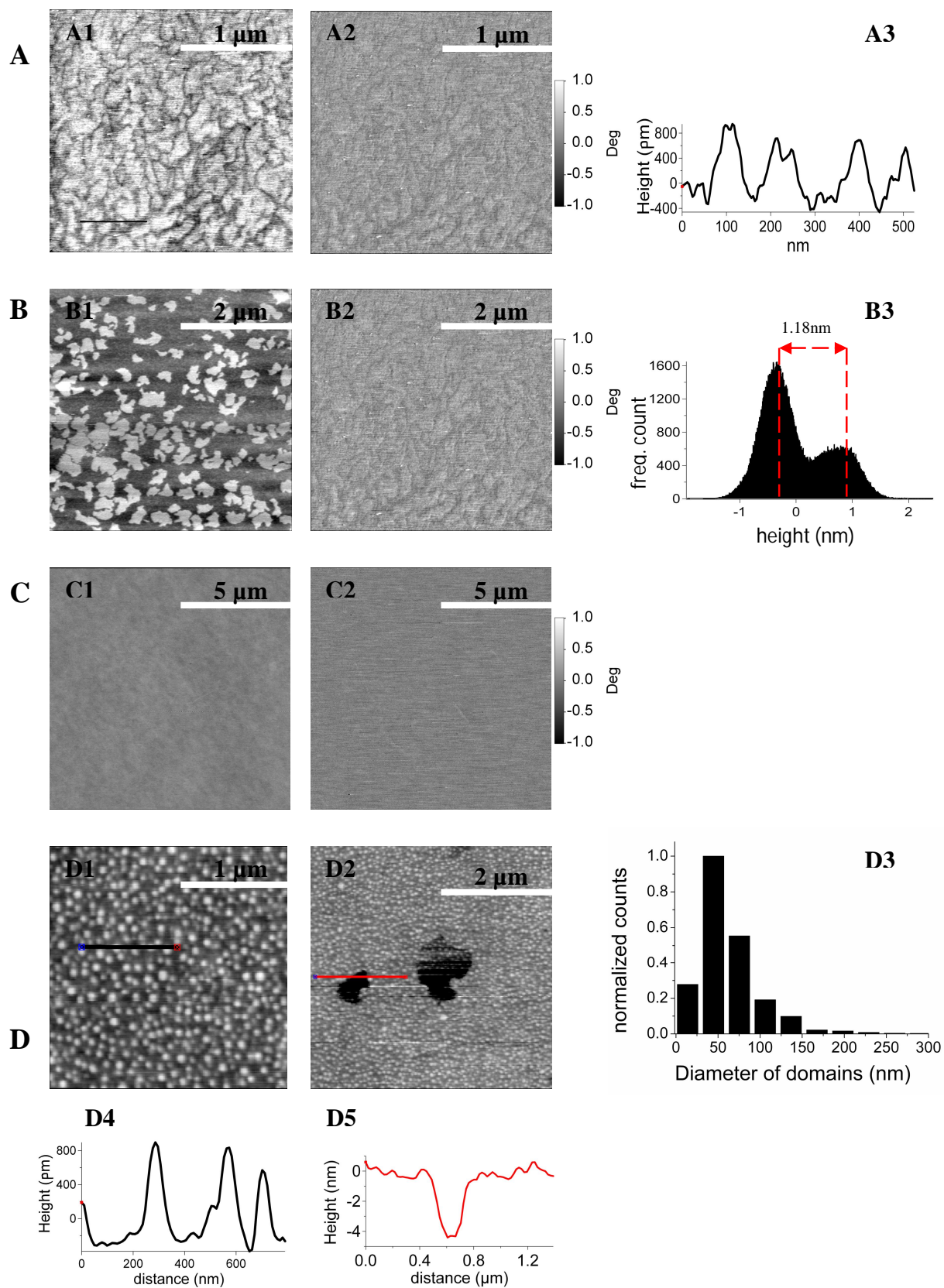


Fig. 4.4 Lateral phase separation in solid supported lipid bilayers of different compositions: AFM images were performed in liquid, at room temperature, in TM (A-C) and CM (D). A: lipid composition is 80% DPPC, 16% POPC, 4%POPS; A1 and A2 are height and phase images respectively; the line cross section (A3) for the line indicated in image A1 shows domains that are about 1.2 nm higher than the surrounding fluid phase. B: lipid composition is 60% POPC, 32% DPPC, 8%DPPS; B1 and B2 are height and phase images respectively; the histogram B3 shows the height difference between the domains and fluid phase for image B1. C: lipid composition is 80% POPC, 16% DPPC, 4% DPPS; no lateral phase separation could be observable neither in the height image (C1) nor in the phase image (C2). D: lipid composition is 50% POPC, 50% DPPC; height images D1 and D2 show nanodomains of 55nm average diameter whose size distribution is represented in the histogram D3; the line cross section (D3) for the line indicated in image D1 show that the domains are about 1 nm higher than the surrounding fluid phase; the dark areas in image D3 are defects in the supported bilayer and their deepness of about 4-5 nm measured by the cross section D5 is typical for successfully formed lipid bilayers on solid supports.

The question why the small domains shown in case D do not increase in size until the full phase separation may be answered on the basis of the entropic traps that stabilize the nanodomains. After early nucleation and independent growth stages, the nanodomains may grow further via merger or Ostwald ripening. The entropy and boundary energy compete to trap nanodomains. For low line tensions the nanodomains are stabilized (case D). For high line tensions, the decrease in the boundary energy dominates the unfavourable entropy of merger and the domains grow to the micrometer scale (case B). Besides the membrane lipid composition, the coupling between the leaflets of the bilayer, the nature of the bilayer interactions with the supporting substrate as well as the buffer properties are factors that may affect the domains merger.

The irregular shapes of the gel phase domains enriched in anionic lipids (case B) may be, in part, due to the dipolar and electrostatic interactions between the headgroups of lipids within the domains as well as the result of coalescence of small domains. The interactions of Ca^{2+} with DPPS lipids induce a partial neutralization of the charged headgroups and therefore determine a decrease in the repulsion magnitude concomitant with a decrease in the surface area per charged lipid⁶⁴. The resulting changes in packing and lipid orientation enhance the hydrophobic mismatch between the domain and the surrounding membrane and in consequence contribute to the increase of the line tension, favoring the formation of large domains (as observed in case B). Calculations of the effects of lipid splay and tilt deformations show that the line tension of domains increases quadratically with the thickness difference on the domains border⁶⁶.

Domains of sizes that vary between tens of nanometers to 10 μm were reported in the literature for solid supported monolayers and bilayers prepared from different ternary lipid mixtures that are used to model the properties of membrane rafts⁶⁷. A study of DLPC/DPPC/Chol mixtures has shown that the sizes of domains decrease with increasing concentrations of cholesterol in the membrane⁶⁸. Controversial information is provided by different studies on the domain sizes in SM/POPC/Chol mixtures. While large circular domains are observed in giant vesicles, smaller domains are reported for similar membrane compositions by FRET experiments⁶⁷. Nanodomains and their stability is increasingly being a subject of debate and interest in the literature as relevant models for

understanding the lipid organization in cellular membranes where rafts sizes are believed to be in the range of 10-200 nm⁶⁹.

A recent study pointed out the influence of the lipid oxidation on the morphology of multicomponent lipid membranes containing unsaturated lipids (DOPC). Air exposure promotes the formation of large microdomains from monolayers that have only nanodomains in a inert environment⁸. To preclude lipid oxidation from affecting the results, POPC was chosen in this study as the fluid phase component of the membranes. The rate of oxidation is significantly slower for POPC than for DOPC since POPC has only one single unsaturated acyl chain while DOPC has two.

4.3 Conclusions

Bilayer patches and continuous lipid membranes of different lipid compositions are formed on silica substrates and analysed by means of atomic force microscopy. Under the conditions used in this work, AFM images reveal that the interaction with the hydrophilic silica substrate is sufficient to promote the deformation and rupture of individual adhered vesicles. AFM snapshots recorded during the membrane spreading process suggest that the "active" edges of the bilayer patches resulting from the vesicles that ruptured first on the substrate may induce, through hydrophobic interactions, additional deformation and eventual rupture of the adjacent vesicles. The persistent irregular shapes of the bilayer patches indicate support-induced constrains in the lipid assemblies' lateral mobility that impede the minimization of the lipid membrane line tension via reorganization into circular patches.

Investigation of the topography of continuous, multicomponent bilayers demonstrates that under identical conditions, not only the lateral phase separation but also the size and the shape of the domains are dependent on the lipid membrane composition. It is shown that the tendency for phase segregation is more pronounced in the presence of divalent calcium ions for membranes containing anionic lipids as compared to neutral bilayers. Nanodomains are visualized for 1:1 POPC/DPPC lipid mixtures when the decrease in the boundary energy of domains is overwhelmed by the unfavorable entropy of merger that prevents the membrane from full phase separation.

Chapter 5

Reversible and irreversible adsorption of proteins

Lipid-protein interactions play a pivotal role in many biological processes that take place at the level of cellular lipid membranes. The adsorption of two peripheral proteins, annexin A1 and prothrombin, to solid supported lipid bilayers was investigated in this study by means of AFM and Ellipsometry. Despite of their different structures and functionalities, both proteins adsorb preferentially, in a Ca^{2+} -dependent manner, on membranes containing acidic phospholipids.

Annexin A1 is preferentially located on the cytosolic face of the plasma membrane and it has been shown to be highly expressed in the cells of the innate immune system. For instance, about 3-4 % of the total cytosolic proteins of blood neutrophils and monocytes is represented by annexin A1. When the neutrophils adhere to the inflamed vascular endothelium, annexin A1 is externalized on the cell surface and blocks the interaction with the endothelial cells⁷⁰. Besides its role in inflammation, annexin A1 is involved in vesiculation⁷¹, membrane fusion⁷², or participates in the plasma membrane repair mechanism⁷³.

The structure of annexin A1 is similar to that of the proteins of the same class of annexins. The protein (38kDa) form a core domain consisting of four conserved structural repeats, each about 70-75 residues in length. Each repeat unit is formed from five α -helices (Fig.5.1). Remarkably, all eight Ca^{2+} -binding sites are on the same curved side of the annexin A1 structure, forming a convex surface which has been proposed to interact with the membrane.

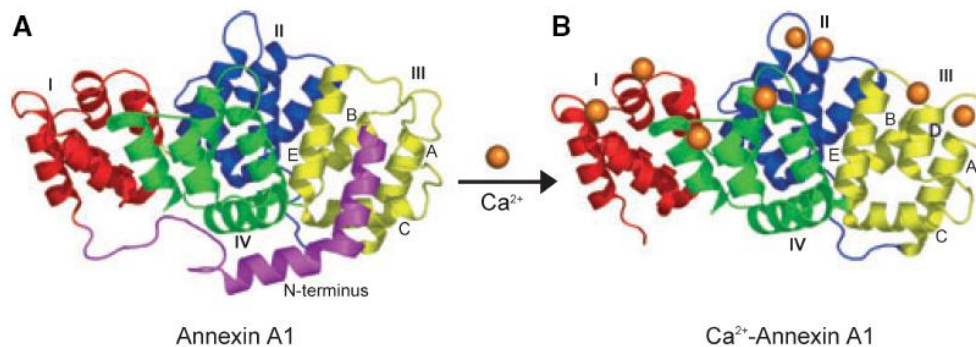


Fig.5.1 Ribbon representation of apo-annexin A1 (A) and Ca^{2+} -annexin A1 (B). The core repeats (I to IV) are differently colored. Calcium ions are shown as orange spheres. In the presence of Ca^{2+} , the N-terminus (magenta color) is expelled from the core domain. The picture is reproduced from Rintala-Dempsey et al.⁷⁴.

Prothrombin is a plasma protein (72 kDa) which is synthesized in liver. The activation of prothrombin to thrombin is a key control reaction in the blood coagulation cascade and it is widely appreciated that mixtures of anionic and neutral lipids (i.e. phosphatidylserine (PS) and phosphatidylcholine (PC)) provide the most efficient catalytic surface for this activation process. The mature prothrombin is a single chain protein that contains highly conserved γ -carboxyglutamic acid (Gla) residues within the first 40 aminoacids residues of the N-terminal portion. Two other regions of internal homology that are referred to as “kringle” structures are located between the residues 40 and 270 (Fig.5.2A). Prothrombin circulates in the blood plasma as a zymogen and, during coagulation it is proteolytically converted to thrombin by the prothrombinase complex consisting of the activated factors X_a and V_a adsorbed on PS containing phospholipid membranes such as those of platelets, peripheral blood mononuclear cells and endothelial cells. Binding of prothrombin to these membranes is essential. The protein–membrane association occurs by chelate complex formation between Ca^{2+} and electron donating groups supplied by Gla residues of the protein and phosphate, amino and carboxyl groups of PS⁷⁵⁻⁷⁷.

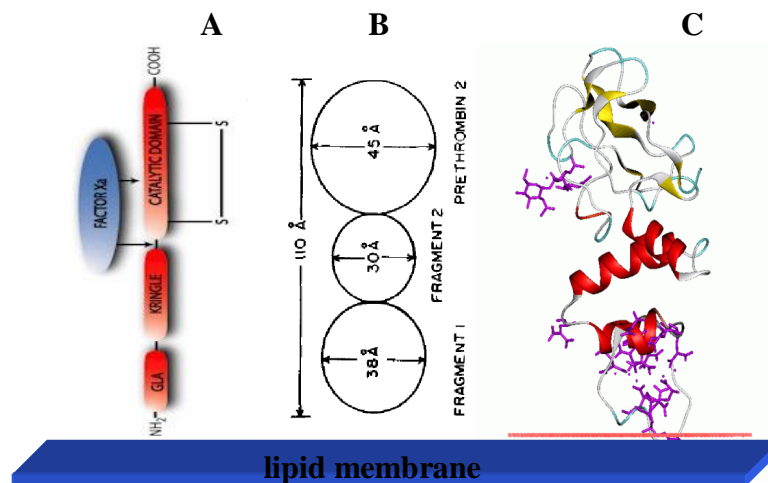


Fig. 5.2 Three schematic representations of the domain structure of prothrombin (in solution) with respect to their functionality (A), size (B) and tertiary structure (C). The orientation of prothrombin is depicted in relation with the lipid membrane during the adsorption process. A) GLA = region containing γ -carboxyglutamic acid residues, KRINGLE = regions of internal sequence homology, CATALYTIC DOMAIN = region containing the serine protease catalytic triad. Arrows indicate the sites which are proteolytically cleaved by factor X_a during activation of the zymogen; B) estimated lengths of the prothrombin domains as resulted from quasi-elastic light scattering (QELS)⁷⁸; C) tertiary structure of prothrombin.

5.1 Calcium-induced and annexin A1-induced clustering of acidic phospholipids in ternary lipid membranes

Atomic force microscopy was employed to characterize the adsorption of annexin A1 to ternary lipid bilayers containing gel and fluid phase lipids in different proportions. Clean silicon dioxide was used as substrate for spreading large unilamellar lipid vesicles (0.5 mg/ml in buffer: 20 mM Tris, 100mM NaCl, 1mM CaCl₂, pH=7.4). Following the membrane formation, the excess of vesicles was flushed with buffer. Prior protein addition, the lipid bilayers were incubated with higher CaCl₂ concentrations (5mM) of the same buffer and imaged with AFM. The membranes with a lipid content of 60%POPC,32%DPPC,8%DPPS exhibit lateral phase separation; at room temperature, the gel phase lipids segregate into domains that are about 1.1-1.2nm higher than the surrounding fluid phase (Fig. 5.3). Incubation of these lipid bilayers with annexin A1, added to a final concentration of 1μM determined an additional increase of the domains height with about 2.2-2.4 nm. This increase is due to the known preferential adsorption of annexin A1 to PS enriched domains^{60, 79}. A similar thickness (2.2±0.3nm) of the adsorbed annexin A1 layer was measured on binary fluid membranes of 4:1 POPC/POPS lipid composition⁶⁰. It is confirmed here that annexin A1 adsorbs irreversibly to PS-enriched lipid domains. The protein did not desorb after gentle washing of the sample with protein-free buffer containing 5mM CaCl₂.

It is generally accepted that calcium ions may induce lateral phase separation in PS-containing lipid membranes^{79,80}. The idea of Ca²⁺ modulated annexin A1 adsorption via reorganization of anionic lipids into domains was recently reinforced⁸¹. However, the clustering capacity of calcium ions is dependent on the proportion of anionic lipids that are present in the membrane. For a lipid membrane containing 80%POPC, 16%DPPC, 4%DPPS no lateral phase separation occurs at 1mM, nor at 5mM concentration of Ca²⁺ in buffer (Fig.5.4A). Following the incubation with 0.5μM annexin A1 in 5mM CaCl₂ containing buffer, AFM images reveal protein domains that are about 2.2 nm higher than the lipid membrane (Fig. 5.4B). Since the protein domains remain stable after gentle washing of the membrane with protein-free buffer containing Ca²⁺, one can deduce that annexin A1 is irreversibly adsorbed to the bilayer. This means that the membrane exposes, in the protein contact areas, high affinity binding sites that are similar to those that are available on the Ca²⁺-induced lipid domains. This observation implies that annexin A1 may induce clustering of PS molecules into domains that ensure its irreversible association with the lipid bilayer. Calcium ions remain, however, the main players even in the process of protein-induced domain formation. Since 8 ions of Ca²⁺ are bound to the active configuration of a single annexin A1 molecule, one can envision the protein in this form as a positive macroion that is more capable (or efficient) than the free, singular calcium ions to cluster the acidic phospholipids during the interaction with the membrane.

If the PS content of the lipid bilayer in a CaCl₂ containing buffer is sufficiently high (i.e. for 4:1 PC/PS lipid composition), the interaction of free calcium ions with the lipid membrane may be sufficient to induce a complete phase separation such that the

additional interaction of annexin A1 with the membrane does not further contribute to the lateral segregation of lipids and therefore no increase of surface coverage with domains may be noticeable (as reported by Janshoff et al. ⁷⁹).

In the present study, the membrane has a lower anionic lipid content (only 4% DPPS) and remains stable with respect to phase separation, even in a solution with a high Ca^{2+} concentration (5mM). The additional interaction of the lipid bilayer with the active annexin A1 molecules that concentrate eight calcium ions bound on its surface may induce the clustering of acidic phospholipids such that protein domains are adsorbed. The height of these domains (2.2nm) correspond well to the thickness of an adsorbed annexin A1 layer but it does not correspond to an additional 1nm increase that would be expected if the underlying lipids would be predominantly in the gel phase. It is not clear whether this value, smaller than expected, is due to a possible higher indentation of the soft surface during AFM scanning or, rather than inducing underlying gel phase domains, the active annexin A1 dislocates and clusters only the DPPS (but not DPPC!) molecules that form areas with high affinity binding sites in a relatively homogenous DPPC/POPC lipid matrix.

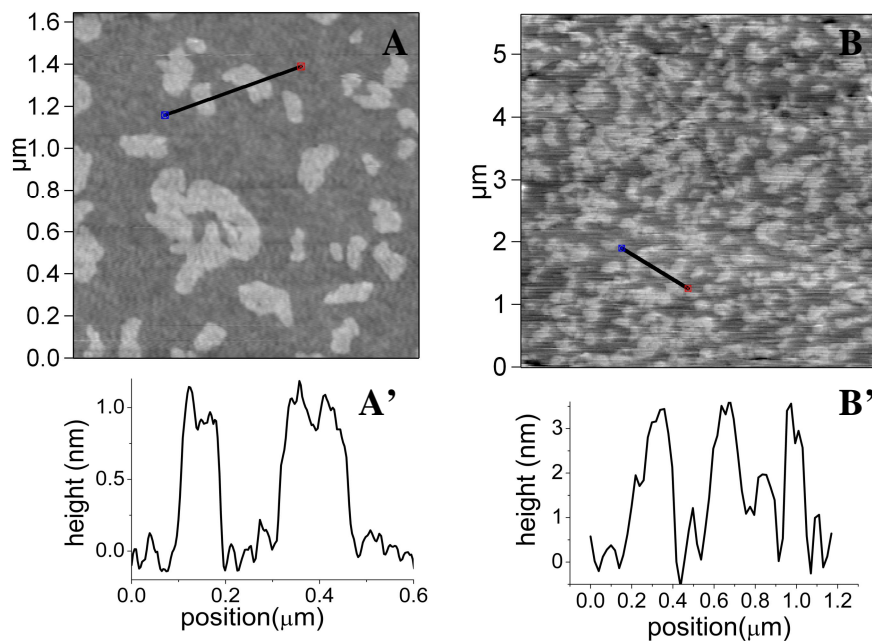


Fig.5.3 AFM visualization of the height increase of DPPS enriched domains as a result of preferential annexin A1 adsorption: A) AFM topography of the solid supported lipid membrane of composition 60%POPC, 32%DPPC, 8%DPPS; the line cross section A' indicates lipid gel phase domains of about 1-1.2 nm height; B) AFM topography of the membrane after adsorption of annexin A1; some small defects (black holes) that are seen in the upper part of the image are 3.95nm deep with respect to the non-domain areas and 6.2 nm deep with respect to the domains; the line cross section B' indicates an increase in the domain height with about 2.2-2.5nm after the adsorption of annexin A1, increase that corresponds to the protein layer thickness; before imaging the samples were washed with buffer containing 5mM CaCl_2 .

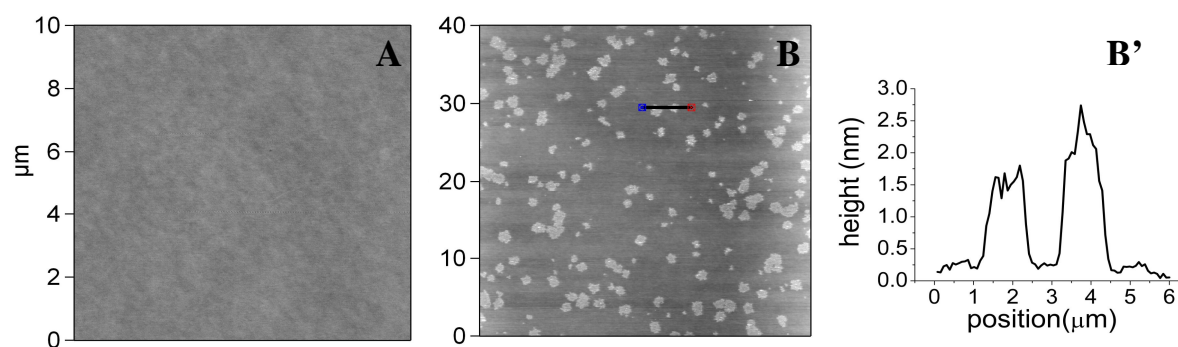


Fig.5.4 AFM visualization of the protein domains formation following the adsorption of annexin A1 on the solid supported lipid membrane of composition 80%POPC,16%DPPC, 4%DPPS: A) before the adsorption of annexin A1, the lipid bilayer has a homogenous composition without lateral phase separation; B) protein domains are formed on the bilayer after incubation with 0.5μM annexin A1; B') the line cross section indicates domains of about 2.4nm height; before imaging the samples were washed with buffer containing 5mM CaCl₂.

5.2 Ellipsometric characterization of reversible adsorption of prothrombin on mixed anionic lipid bilayers

The investigation of prothrombin adsorption on negatively charged lipid membranes was performed for protein concentrations lower than 3μM, value which is the upper limit of prothrombin concentration in human blood plasma. The lipid content of the membranes was 4:1 POPC/POPS, composition that can be considered physiologically relevant for the biological membranes involved in coagulation process that have about or less than 20% acidic phospholipids. A typical setup for null-ellipsometry with a Nd:YAG laser ($\lambda=532\text{nm}$, adjustable power) was used to record the time course of the ellipsometric angles Δ and ψ during the experiments. The thicknesses of the deposited layers were obtained from the fitting procedure through a mathematical model with fixed optical constants (see Section 2.2.3). The buffer exchange in the measuring cell was possible via a liquid handling system in connection with a peristaltic pump that insured a continuous and constant flow of the liquid into the cell. The lipid vesicles suspension (0.5mg/ml) in buffer (20mM Tris, 100mM NaCl, 1mM CaCl₂, pH=7.4) were spread on the hydrophilic silica substrate. Before starting the experiment, the initial SiO₂ layer on the silicon support was determined, by 4 zone ellipsometry measurements, to be as thick as 1.4nm. The drop in Δ from 178.2° to 174.92° (Fig.5.5a) corresponds to the formation of a continuous lipid bilayer of about 4.5nm thickness on the silica substrate. The excess of lipid vesicles was removed from the measuring cell by flushing the sample only with buffer. Thereafter, prothrombin (1.9μM suspension in buffer enriched with 2mM CaCl₂ and 1mM NaNO₃) was adsorbed onto the planar lipid membrane. In consequence, the ellipsometric angle Δ dropped to 174.65°, value that corresponds to an average protein layer of 0.34±0.12nm. Stepwise increase in the buffer CaCl₂ concentration, first up to 3mM and then up to 5mM,

determined consecutive decreases in the Δ values down to 174.38° and 174.29° , which correspond to the estimated average thickness of $0.63 \pm 0.12 \text{ nm}$ and $0.74 \pm 0.12 \text{ nm}$, respectively (Fig.5.5b). No further increase in prothrombin adsorption was recorded when CaCl_2 concentration was raised from 5 mM to 10 mM indicating that the saturation with calcium ions of the binding process was already reached. Washing with protein free buffer at much lower CaCl_2 concentration (1 mM) induced considerable prothrombin desorption from the lipid bilayer. From the increase to 174.78° of the Δ value, a final average thickness of the remaining protein layer of $0.157 \pm 0.12 \text{ nm}$ is estimated.

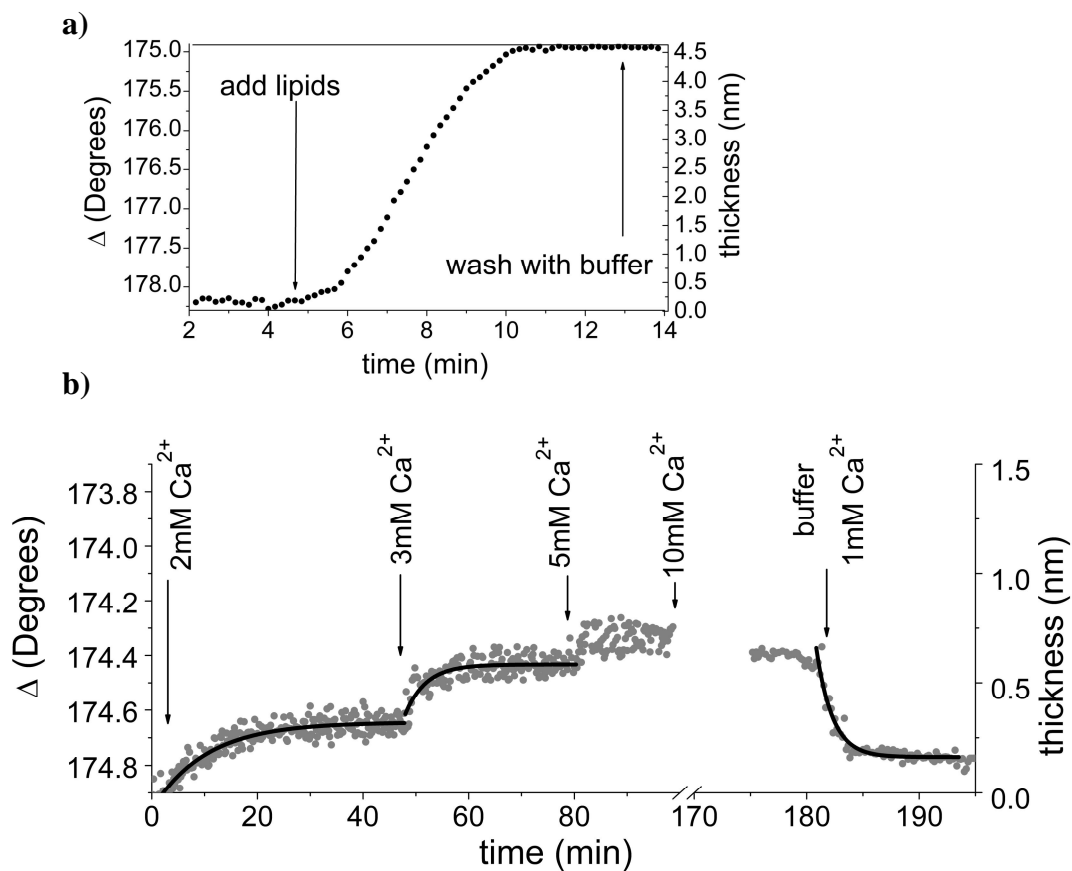


Fig.5.5 Time course dependence of the ellipsometric angle Δ and of the corresponding average thickness lipids or proteins layer (estimated from the fitting procedure to the mathematical model with fixed optical constants) during the process of the lipid bilayer formation (a) and subsequent prothrombin adsorption at increasing CaCl_2 concentrations (b). Following the formation of a continuous lipid membrane (POPC/POPS 4:1) the excess of lipid vesicles was flushed with buffer and prothrombin was added to a final concentration of $1.9 \mu\text{M}$ in buffer containing initially 2 mM CaCl_2 . Stepwise increasing of CaCl_2 concentration induced an increased adsorption of prothrombin to the membrane up to a saturation limit. Washing with protein free buffer at much lower CaCl_2 concentration (1 mM) determined considerable desorption of prothrombin from the lipid bilayer. The Δ scale was inverted for a more suggestive representation of the variation in the lipid/protein layer thicknesses. The gray dots represent the experimental data while the continuous lines are theoretical fits according to Eq.5.1.

It has been found that prothrombin undergoes a Ca^{2+} -dependent transition (cis-trans proline isomerization) in order to obtain a molecular form with binding capacity⁸². In solution, as depicted in Fig.5.2, the protein has an overall length of about 11nm. Upon binding of the fragment 1 to the PS-containing membranes, the prothrombin molecule adopts a tighter folding on the lipid surface or it may tilt with respect to the bilayer normal such as the distance between the C-terminus of the protein and the phospholipid surface is about 9.4nm⁸³. Considering a proportional relation between the ellipsometrically estimated average thickness of the adsorbed submonolayer of prothrombin and the surface coverage, the dependence of prothrombin adsorption on Ca^{2+} concentration is plotted in Fig. 5.6a. For a lipid bilayer containing 20%POPS, the saturation concentration of calcium is 5mM.

It has been proposed a binding stoichiometry for prothrombin of 42 lipids/protein⁸³ and it is generally accepted that a constant number (8 to 10) of phosphatidylserine residues interact with the bound prothrombin regardless of the membrane composition⁸⁴. The affinity for prothrombin is therefore sensitive to the spacing between PS molecules. For a homogenous lipid bilayer with 20% POPS content it may be that discrete clusters of acidic phospholipids need to form in order to facilitate the protein adsorption. Increased Ca^{2+} concentrations may contribute to the lateral reorganization of PS molecules in order to facilitate the adsorption of prothrombin.

Calcium ions are required for maintaining the correct conformation of prothrombin and also for mediating the formation of PS-Gla complexes. No adsorption was observed in the absence of calcium. 79.8% of prothrombin was removed from the membrane after washing with protein free buffer containing only 1mM CaCl_2 (Fig 5.5b). The dissociation of protein from the membrane is however not only the consequence of the Ca^{2+} concentration decrease (from 10mM to 1mM) but also the result of reversible association of prothrombin to the lipid bilayer. When EDTA was added to the buffer, the protein was completely removed from the surface as the ellipsometric angle Δ grew up to the initial value before adding the protein.

The reversibility of prothrombin binding to PS containing lipid membranes is illustrated in Fig.5.6b. Adsorption of the protein (2.8 μM) to 4:1 the POPC/POPS lipid bilayer at saturating Ca^{2+} concentration (5mM) indicates a decrease of the ellipsometric angle Δ to a value that corresponds to an average protein thickness of about 1.38nm (14.89% coverage). After exchanging the prothrombin containing buffer with a protein-free buffer having the same Ca^{2+} content (5mM), the equivalent average thickness of the protein layer decreased to 0.8nm (8.52%coverage) that means that 42% of prothrombin dissociated from the lipid bilayer.

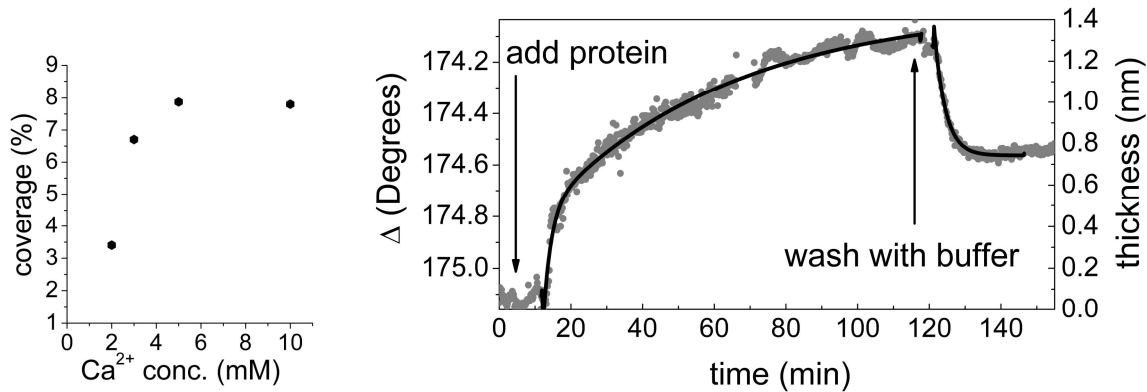


Fig.5.6 a) The dependency on Ca^{2+} concentration of the surface coverage during adsorption of prothrombin ($1.8\mu\text{M}$) on 4:1 POPC/POPS lipid bilayers; b) time course dependence of the ellipsometric angle Δ and of the corresponding protein average thickness (estimated from the fitting procedure to the mathematical model with fixed optical constants) during the process of prothrombin adsorption ($2.8\mu\text{M}$) on 4:1 POPC/POPS lipid bilayers at saturating Ca^{2+} concentration (5mM) and during the reverse process of desorption initiated by washing the surface with protein-free buffer at the same Ca^{2+} concentration. The gray dots represent the experimental data while the continuous lines are the theoretical fits.

Rate constants of prothrombin binding to POPC/POPS membranes

As results from fig.5.6.a, very low surface coverage with prothrombin was attained under the experimental conditions that were employed in the ellipsometric measurements such that one can consider that the individual binding sites are independent from each other. The rate constants of the adsorption process can be therefore extracted by fitting the time course dependency of the ellipsometric angle Δ with the exponential equation of the Langmuir approach:

$$\delta\Delta(t) = \delta\Delta_e [1 - \exp(-(t - t_0)/\tau)] \quad (5.1)$$

were the difference in time $\delta\Delta(t) = \Delta(t) - \Delta_0$ and the equilibrium value $\delta\Delta_e = \Delta_e - \Delta_0$ are related to the initial/starting value of the measured ellipsometric angle Δ_0 . The rate constant $k = 1/\tau$ is dependent on the protein concentration in the bulk phase and contains information about the adsorption rate k_{on} and the desorption rate k_{off} .

At a constant concentration of prothrombin ($1.9\mu\text{M}$), Ca^{2+} -dependent measurements (Fig.5.5b) show an increase in the rate constant with the calcium concentration, from $k=0.096\text{s}^{-1}$ in 2mM CaCl_2 containing buffer to $k=0.262\text{s}^{-1}$ in 3mM CaCl_2 containing buffer. For higher concentration of protein in solution ($2.8\mu\text{M}$), at calcium saturation (5mM), the adsorption reveals a biphasic behavior (Fig.5.6) with the rate constants $k_1=0.45\text{s}^{-1}$ and $k_2=0.018\text{s}^{-1}$. Anomalous binding at high protein concentrations was also reported by Wei et al. who performed stopped-flow light scattering experiments on prothrombin adsorption to lipid bilayer vesicles⁸⁴. It is questionable whether the slow adsorption component reflects the existence of a second class of low affinity binding sites or the sites show variable rate constants at different degrees of phospholipid saturation.

Another explanation for the two rates adsorption process might reside in the observation that before binding, prothrombin undergoes calcium dependent conformational changes at two distinguishable rates. However, the values of these rates (one of which is 0.00046s^{-1} at 10°C ⁸²) are not known for the room temperature such that one could make a correlation with the adsorption rates measured by ellipsometry.

Fitting the exponential decay of the Δ change during the prothrombin desorption (while washing with protein free buffer) results in the dissociation constant $k_{\text{off}}=0.32\text{s}^{-1}$ at a constant concentration of CaCl_2 of 5mM (Fig.5.6). Much faster was the desorption process ($k_{\text{off}}=0.69\text{s}^{-1}$), when additionally, the calcium concentration of buffer was decreased from 10mM to 1mM (Fig.5.5 b). In the latter case, the desorption of proteins is not only due to the intrinsic binding reversibility. The drop in calcium concentration affects the stability of the active configuration of prothrombin and also affects the lateral organization of lipids in the membrane such that high affinity binding sites are dissolved and therefore the proteins dissociates rapidly from the bilayer.

Roughly approximated, the fast rate constant of association k_{on} can be derived from the formula of the concentration-dependent rate $k(c_{\text{prot}}) = k_{\text{on}} c_{\text{prot}} + k_{\text{off}}$. The resulting value is $k_{\text{on}}=4.6 \cdot 10^4 \text{ M}^{-1} \text{ s}^{-1}$ and the reversible binding constant calculated as $K=k_{\text{on}}/k_{\text{off}}$ is therefore $K=1.43 \cdot 10^5 \text{ M}^{-1}$.

As compared to previous studies that involve bilayer vesicles and FRET or light scattering techniques, the advantage of using ellipsometry for investigation of prothrombin adsorption on planar, solid supported lipid bilayers is that the process can be monitored at increased Ca^{2+} concentrations without any artifact or limitation determined by calcium-induced aggregation of vesicles. The reversibility of prothrombin adsorption could be monitored in real time and mostly the mass transport limitation may potentially prevent from accurate determination of the rate constants that are governing the process of interaction between the proteins and the lipid membrane. This limitation could be however dismissed if, for reversible adsorptions, equilibrium coverage fluctuations at intermediate coverage (less than 20%) could be experimentally analysed via a highly sensitive technique, as theoretically described in the Section 1.4.

5.3 Conclusions

The adsorption of annexin A1 on solid supported lipid membranes of different compositions was visualized with AFM. The height increase of the PS-enriched domains after addition of the protein and rinsing with buffer confirmed that annexin A1 adsorbs irreversibly, in a Ca^{2+} -dependent manner, to those areas of the membrane that concentrate locally the acidic phospholipids. Ternary lipid bilayers containing mixtures of charged and uncharged lipids in gel and fluid phase were employed in order to discriminate between calcium-induced and protein-induced lateral reorganization of the lipids. Although in the presence of high calcium ions concentrations no lateral phase separation occurred in membranes with low content of anionic lipids, AFM images reveals irreversible adsorbed domains of annexin A1. This observation implies that annexin A1 may induce clustering of PS molecules into areas with high binding affinity that are underlying the protein domains.

The calcium dependency of prothrombin adsorption onto anionic fluid membranes was investigated by means of ellipsometry. A saturation concentration of 5mM CaCl_2 was found for 4:1 POPC/POPS bilayers. Under these conditions, 42% of prothrombin adsorbs reversibly to the membranes while the rest of 58% of Ca^{2+} -mediated PS-Gla complexes remain stable.

The rate constants that are governing the adsorption process were determined through a simple Langmuir approach at low surface coverage. At higher concentrations of prothrombin (2.8 μM) the adsorption is biphasic, at two distinct rates: $k_1=0.45\text{s}^{-1}$ and $k_2=0.018\text{s}^{-1}$.

Chapter 6

Fast imaging with conventional AFM for detecting surface coverage fluctuations: pitfalls and drawbacks

For real-time observation of the dynamic behavior of a sample surface, high speed imaging with atomic force microscopy (AFM) may offer the optimal solution due to its high spatial resolution and large applicability, regardless to the imaging conditions (air or liquid) or to the sample properties (conducting or non-conducting material). The employment of fast scanning AFM for recording equilibrium coverage fluctuations in the process of reversible adsorption of proteins on lipid membranes is considered in the following. This challenging experimental approach would allow, according to the new detection scheme that was theoretically proposed by Lüthgens ⁷, to determine precisely, from one single experiment, the rate constants that are governing the adsorption process, without interferences from mass transport, depletion, or high surface coverage phenomena.

From Eq.1.3 it results that the fluctuations amplitude of the surface coverage is reverse proportional with the investigated surface area and it reaches the maximum at 20% coverage. Therefore, as sensing areas, small membrane domains or patches on that the proteins adsorb selectively are necessary for imaging with AFM at high scanning rates. Prothrombin, for instance, adsorbs reversibly on lipid bilayers that contain PS lipids. The experimental conditions (protein concentration, buffer properties) for attaining low to intermediate coverage on lipid bilayers with 4:1 PC/PS lipid content were investigated by means of ellipsometry in Section 5.2. In order to decrease and also differentiate the surface area that is available for protein adsorption, ternary lipid membranes exhibiting gel phase domains enriched in PS molecules were spread on silicon substrate. The lipid content of the membrane was calculated to maintain the ratio 4:1 of zwitterionic/anionic lipids (DPPC/DPPS) in domains surrounded by the fluid phase of POPC molecules. Subsequent addition of proteins (i.e. prothrombin) would result in a low surface coverage (15%) of the domains area. Continuous and repetitive AFM imaging of a single domain should be performed at high scanning speed in order to monitor the equilibrium coverage fluctuations. A Lorentzian fit can be applied to the Fourier transform of the acquired data only if the duration of repetitive scanning is long enough to cover the low frequency region that comprise information about the adsorption rates (Fig1.5).

The main aspects that have to be specifically considered in this experimental approach for recording equilibrium coverage fluctuations during reversible adsorption of proteins

on lipid membranes, via fast scanning with a conventional AFM, are discussed in the following.

6.1 Thermal drift and small scan areas

The overall drift in AFM measurements is generated by probe displacement relative to the sample and may affect significantly the results of experiments, especially when the size of the sample becomes comparable with the drift's magnitude. In this work, a commercially available AFM-MFP 3D (Asylum Research) was employed for fast scanning in liquid at room temperature (20-22°C), under normal laboratory conditions. For testing purposes, the sample was a solid supported lipid membrane exhibiting gel phase domains that are about 1.2nm higher than the surrounding fluid phase. A small defined area (0.4x1.2µm) of the bilayer was consecutively imaged (128x512pixels) in contact mode at a scan frequency of 3.9Hz (4.68µms⁻¹) which corresponds to 33s per frame. One can see in Fig.6.1a that after about 5 min of operation, already in the 9th acquired image, a certain object (in this case a lipid domain) selected on the sample surface is going to move out of the scanning area since the global drift is exceeding the scanning range. The drift velocities $S_{x-drift}$ and $S_{y-drift}$ along the X and Y scan axes are calculated from consecutive scanned images and represented in Fig.6.1b. One can observe that the values of the drift velocities are variable in time and independent on the scanning direction. The main reasons for the spatial uncertainty associated with the AFM and its piezoelectric drive mechanism belong inherently to any ceramics used in piezoscanners (that show hysteresis, creep and non-linearity) as well as to the thermal drift generated by the thermal gradient of the environment. Although the overall AFM drift is an integration result of several factors, thermal changes in the ambient conditions are the most influential. They cause the mechanical length variation of the PZT actuator, cantilever-tip and sample platform such that the AFM probe or the sample is displaced from the initially observed position.

Drift measurements and compensation are important to keep AFM operations stable and reliable. Despite of the variability in time of the drift velocities, the derivative $dS_{x-drift}/dS_{y-drift}$ is nearly constant such that the 2D trajectory of the drift is almost rectilinear and can be calculated as shown in Fig.6.1c. One can observe that during about 10 min of repetitive scanning of the same area, a given dot (punctual object) on the sample is still visible if the size of the scanning area is at least 250x800nm. However, the lipid domains that need to be investigated do have a certain area (in the range of some hundreds nm²). The direct solution for maintaining the object of interest in the scanning frames by enlarging the scanned area in the detriment of the imaging frequency may be not satisfactory if the final purpose is to detect fast coverage fluctuations. The time course variations of the drift velocities along X and Y scan axes are relatively small as compared to their absolute values. This is mainly observable from the representation as a function of time of the global drift along the drift direction and along X and Y scan axes (Fig.6.1.d). The temporal dependency of the global drift is mostly dictated by the global drift along the Y direction which is considerably larger than that along the X direction.

To maintain the object of investigation (the lipid domain) into the chosen frame of the small scanning area, there would be the need to sequentially shift the position of the

AFM probe, after each scan, along the opposite direction of the drift. This direction is given by the calculated slope from Fig.6.1c while the necessary shift size of the AFM probe position is weighted, at any given time, by the slope values extracted from the line fits in Fig.6.1d assuming a constant scanning rate for all AFM images. These values are however very much dependent on the way how changes in the environmental conditions take place. They can not remain constant or be reproducible in a very long range of time (hours or days) if a minimal control over the ambient conditions is not maintained. The corrections for the AFM probe position would not apply if temporal variations in the temperature gradient fluctuate randomly between positive and negative values such that the drift trajectory remains unpredictable.

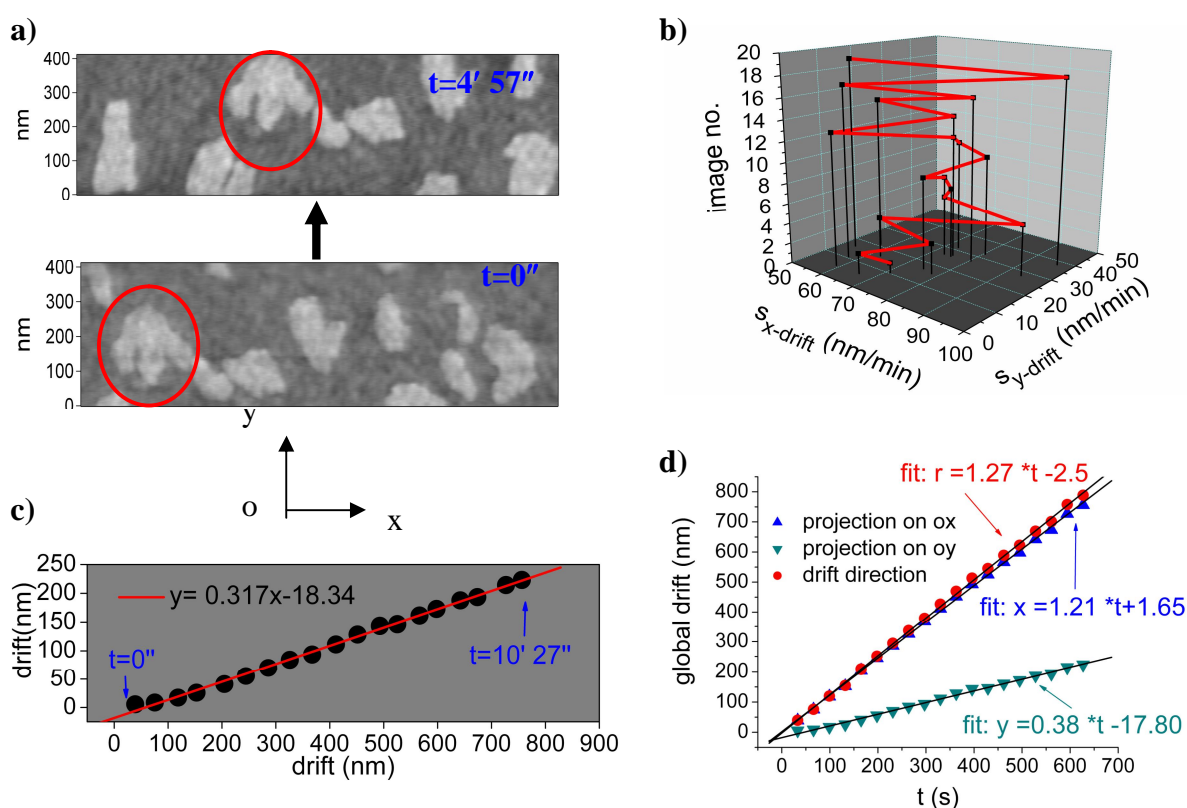


Fig.6.1 a) The 1st and 9th images (128x512pixels) from an AFM-CM scan series of lipid membrane domains, performed at a scan frequency of 3.9Hz ($4.68\mu\text{ms}^{-1}$) which corresponds to 33s per frame. As the operation time passes (4min and 57s) the selected domain is moving out of the scanning area because the drift is exceeding the scanning range; b) representation, for each consecutively scanned AFM image, of the drift velocities $S_{x-drift}$ and $S_{y-drift}$ along X and Y scan axes respectively; c) the drift trajectory obtained from the calculated values of the drifts along X and Y scan axes during continuous scanning of the sample, for 10 min and 27 s, without changing the scanning parameters. The linear fit (red line) may predict the drift direction for the time range of several minutes; d) time dependencies of the global drift along the drift direction r and along X and Y scan axes. The slopes of the linear fits (continuous lines) may be used as weighting factors for the corrections of the AFM probe position at any given time.

A rigorous environmental control by placing the AFM in a temperature-controlled chamber can greatly reduce the thermal drift although, to a certain extent, other sources, i.e. the instrumental noise, may generate effects that are similar to that of the thermal drift.

There are several studies, especially in the area of nano-manipulation, that explore potential methods for drift compensation, most of them being based on the assumption that the drift velocities remain constant^{85,86}. Yang et al. have proposed a compensation scheme that is based on block phase correlation and uses multilayer neuronal networks for drift prediction⁸⁷.

Currently there are extensive efforts for minimization of the mechanical and thermal drift effects on newly built AFMs. As the main reason for the thermal drift is unequal displacements of several components of the system, the selection of materials is done such as, by combination of the thermal expansion and thermal conductivity coefficients, the principle of "self compensation" can be applied in a carefully chosen overall system geometry.

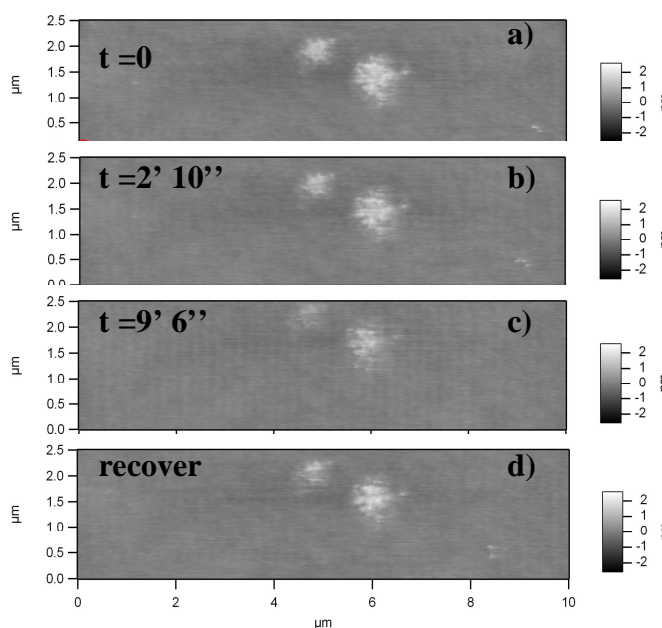
6.2 Image resolution and long-time imaging stability and repeatability

For recording surface coverage fluctuations, repetitive imaging of the sample at high scan rates is required over an extended time range. Although the conventional AFM-MFP is capable of imaging samples in liquid at high resolution, the suitable scan speed has normally low values, mostly because of the limited bandwidth of the PI-controlled AFM given by the main dynamics of the piezo scanner. Faster scan speeds would result in oscillations of the scanner. The instabilities of the closed loop AFM system consisting of the scanner, the cantilever, the photodiode, and the controller system cause oscillations that distort the topography images. If the PI feedback settings are set low enough to avoid the oscillations i.e. in CM imaging, the cantilever deflections around the setpoint value increases and this may damage the sample.

Soft samples such as proteins adsorbed to lipid membranes are sensitively affected by the interaction force with the scanning tip. In tapping mode, this force can be minimized by using small free oscillations amplitude of the cantilever and a shallow setpoint. Fig.6.2 shows images of Anexin A1 domains adsorbed on lipid membrane (80%POPC, 16%DPPC, 4%DPPS) from an image series recorded with AFM-MFP at a scan frequency of 4.88 Hz (26s per frame) over a long time range. Imaging was performed in TM with silicon nitride tips mounted on cantilevers (OMCL-TR400PSA Olympus) with a nominal spring constant 0.08N/m and 7.4 kHz resonance frequency in water. One can observe that the image accuracy decreases in time. After about 9min of continuous and repetitive scanning without changing the settings, the domains appear smaller and the surface topography is not any more followed rigorously by the scanning tip (trace and retrace curves differ more and more). In some cases the oscillating cantilever tip may even dissociate completely from the sample surface and the sample topography information gets lost. The initial image could be recovered only after readjusting the setpoint (Fig.6.2d). The observed effect is mainly a cause of the drift in the cantilever excitation efficiency. Lower excitation efficiency induces decreased oscillation amplitude that is interpreted by the

feedback system as a stronger tip interaction with the sample. In consequence the sample stage is withdrawn from the tip. The stability of the excitation amplitude is decisive for the success of successive imaging with maintained small tapping force. Unfortunately, the drift in the free oscillation amplitude can not be directly monitored during the scanning process. A drift compensation method was recently proposed by monitoring the drift in the second harmonic amplitude of cantilever oscillation averaged over a period longer than the image-acquisition time⁸⁸. This drift compensation together with the newly invented "dynamic PID controller" whose gains can be automatically changed depending on the cantilever's oscillation amplitude, allow stable high speed imaging with maintained weak tip-sample interaction.

Fig.6.2 Images of Annexin A1 domains adsorbed on lipid membrane (80%POPC, 16%DPPC, 4%DPPS) from an image series recorded continuously with AFM-MFP at a scan frequency of 4.88 Hz (26s per frame) during several minutes. The selected images are obtained at (a) $t=0$, (b) $t=2'10''$, (c) $t=9'6''$ without changing the scan settings and (d) after readjusting the setpoint. Imaging was performed in TM with silicon nitride tips mounted on cantilevers having a nominal spring constant 0.08N/m and 7.4 kHz resonance frequency in water. The initial image could be recovered after readjusting the amplitude setpoint (d).



Commercially available AFMs require typically several seconds up to a minute or more to acquire a single image. A crucial issue in AFM development is the increase of the imaging speed. Several alternative solutions were widely proposed for enhancing the scan speed of AFM without detrimental effects on the image quality, such as introducing additional high frequency piezo segments to the probe⁸⁹⁻⁹¹ or to the scanner⁹² or by implementing a modern model-based feedback controller⁹³. To speed up the response of the probing tip one can use small cantilevers with very high resonance frequencies⁹⁴⁹⁵ or one can reduce the quality factor of the probes^{96,97}. Viani et. al⁹⁴ have reported the ability to produce repeated tapping-mode images ($1 \times 1 \mu\text{m}^2$) of DNA adsorbed onto mica using a new prototype AFM with small cantilevers, at an acquisition time of 1.7 s per image. Small cantilevers allow faster imaging because they have higher resonant frequency in liquid (>100kHz) and lower coefficients of viscous damping which permit high-tapping frequency. Also, due to their low spring constant (<0.5N/m), the sample damage is minimized.

Ando et al. has developed, over several years, devices that are optimized for high-speed AFM-TM scanning in order to capture the dynamic behavior of biomolecules⁹⁸. Now, the most advanced tapping-mode high speed AFM that is available in this group can capture

images on video at ~30-60 ms/frame for a scan range of 250nm under feed-back operation capable of preventing sample disturbances from the scanning tip ⁹⁹.

6.3 How fast? How long ? – a matter of the chosen system

Considering the previously estimated adsorption kinetics of different proteins, the applicability of the available AFM-MFP for detecting surface coverage fluctuations at adsorption equilibrium may be theoretically evaluated. Monte Carlo simulations based on the random sequential adsorption (RSA) model were performed in this study and then analyzed according to the detection scheme proposed by Lüthgens ⁷. Two different proteins were selected here: prothrombin and a His-Tagged protein. The adsorption kinetics of prothrombin to lipid membranes was described and investigated in the section 5.2 ($k_{on}=4.6 \cdot 10^4 M^{-1}s^{-1}$, $k_{off}=0.32s^{-1}$). His-Tagged proteins are proteins that contain a hexa histidine-tag at the C- or N- terminus. Their binding to supported lipid bilayers containing NTA-lipids, after saturating all NTA sites with nickel, was monitored in real time with an acoustic wave guide device ¹⁰⁰. The resulting rate constants for a His-Tagged protein (12,500Da) are $k_{on}=2.56 \cdot 10^4 M^{-1}s^{-1}$ and $k_{off}=1,3 \cdot 10^{-3}s^{-1}$. Fig. 6.3 presents the calculated power spectra of equilibrium coverage fluctuations that results from MC simulations performed for both proteins: prothrombin and His-Tagged protein.

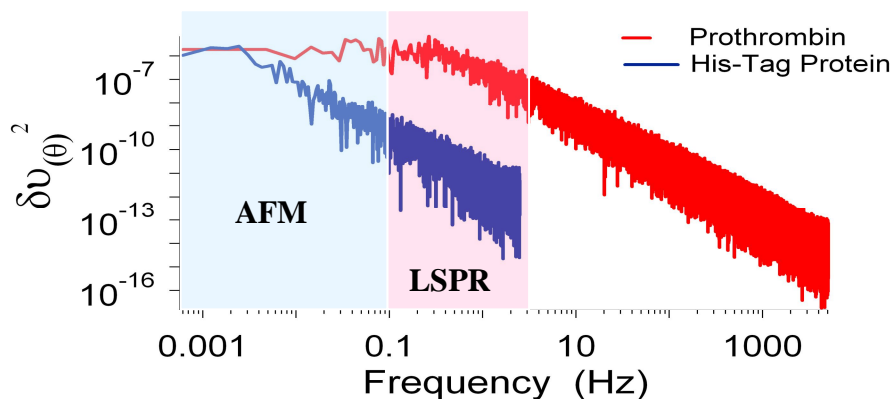


Fig.6.3 Power spectra of equilibrium coverage fluctuations obtained from MC simulations performed for prothrombin ($k_{on}=4.6 \cdot 10^4 M^{-1} s^{-1}$, $k_{off}=0.32s^{-1}$, $\rho=1.69 \cdot 10^{15}$) and His-Tagged protein ($k_{on}=2.56 \cdot 10^4 M^{-1} s^{-1}$ and $k_{off}=1,3 \cdot 10^{-3} s^{-1}$, $\rho=2.41 \cdot 10^{13}$). The blue shadowed area delimits the applicability range as concern the temporal resolution of the available AFM-MFP. Faster and highly sensitive optical techniques based on LSPR may apply for detection of equilibrium coverage fluctuations of proteins with fast adsorption kinetics (red shadowed area).

Low surface number densities (ρ), that reflect the protein bulk concentrations, are required in order to avoid the jamming limit and moreover, to maintain an equilibrium

coverage ($\langle \theta \rangle$) around 0.2 such that the amplitude of the fluctuations is maximal. For experimentally obtained data, the binding constants that are governing the adsorption process may be extracted from the Lorentzian fit applied to the power spectra ⁷:

$$\langle \delta\theta(\nu)^2 \rangle = \frac{4\tau \langle \theta \rangle \pi a^2 (1 - 4 \langle \theta \rangle)}{A [1 + (2\pi\nu\tau)^2]} \quad (6.1)$$

Binding and unbinding constants k_{on} and k_{off} are included in the time constant τ that sets the level of the time resolution required by an experimental setup for detecting the equilibrium coverage fluctuations. The amplitude of these fluctuations increases proportionally with the surface area (a) of the proteins and are larger for smaller detection areas A . As it's resulting from Fig. 6.3, in the case of His-Tagged protein, repetitive scanning with AFM at about 10s to 20s per frame may allow, in principle, to record the equilibrium coverage fluctuations. Continuous and repetitive imaging is however required for at least 16 minutes such that enough data points are captured in the low frequency region that comprises the information about the adsorption rates. Under these conditions (long and repetitive fast scanning of small areas) the problems generated mainly by the overall AFM drift and system instability prevent the stable acquisition of images at high spatial resolution, simultaneously maintaining a weak sample-tip interaction. Proteins with faster adsorption kinetics, such as prothrombin, shift the power spectra to the higher frequencies and therefore a better time resolution (one data point per second or even less) is required for the experimental setup in order to monitor the fluctuations.

Highly sensitive and non invasive optical techniques such as those based on localized surface plasmon resonance (LSPR), that imply very small detection areas, are appealing as potential experimental approaches for detecting the equilibrium coverage fluctuations of proteins, as it will be described in the next chapters.

6.4 Conclusions

The employment of fast scanning with a conventional AFM-MFP (Asylum Research) for recording equilibrium coverage fluctuations in the process of reversible adsorption of proteins on lipid membranes was considered.

Although the conventional AFM may capture images with high spatial resolution, their relatively long acquisition times (from several seconds up to a minute) do not allow for recording fast fluctuations that occur on a much shorter time scale (seconds and milliseconds). The resonance frequency of the cantilever and the bandwidth of the z scanner are the main rate limiting factors of the standard AFM operating in tapping mode.

From MC simulations based on RSA model, it results that in the case of proteins with slower adsorption kinetics, a temporal imaging resolution of several seconds per frame may be satisfactory for detecting the equilibrium coverage fluctuations if data points are repetitively acquired over a range time of several minutes (i.e. minimum 16 min for His Tagged protein). It was shown, in the efforts to scan small areas of soft samples at fast scan rates with maintained weak tip-sample interaction, how the thermal drift and the drift in the cantilever excitation efficiency impede the repetitive and stable image acquisition. Newly designed high-speed AFM prototypes together with small cantilevers having high resonance frequency in liquid and lower coefficients of viscous damping may, however, overcome most of the problems that are encountered with a conventional AFM during fast scanning.

Highly sensitive and non invasive optical techniques such as those based on localized surface plasmon resonance (LSPR) may offer an alternative and less expensive solution for designing sensors that are able to monitor the equilibrium coverage fluctuations in protein adsorption.

Chapter 7

Nanostructuring Gold Surfaces

In many applications of nanostructures, fabrication is the first challenge to their realization.

There is so far no universally applicable method for nanostructuring materials. Each nanofabrication method has significant limitations and therefore one should choose and develop the most suitable method in order to produce the desired nanostructures.

Direct write methods like electron-beam lithography, focused ion beam lithography or X-ray lithography are currently used to pattern solid surfaces with regular arrays of nanometer scale features. Scanning probe lithography offers an excellent control over the nanoscale structures. However, these methods are slow serial approaches (one structure is created at a time) that require long times for fabrication of extended areas or dense patterns of nanostructures. Replication techniques, i.e. photolithography or soft lithography (based on stamping) are very attractive as serial processes, suitable for large scale fabrication but with limited resolution (the smallest feature replicated in photolithography is limited by the wavelength of the light while in soft lithography the mechanical properties of the stamp and the physical interaction between the stamp and the substrate are dictating the ultimate resolution).

An increasing challenge nowadays is to fabricate large areas/volumes of nanostructured materials with good control over the size of the nanoparticles and the interparticle spacing.

In the following sections (7.1-7.3) I will show how I have employed nanosphere lithography for constructing extended areas of nanostructured gold surfaces that can be used as optical sensitive substrates for the detection of changes in the dielectric properties of their local environment.

Dependent on its topography (i.e. periodic or random arrangement), the nanoparticles' array manifests different optical properties as compared to the individual nanoparticles. Regular arrays of nanoparticles can exhibit interesting physics resulting from the collective behavior of the interacting nanostructures. Investigation of 2D-arrays with different interparticle spacing makes possible to exploit the amazing optical properties of nanoparticles using conventional methods for bulk materials (e.g. absorption spectroscopy).

7.1 Nanosphere lithography

Nanosphere lithography (NSL) is a bottom-up approach for fabrication of periodic nanostructures, using self-assembled polystyrene nanospheres as templates. Inexpensive and inherently parallel, NSL is an attractive technique for producing well-ordered nanoparticle arrays, that provides control of interparticle spacing and out-of-plane height to the level of a few nanometers.

In the first step, polystyrene nanoparticles were used as building blocks for the synthesis of long-range-ordered monolayers and films of colloidal nanocrystals. Colloidal crystallization is induced by attractive capillary forces present between particles at the solid-liquid-gas contact line (Fig.7.1a). In the second step, a thin film of deposition material was deposited to a certain mass thickness over the nanosphere-coated substrate. At last, the polystyrene nanospheres were removed by chemical or mechanical means. The deposition material that was filling the threefold holes of the nanospheres mask remains on the substrate and forms the periodic particle array (Fig.7.1b).

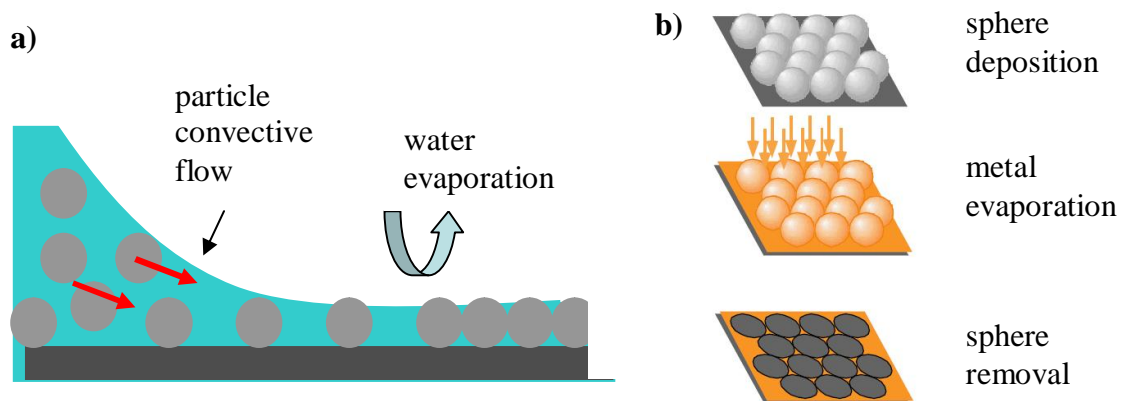


Fig. 7.1 Schematic representation of: a) 2D-colloidal crystallization process at the solid-liquid-gas contact line, and of b) the main steps followed in NSL technique.

In Fig.7.2 is shown the scanning electron microscopy image (SEM) of a monolayer of hexagonally close-packed nanospheres of 500 nm diameter formed on freshly cleaved mica substrate. The deposition conditions and the properties of the underlying substrate are of a critical importance for long-range nanosphere ordering. Optimization of several parameters like the wettability of the substrate, the solvent evaporation rate or the particle volume fraction in the suspension was performed in order to obtain monolayers of polystyrene beads in a honeycomb arrangement on large areas.

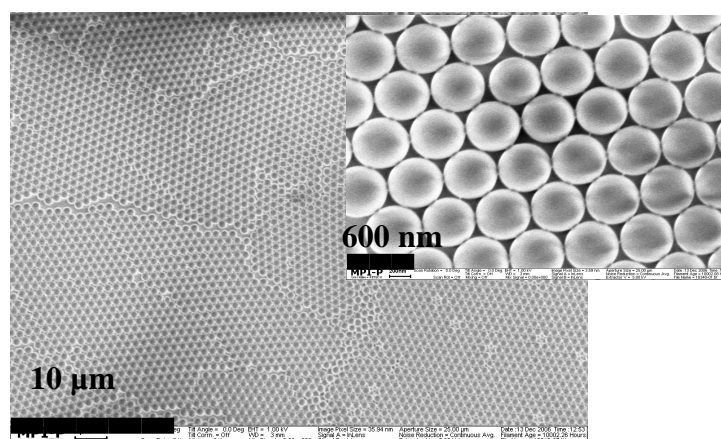


Fig.7.2 Large and detail SEM images of the deposition mask formed by self assembling polystyrene beads of 500 nm diameter in a hexagonally close-packed pattern on freshly cleaved mica substrate

In the following, the method of nanosphere lithography is applied to fabricate highly regular arrays of nanometer-scale gold structures as well as two-dimension random arrays of nanoscopic holes perforated in metallic films. The structural properties of these metallic nanostructures were investigated with atomic force microscopy.

7.2 Regular arrays of triangle shaped gold nanoparticles

The sample preparation procedure was adapted from the drop-coat method of nanosphere ordering as employed in Van Duynne research group¹⁰¹. The deposition mask was formed either on highly hydrophilic glass substrate or on freshly cleaved mica by self-assembling polystyrene nanospheres into a hexagonally close-packed two dimensional colloidal crystal. In order to find their lowest energy configuration, the nanospheres have to be able to diffuse freely across the substrate. This could be achieved using polystyrene nanospheres having a chemically modified surface with sulfate groups.

As in all naturally occurring crystals, nanosphere masks include a variety of defects that arise as a result of nanosphere size polydispersity: site randomness, point defects (vacancies), line defects (slip dislocations), and polycrystalline domains. Defect free areas are typically in the range of 10-100 μ m.

At high particle volume fraction in the suspension (higher than 2.5%) the tendency for multilayer formation was observed. The number of colloidal layers increased usually in a stepwise fashion from the edge to the center of the crystal (Fig.7.3a). The number of layers was increasing with the suspension concentration, independent on the solvent evaporation rate. At higher magnification, SEM images (Fig.7.3b) show also vacancies in the colloidal monolayer or fracture lines rising at the point where a bead has a different (larger) size.

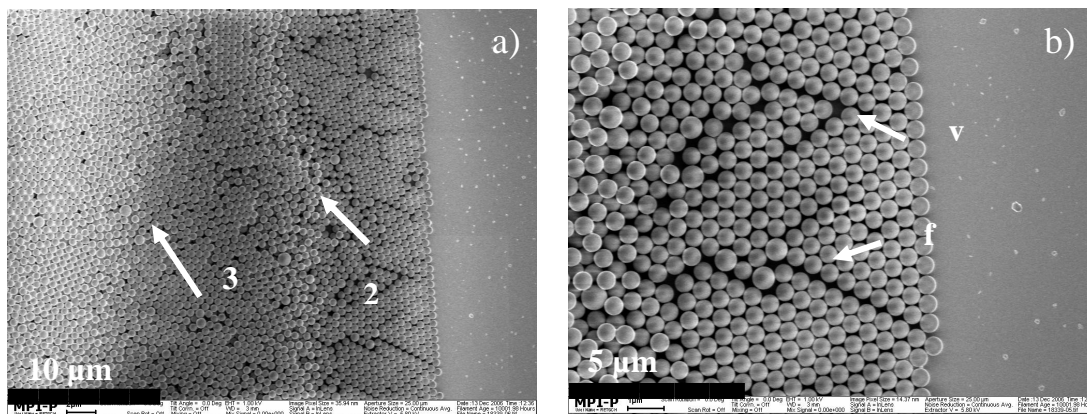


Fig.7.3 SEM images (large and detail views) of polystyrene nanospheres self assembled on glass substrate at a high volume fraction in the suspension (2.5%); a) The number of colloidal layers increases from the edges to the center of the crystal; the arrow 2 and the arrow 3 mark, respectively, the borders from that the second layer and the third layer start to crystallize; b) defects in the monolayer structure: the arrows show a vacancy (v) and a fracture line (f) starting at the point where a particle of a larger size is present.

At too low concentrations of polystyrene nanoparticles in solution (lower than 0.2% w/w), the substrate is covered only partially with isolated islands of monolayer beads. With increasing volume fraction of nanoparticles the islands elongate and interconnect with each other (Fig.7.4).

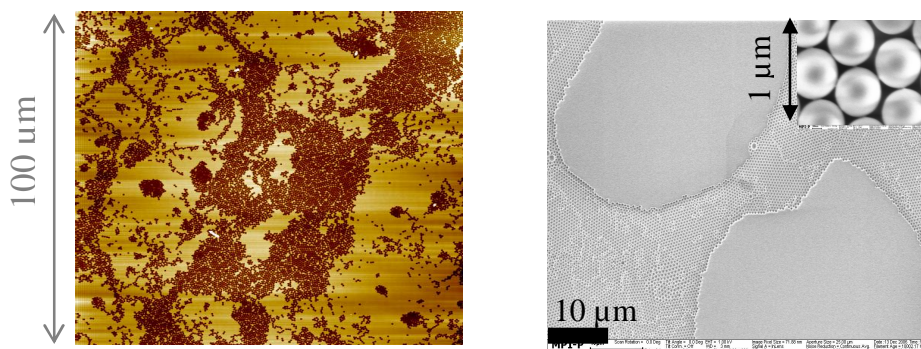


Fig.7.4 AFM image (left) and SEM image (right) of the deposition mask formed, respectively, on hydrophilic glass and on mica substrate at a low volume fraction of nanoparticles in suspension (0.6 %). The AFM image represents the “negative” picture of the mask that was removed from the substrate after evaporation of a thin gold layer (60nm). The dark areas correspond to the remaining voids in the gold layer after the removal of the polystyrene beads. The inset of the SEM image shows, in detail, the local arrangement of the latex beads (500nm diameter) used to form the 2D mask.

Similar structures of aggregates with local honeycomb arrangement of nanoparticles were obtained in similar conditions for much smaller polystyrene spheres of only 110 nm diameter (Fig.7.5).

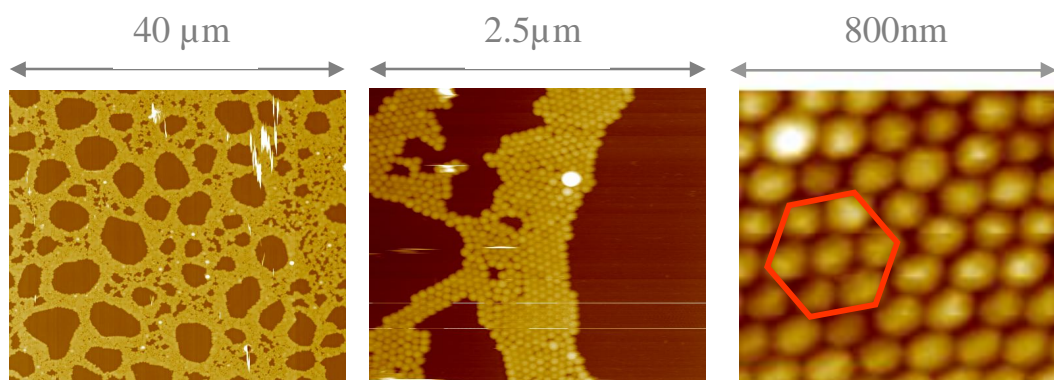


Fig. 7.5 The structure of 2D-aggregates of polystyrene beads (110 nm diameter) imaged with AFM on different scan areas (40 μ m, 2.5 μ m and 800nm) in contact mode (after evaporation of a thin gold layer-20nm thickness). The substrate was hydrophilic glass. The nanoparticles self assemble locally in the known nano honeycomb arrangement.

The topography of the final structure is strongly dependent on the solvent and on the substrate properties via the evaporation rate and the friction between the nano-beads and the surface. Of a crucial importance for obtaining large areas of periodic nanostructures is also the monodispersity in size and shape of the nanoparticles suspension.

Mica and hydrophilic glass were chosen as substrates in this work and the mask deposition conditions were optimized in order to obtain large and homogenous areas of regular nanoparticle arrays. In comparison to the glass substrates, mica surfaces favor a better packing of polystyrene spheres that have chemically modified surfaces with negatively charged functional groups. This is most probably due to an easier sliding (corresponding to very low friction) of the nanobeads on the mica substrates.

A better rearrangement of the nanobeads on the surface during solvent evaporation was observed when surfactant, Triton X-100 and methanol (1:400 v/v) was added in a 1:4 ratio to the aqueous solution of nanospheres before drop coating. The optimal concentration of polystyrene nanoparticles was 1.3 % solid for lithography performed at room temperature under normal lab atmosphere.

Prior to use, the glass substrates were treated in piranha solution (1:3 30% H₂O₂:H₂SO₄, 30 min at 80°C) that render them highly hydrophilic. However, under similar conditions (e.g. solvent and concentration of the colloidal suspension, the disposition angle of the substrate and the temperature and humidity of the surroundings) the polystyrene nanobeads are packing better, and on larger areas, on the mica substrates.

Following the formation of the deposition mask, the samples were mounted in a vapor deposition chamber system (Balzers BAE vacuum coating system) where gold films of controlled thicknesses (usually between 20-100 nm) were thermally evaporated onto the substrate at slow rates (0.03 nm/s), under very low pressures (3×10^{-6} mbar). A thin layer of chromium (3-5 nm) was used to promote the adhesion of the gold film to the underlying substrate. Removal of the gold capped nanospheres by sonication in ethanol,

tape stripping or washing with dichloromethane results in a patterned substrate with repeatable spaced metallic nano-triangles as shown in the AFM images of Fig.7.6.

In order to check the surface topography, atomic force microscopy images were taken with NanoscopeTM III (Digital Instruments) using silicon nitride probes (OTR8 Veeco, USA) with 36° side angle and 20nm effective radius of the curvature at the tip. The in-plane sizes of the imaged nanoparticle are slightly overestimated, mainly because of the tip-induced broadening effects.

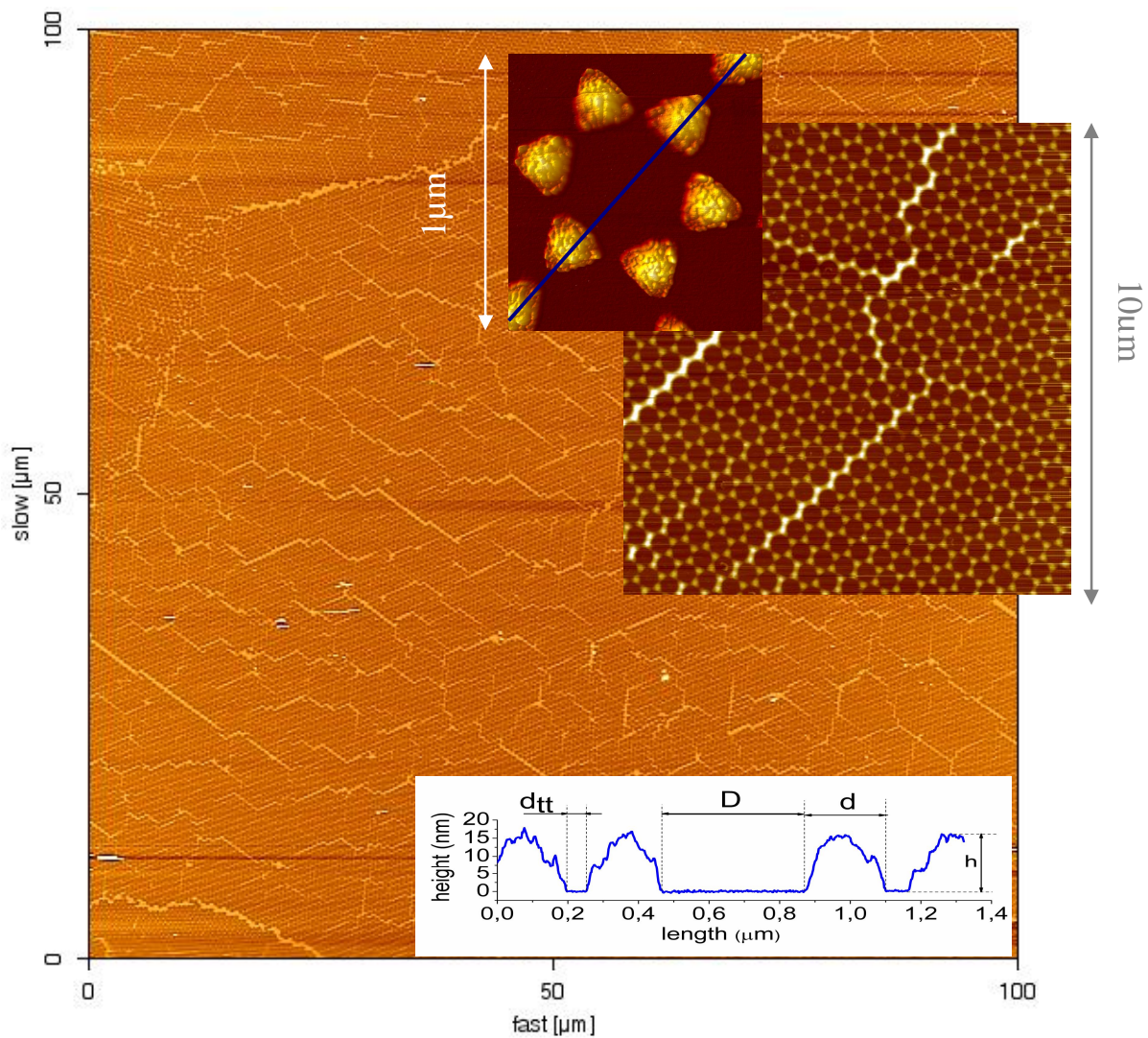


Fig. 7.6 Large and close view of the regular array of triangle shaped gold nanoparticles imaged with AFM on different scanning areas. The line cross section characterizes the nanoparticles with a normal bisector $d=203\text{nm}$, out of plane distance $h=19\text{nm}$ and tip to tip distance between the triangles $d_{tt}=56\text{nm}$.

Calculations based on discrete dipole approximation (DDA) have shown a considerable increase of the electric field around the edges of a truncated tetrahedron in comparison

to the local electric field around the spheres or ellipsoids³⁶. For sensing purposes (in terms of detection of small changes in the local dielectric environment) the geometry of the plasmonic particles is essential in setting their resonance frequency and their spectral sensitivity defined as the shift of the resonance wavelength per refractive index unit. The resonance wavelength can be also tuned over a large range of values by choosing the appropriate aspect ratio which, for triangle shaped nanoparticles, is given by the ratio between the length of the triangle's perpendicular bisector d and the measured out-of-plane height h . Nanosphere lithography is particularly useful in this regard. The size of the nanoparticles can be easily adjusted according to the diameter D of the employed polystyrene nanospheres and to the thickness of the deposited gold layer.

NSL method can be applied for the fabrication of periodic arrays of nanoparticles made of different metals. Silver, for instance, although liable to fast oxidation is of a particular interest for construction of biosensors based on LSPR due to its exquisite sensitivity to the dielectric nanoenvironment.

7.3 Random arrays of nanoholes in thin gold layers

NSL was also employed for fabrication of short range ordered arrays of nanoholes in thin gold layers on glass substrates. To this end, a similar approach as previously described was adopted except for the technique of formation the deposition mask which was modified. To obtain individual nanoholes at controlled distances from each other, a submonolayer mask made of polystyrene nanospheres was electrostatically self-assembled on a chemically treated cover glass (Fig.7.7a). The characteristic distance between the spheres could be tuned through the salt concentration in the colloidal solution. Low surface coverage was achieved by kinetically interrupting the particle adsorption on the substrate. Different suspensions of size monodispersed latex nanospheres (diameter from 50 nm to 110nm) with sulfate modified surface were tested. The smaller is the nanospheres diameter the more problematic is the size monodispersity issue because of the residual synthesis products that are present in the nanoparticles suspension (Fig.7.7b). Size polydispersity of the resulting nanoholes determines inhomogenous broadening effects on the measured extinction spectra of the array, with direct influence on the sensitivity of the LSPR detection method. However, employing single particle spectroscopy this problem is optimally solved and the highest sensitivity can be reached if individual nanoholes are considered as sensing elements

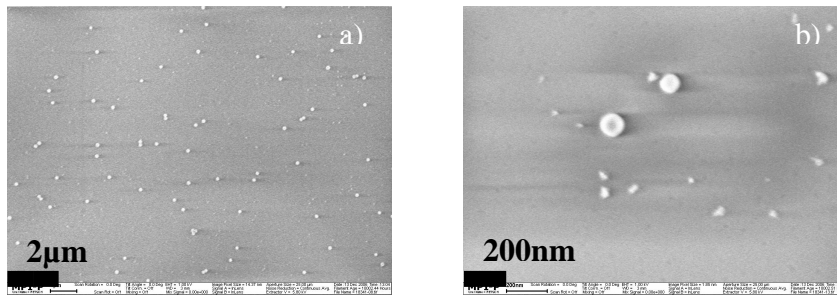


Fig.7.7 a) submonolayer mask made of polystyrene nanospheres that are electrostatically self-assembled on chemically treated glass substrate; b) the smaller is the nanospheres diameter the more problematic is the size monodispersity issue. Residual synthesis products are present in the nanoparticle suspension and attach to the substrate.

Fig.7.8 shows the 3D AFM image of a short- range ordered array of sub-wavelength holes in a thin gold layer (60 nm) that was fabricated with NSL method.

During the formation of the 2D submonolayer mask, several parameters are influencing the final distribution of particles such as: salt concentration and pH of the suspension solution, particles and surface charges, particles size and polydispersity, surface chemistry and the adsorption time.

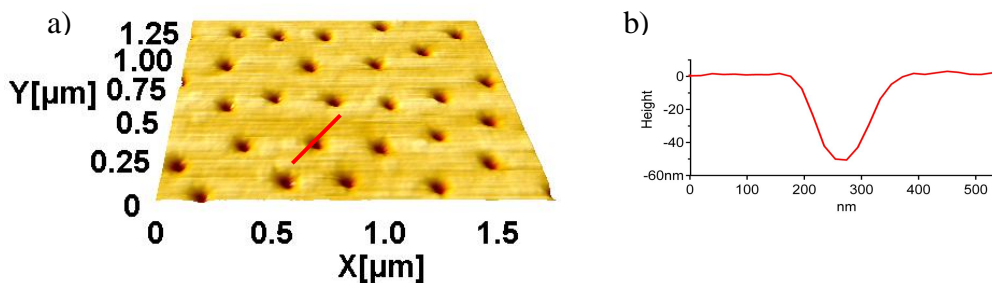


Fig.7.8 a) 3D-AFM image of a short-range ordered array of nanoholes perforated in a thin gold layer (60 nm thickness). The structures were obtained through NSL using polystyrene beads of 110nm diameter; b) cross line section of a single nanohole.

Homogenous distributions of individual nanoparticles on large areas were obtained with negatively charged (sulphate modified surface) polystyrene spheres that adsorbed electrostatically on oppositely charged surfaces (glass substrates that was previously functionalized with amino terminal groups). On clean, but chemically untreated hydrophilic glass substrates, the particle films aggregated often even at very low concentrations of the colloidal solution and it was difficult to control the distances between the adsorbed particles. By contrast, the Columbian interactions of the negative nano-beads with the positively charged glass substrates ensure a strong adhesion to the surface while the interparticle repulsion between already adsorbed beads prevent additional adsorptions within a characteristic distance. As a result, fairly well defined average distances between the particles on the surface are achieved.

Fig.7.9 shows AFM images of large areas of homogenous, high density (a) and low density (b) arrays of nanoholes in thin gold layers.

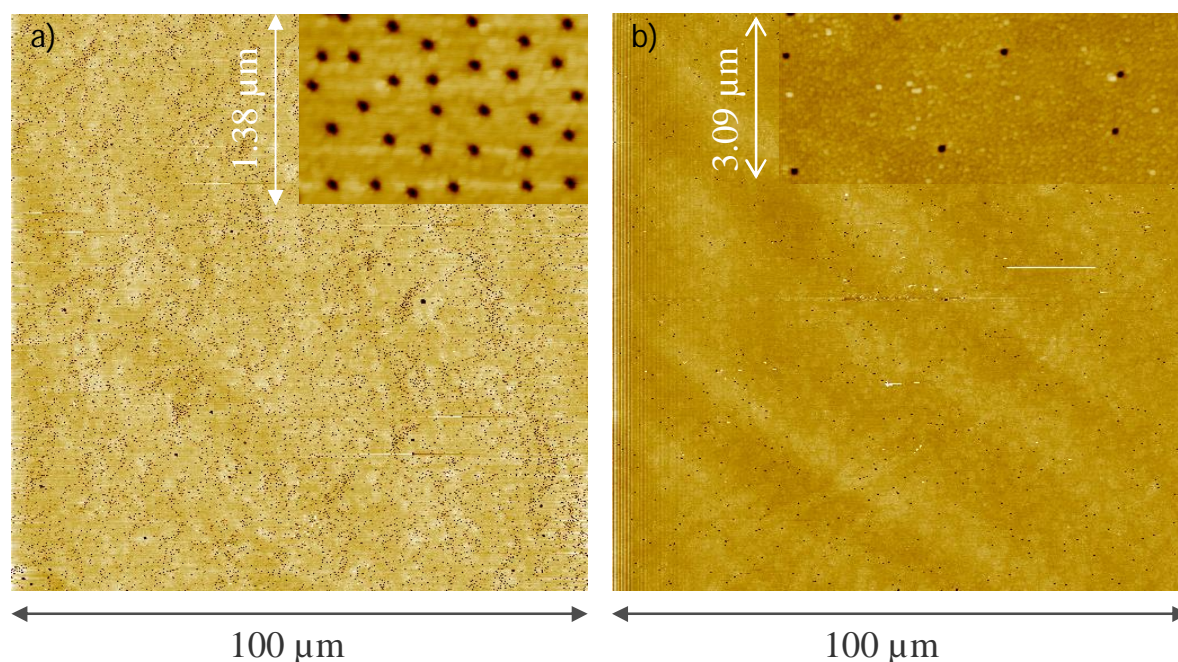


Fig.7.9 AFM images (in air, contact mode) of large areas (100μm-the largest area one can scan with AFM) of random arrays of nanoholes in thin gold layers at high density (12voids/μm²)- (a), and low density (0.33voids /μm²)- (b). The insets show detailed images of the gold layers (20nm thickness) with voids.

Shorter distances between the resulting nanoholes were achieved at increased salt concentration (up to 100mM NaCl) of the nanospheres suspension due to the screening of the interparticle repulsion during the mask deposition process. Dilute solutions of polystyrene nanoparticles were used in the concentration range 0.002-0.4% (v/v). The adsorption time varied between few minutes to about 30 minutes. For long incubation times and high concentrations of latex nanobeads in suspension, the resulting nanoholes are positioned at submicron distances from each other. When individual nanoholes need to be investigated (i.e. with single particle spectroscopy), convenient interspacing between the nano-voids has to be achieved. The example from Fig.7.9b represents a sample having an extremely low density of nanoholes (0.33voids /μm²). The features occupy in this case only 0.28% from the total surface area. This coverage is 21 times lower in comparison to 5.9% coverage with nanoholes estimated for the previous sample (12voids /μm²) shown in Fig.7.9a.

Size distribution of the fabricated nanoholes was estimated from grain analysis performed on AFM images (Fig.7.10). The statistics reveal in fact the size monodispersity of polystyrene beads used as templates. Although due to the tip broadening effects the dimensions are slightly overestimated, the distribution statistics of the nanoholes diameters is accurate.

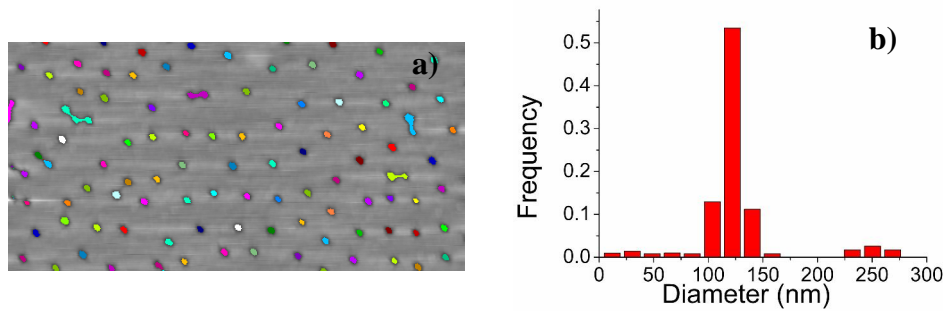


Fig.7.10 Size distribution (b) of the resulting nanoholes is obtained from the grain analysis of the sample's AFM image (a). For this particular sample NSL was performed with size monodispersed latex nanobeads of 110nm diameter.

NSL method based on electrostatic self-assembling of colloidal particles proves to be a versatile method for fabrication of large arrays of nanoholes in optically thin gold layers, with fairly controlled interspacing.

In DF microscopy, the nanoholes appear as bright coloured spots, due to their capability to support localized plasmon modes (Fig.7.11 and Fig.7.12).

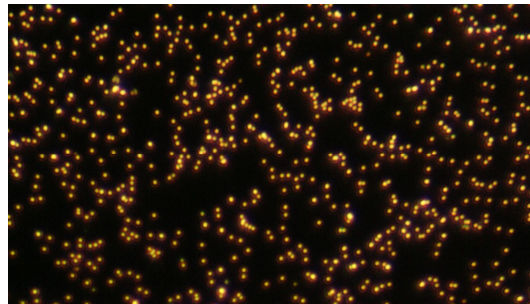


Fig.7.11 Dark-field microscopy image of nanoholes (100nm diameter) in an extended gold film (20nm thickness).

The optical properties of the nanoholes are dependent on their aspect ratio (defined as the ratio between the holes diameter D and the holes deepness h) as well as on their average interspacing. So far, no detailed electrodynamic calculations for holes in thin gold films exist. There is an overall similarity in the resonance behaviour between holes and disks³⁰. In a simple quasi-static approximation the holes are modelled as oblate spheroids and the resonance position can be estimated by minimizing the denominator of the resonant dipole polarizability $\alpha(\lambda)$ expressed in Eq.1.4. However, in contrast to nanodisks LSP, the nanoholes LSP have the possibility to interact through emission of surface plasmon polaritons (SPP) in the interceding gold film. At submicron separation the interhole coupling mediated by SPP excitation is expected to result in a pronounced renormalization of the LSP resonance. In Fig.7.12 different colours correspond to nanoholes of different aspect ratios and different surface number densities.

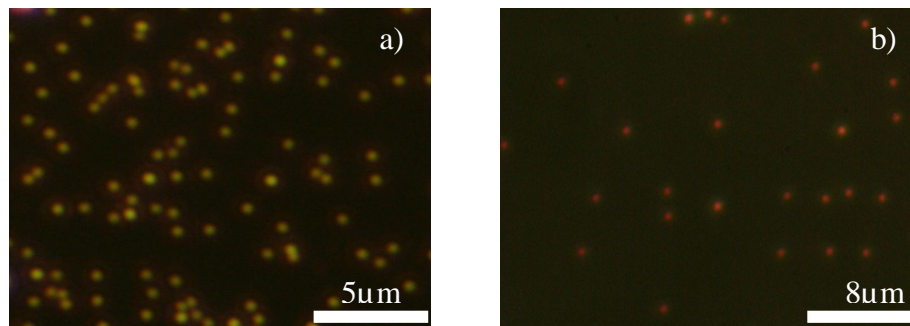


Fig. 7.12 The inter-holes coupling for dense hole arrays and the aspect ratio (defined as the ratio between the holes diameter D and the holes deepness h) of the nanoholes determine the spectral position of the localized surface plasmon resonance (LSPR). The aspect ratio of the nanoholes imaged here with DFM is 2.5 (a) and 4 (b).

7.4 Conclusions

I have employed nanosphere lithography for the construction of extended areas of regular arrays of triangle-shaped gold nanoparticles and of short-range ordered arrays of nanoholes in optically thin gold layers.

The specific achievements for the built systems are: i) individual, well separated features, ii) independent control of different structure parameters such as spacing, shape and size of the features, iii) suitable fabrication technique so that large areas are homogeneously nanostructured, and iv) reproducibility. To this end, the technical issues addressed were mainly related to the optimization of the mask deposition conditions such as the substrate and the solvent properties (salt concentration, the solvent evaporation rate), the particle charges, and the particle volume fraction in the colloidal solution.

I established that electrostatic self assembling of negatively charged polystyrene nanobeads on positively modified surfaces (with amino-terminal groups) ensures a homogenous distribution of particles on extended areas. AFM images prove the possibility to control the surface number density of the nanoholes and the interhole spacing, parameters that are decisive for LSPR sensing via spectroscopic measurements (to be performed either "in bulk" or on individual nanoholes).

Chapter 8

Lipid membrane coated gold nanorods as sensing elements

As an alternative to the nanostructured gold surfaces built in order to generate and exploit the LSPR sensing properties of the resulting nanostructures, gold nanoparticles can be used as sensing elements after their immobilization on glass surfaces. Gold nanorods exhibit longitudinal and transverse localized surface plasmon resonances which are basically independent on each other and can be selectively excited with polarized light. The longitudinal SPR component is extremely sensitive to changes in the dielectric properties of the local environment. In this work, plasmonic particles coated with lipid membranes are used as sensing elements for protein adsorption. Once the gold nanorods are “functionalized” with lipid membrane, the adsorption of proteins to the bilayer can be monitored via refractive index sensing properties of the plasmonic particles. The higher is the aspect ratio of the nanorods the greater is the sensitivity to interfacial changes in the refractive index. Specific or nonspecific adsorption of proteins to the lipid membrane which is coating the nanorods may be detected as resonance shifts in the scattering spectra. Since individual nanoparticles exhibit enhanced scattering behavior, single particle spectroscopy applied to gold nanorods is the most appealing method for detecting highly localized events, with increased sensitivity. The small detection area which is limited to only few hundreds of nanometers (the surface area of a single nanorod) renders this method potentially amenable for analysis of stochastic binding events as it is described in Section 1.4. Each single nanoparticle that is immobilized on the glass surface and coated with lipid membrane can be regarded as an individual plasmonic transducer of membrane mediated recognition events. One can further conceive the construction of a 2D array of such miniaturized sensor elements in combination with selective functionalization via ink-jet dispensing or microfluidics for achieving a high throughput sensing platform.

I present in the following the experimental approach and the proof of concept for the construction of an optical biosensor using gold nanorods as sensing elements for monitoring membrane mediated recognition events.

8.1 Self-assembling of gold nanorods on glass substrates

The optimal conditions for immobilization of gold nanoparticles at the desired surface number density have been investigated. To this end, glass substrates were subjected to two different treatments either to render them hydrophilic or to functionalize them with amine-terminal groups. The concentration of nanorods suspension, the time of incubation, pH and ionic strength were adjusted in order to control the deposition and distribution of the plasmonic particles on the surface.

8.1.1 Immobilization of gold nanoparticles on amine-functionalized glass

Fig. 8.1 shows how the concentration of nanorods in the incubation volume influences the surface number density of the adsorbed particles. Various dilutions in Milli-Q water were prepared from the same original stock suspension of nanorods (initial concentration estimated to 10^{10} nanoparticles/ml). Except for the nanorods dilutions, all samples were prepared under identical conditions on amine-functionalized surfaces with EDSPA, as described in the section 3.2.2.

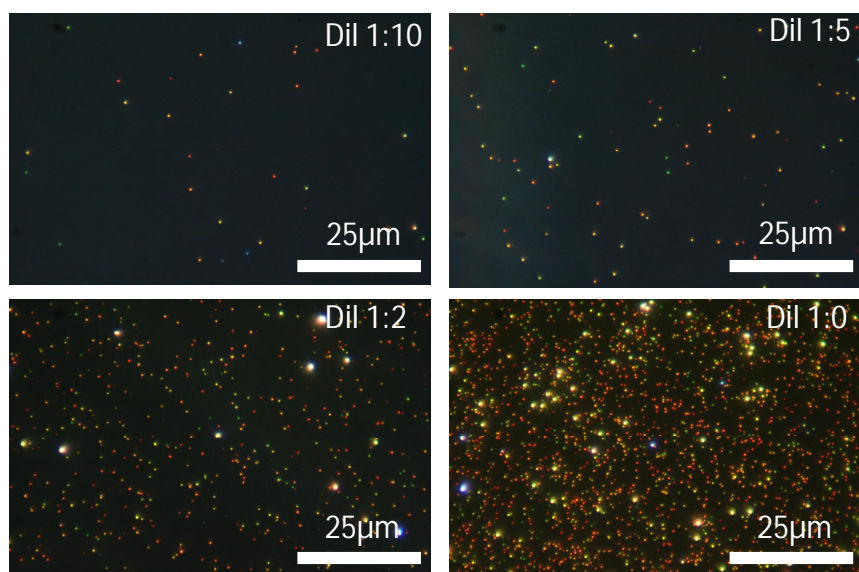


Fig. 8.1 DFM images of self-assembled gold nanorods on amine-functionalized glass surfaces. The samples were incubated over the night with different dilutions (1:10, 1:5, 1:2 and 1:0) from the same batch of nanoparticles (initial concentration 10^{10} nanoparticles/ml) under identical conditions. Different colors correspond to gold particles of different aspect ratios. Accidentally, at higher surface coverage some nanorods may aggregate and appear as bright yellow/orange spots.

As expected, the surface number density of gold nanorods increases with increasing concentration of nanoparticles in solution.

Particle analysis of DFM images was performed using the public-domain image analysis software (Image J, NIH) for estimation of surface number densities.

Dilution	Surface No. Density/ mm ⁻²
1:0	832 x10 ³
1:2	85 x10 ³
1:5	18 x10 ³
1:10	11 x10 ³

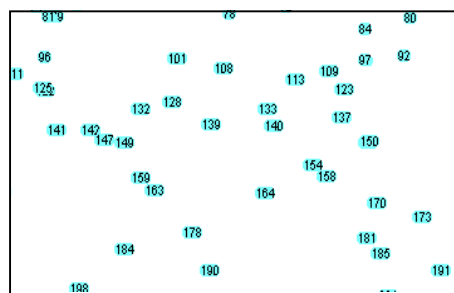


Fig.8.2 a) Surface number densities corresponding to various dilutions of gold nanorods in the incubation volume; b) Sequence of a DF image analyzed with Image J software for particles counting.

8.1.1.1 Influence of CTAB on the particles' adsorption efficiency

Decreased adsorption efficiency (lower surface number densities) of gold nanorods on the substrate was observed when the cationic surfactant CTAB, used as stabilizing agent in the process of nanorods synthesis, was present in excess in the incubation volume. When CTAB containing nanorods suspensions were simply diluted with Milli-Q water, there was a need for long incubation times (several hours, or even overnight incubations) in order to reach sufficiently high surface number densities. At small dilution factors, not only the nanorods concentration but also the CTAB concentration remains high and hampers or slow down the process of particles deposition. Following the immobilization of nanorods on the glass surfaces, the samples were thoroughly washed with Milli-Q water.

8.1.1.2 Incubation time

In order to remove the excess of CTAB before their self-assembling on the glass substrates the nanoparticles were washed by consecutive centrifugation steps (each time 5min at 6000 rpm). The use of washed nanorods may however favor the formation of aggregates in solution or on the surface. Clustering of washed nanoparticles is mostly facilitated by long incubation times (longer than several minutes) and/or by increased salt concentrations (Fig.8.3)

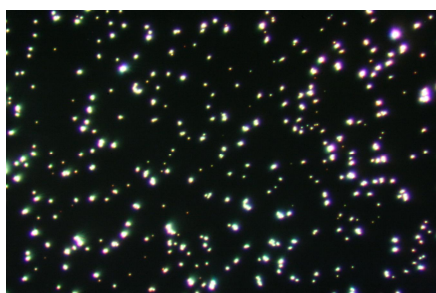


Fig.8.3 DFM image of nanoparticle aggregates formed on the glass surface after long incubation time (longer than 10 min) at high NaCl concentration (100mM) of the aqueous suspension of nanorods. The large aggregates scatter strongly the light and do not exhibit a spectral characteristic.

8.1.1.3 Effect of pH

Low pH values of the incubation solution induces the protonation of the amine terminal groups of the EDSPA functionalized glass surfaces and influence the adsorption of the gold nanoparticles. Fig. 8.4A shows an example where, during the incubation with a suspension in water of washed nanorods, the local pH was decreased very much on a small area of the substrate by dropping a small amount of hydrochloric acid (30%) with a very thin pipette whose end tip was placed close to the surface. The surface number density of nanorods increased considerably in the area where the pH was lowered. The higher the concentration of the HCl droplet, the higher was the corresponding surface number density of the nanorods. This demonstrates clearly that one can tune the surface number density of nanorods by adjusting the pH of the incubation solution.

The gold particles remained irreversibly adsorbed on the functionalized glass surface. Thorough washing of the samples with Milli-Q water did not remove the particles and did not lower the surface coverage of the areas that were exposed to low pH during the incubation with the colloidal suspension.

Homogenous coverage with gold nanorods at high surface number density was obtained all over the sample surface by lowering the pH in the entire incubation volume of the colloidal suspension (Fig.8.4B).

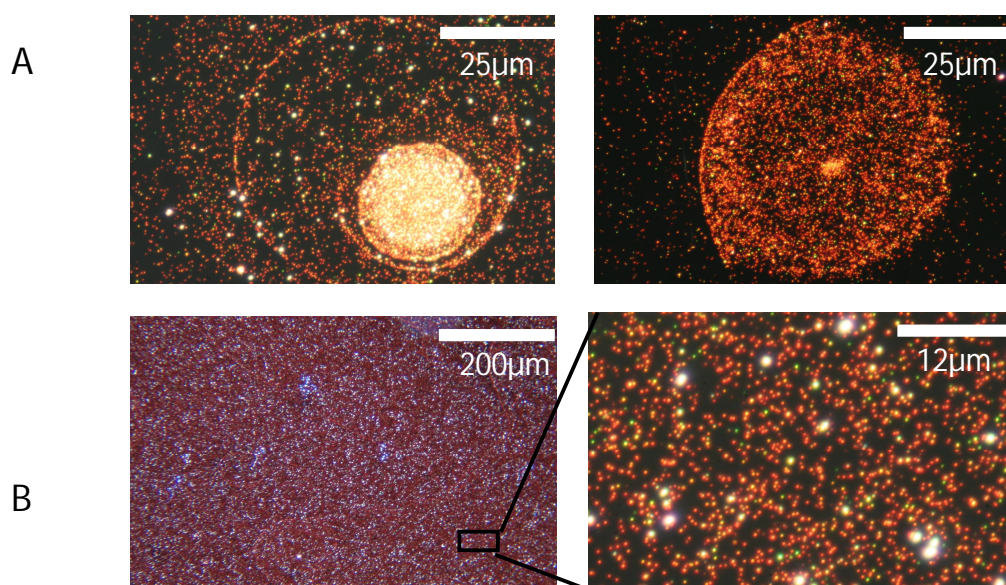


Fig.8.4 DFM images of self assembled nanorods on amine-functionalized glass substrates: A) the surface number density of nanorods is considerably increased in the area where the pH was locally lowered. The lower is the value of the local pH (left compared to the right picture) the higher is the surface coverage with gold nanorods; B) Global (left) and detailed (right) view of a homogeneous distribution of gold nanorods self assembled on EDSPA functionalized glass, at low pH. The average surface number density was estimated to $1.2 \times 10^6 \text{ mm}^{-2}$.

8.1.2 Self-assembling of gold nanorods on hydrophilic glass surface

The adsorption of gold nanoparticles on hydrophilic glass surfaces is facilitated when the ionic strength of the colloidal solution is increased by adding NaCl up to 100mM final concentration. This method of nanoparticle adsorption via short range Van der Waals interactions is unspecific with respect to the nature of the adsorbed objects. Moreover, employing similar concentrations (10^9 - 10^{10} nanoparticles/ml) of aqueous suspensions of gold nanorods, the surface coverage of the hydrophilic substrates was generally lower than the coverage obtained on amine-functionalized substrates. Only one control parameter could be adjusted in the first case for modifying the surface coverage, namely the concentration of nanoparticles in suspension. Short incubation times (up to 5 minutes) are required to prevent the formation of particles aggregates.

With this method one can obtain samples with well separated and evenly distributed particles, suitable for investigations with single-particle spectroscopy.

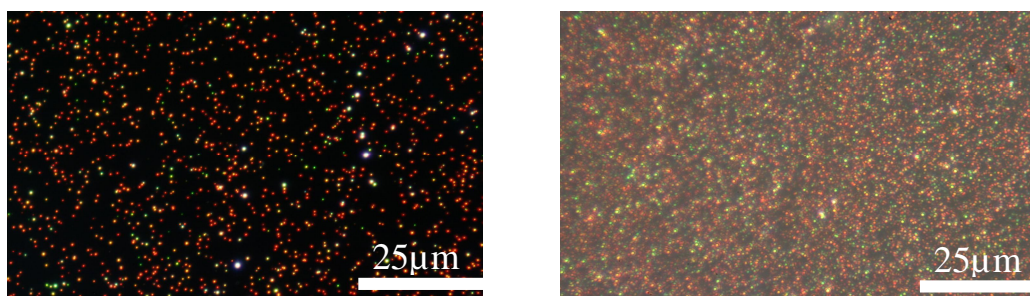


Fig.8.5 DF images of self-assembled gold nanorods on hydrophilic glass substrates show that the surface coverage is considerably increased on the sample prepared with mPEG-NH₂ conjugated nanorods (right) as compare to the sample prepared, under similar conditions, with washed nanorods (left).

Another way to increase the surface number density of gold nanorods on the hydrophilic glass substrate is to functionally modify the particles' surface. mPEG-NH₂ conjugated nanorods, for instance, formed dense submonolayers that were stable to consecutive washing procedures. Fig.8.5 shows, for comparison, DF images of samples prepared either with bare washed nanorods or with amino PEGylated nanorods that were self assembled on hydrophilic glass substrate under similar conditions, from suspensions of similar particle concentrations (10^9 nanoparticles/ml). The amino functional groups on the mPEG-NH₂ conjugated nanorods surface render them positively charged by protonation in the water suspension and facilitate the electrostatic adsorption on the glass surfaces which are slightly negatively charged.

Functionalization of the nanoparticles in solution obviates the problem of rapid formation of aggregates and also offers additional possibilities for controlling the surface coverage besides the empirical adjustment of the colloidal concentration. However, since the evanescent field around the gold nanorods is exponentially decaying with the distance from their surface, the sensitivity with respect to the local changes in the refractive index of the surroundings decreases rapidly with any intermediate functionalization layer that places the interacting sites of interest further away from the

particle' surface. Therefore, only bare gold nanorods were coated with lipid membranes for plasmonic sensing of the protein adsorption, as shown in the following sections.

8.2 Lipid bilayer formation on glass substrates with gold nanorods

Following the biosensor concept for spectral detection of proteins interacting with lipid membranes, gold nanorods immobilized on the glass substrates were coated with lipid bilayers. The successful reconstitution of lipid membranes, their continuity and integrity was probed under different experimental conditions with complementary techniques such as fluorescence microscopy and FRAP, AFM and dark field scattering spectroscopy. Individually addressable micropatterned lipid bilayers were formed on the glass substrates with gold nanorods by spreading LUVs containing a small fraction (1mol% or less) of fluorescently labeled lipids (either sulforhodamine DHPE or β -Bodipy C₁₂-HPC), through the capillaries formed by conformal contact between PDMS molds and the substrate (see Section 3.5 for complete description of the method). Under the illumination with white light directed through the dark field condenser of a DF microscope it was possible to visualize simultaneously the scattering signal of the nanorods overlapped with the fluorescence signal of the microstructured lipid membranes (Fig.8.6).

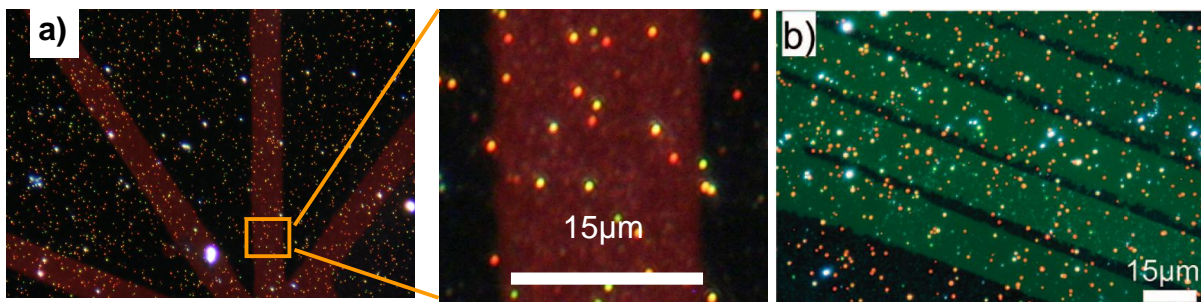


Fig.8.6 DFM images (true colors) of the fluorescently labeled lipid membranes (POPC/POPS 4:1) that were microstructured on glass substrates with gold nanorods. Prior immobilization of the nanoparticles, the glass surfaces underwent different treatments: a) the glass surface was functionalized with amine-terminal groups (EDSPA), the lipid membrane is labeled with sulforhodamine DHPE (1mol%, red fluorescence) b) the glass surface is hydrophilic, the lipid membrane is labeled (with β -Bodipy C₁₂-HPC (0.2 mol%, green fluorescence).

The lipid membranes were spread either on hydrophilic glass substrates or on glass substrates that were previously functionalized with amine-terminal groups (EDSPA). Before membrane formation, the gold nanorods were immobilized on the substrates at a low surface number density. Adhesion and rupture of the lipid vesicles on solid supports

are processes that are governed by the interaction between the lipid vesicles and the substrate, the interaction between the adsorbed vesicles, and the interactions within the adsorbed vesicles. Electrostatic forces contribute to these three interactions. Therefore, on amine functionalized glass surfaces negatively charged vesicles (POPC/POPS 4:1) were spread in order to increase the vesicles adhesion to the substrate and facilitate their deformation and rupture. On the hydrophilic glass substrates the bilayers were spread equally from either pure POPC or from mixtures of POPC/POPS (4:1) vesicles. In the latter case, the calcium concentration of the vesicles suspension was increased to 2mM since it is known the ability of these bivalent ions to “bridge” negatively charged entities such as the carboxilate groups of POPS to the negative charges on the glass surface.

Influence of high surface density of gold nanorods

Large defect areas are observed for the lipid membranes spread on glass surfaces exhibiting high coverage with gold nanorods. This phenomenon is visible on both, hydrophilic and amine functionalized glass surfaces and is shown in Fig.8.7.

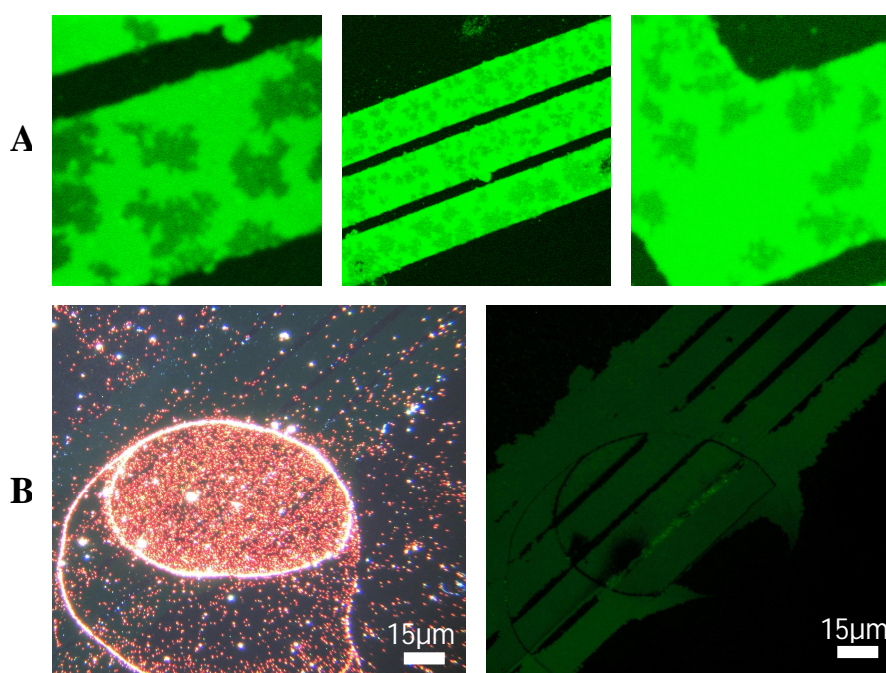


Fig.8.7 A) Fluorescence images of the lipid membranes (POPC/POPS 4:1) that were micropatterned on hydrophilic glass surfaces having high surface number densities of gold nanorods. Several defects (darker areas) are observable. From the left to the right, the size of the images (in μm) are: 24x24, 96x96, 24x24; B) DF image (left) and fluorescence image (right) taken from the same area of a sample consisting in microstructured lipid membrane (POPC/POPS 4:1) on amine functionalized glass substrate with a heterogeneous distribution of gold nanorods. One can observe the correspondence of the regions exhibiting high surface number densities of gold nanoparticles with the regions that are depleted of lipid membrane.

Heterogeneous coverage with gold nanorods was achieved on amine functionalized glass surfaces by locally lowering the pH, as described in section 8.1.1.3. On these substrates, fluorescently labeled membranes were micropatterned. To distinctly visualize the surface distribution of the nanorods and the lipid membranes, two separate images focused on the same area of the sample were taken in DF and fluorescence microscopy (Fig.8.7B). Comparing both images one can clearly notice the correspondence of the regions that are depleted of lipid membrane with the regions exhibiting high surface density of gold nanoparticles.

These observations are in agreement with theoretical calculations of Svein and Andelman that estimate minimal adhesion energy of the lipid membrane at maximum substrate roughness^{102, 103}. At lower adhesion, the lipid vesicles may not have sufficient energy to adsorb and fuse with the substrate such that several membrane defects or/and membrane depleted areas are visible.

8.2.1 FRAP analysis

To investigate the lateral mobility of lipids that is commonly regarded as a criterion for the successful reconstitution of lipid membranes on solid supports, fluorescence recovery after photobleaching (FRAP) experiments were performed on the lipid bilayers formed by vesicle fusion on glass substrates with gold nanorods. The membranes (POPC or 4:1 POPC/POPS mixtures) were spread on both, hydrophilic and amine functionalized glass surfaces. They were either spread over the entire surface or microstructured by soft lithography (micromolding in capillaries). In all cases, the surface number density of gold nanoparticles was lower than $1.2 \mu\text{m}^{-2}$ in order to avoid the formation of disconnected lipid phases (as it was previously shown in Fig.8.7).

The FRAP method, technical measuring conditions and data analysis are described in Section 3.4.

Fig.8.8 shows, for exemplification, the recovery curve of the fluorescence intensity inside of a bleached spot of Gaussian shape; the inset contains the fluorescence images (at 0s, 5.4s, 11s and 20s after photobleaching) from a series taken during FRAP experiments on POPC membranes microstructured on hydrophilic glass substrates with gold nanorods. The measured diffusion coefficients of the lipids are in the range of $3.9\text{-}5.1 \mu\text{m}^2/\text{s}$. No correlation of these values with the surface number density of gold nanoparticles underlying the lipid bilayer was observed. The same diffusion coefficients were obtained for lipid membranes spread on glass substrates without nanorods (control experiments). These values are in agreement with earlier reports^{104, 105}.

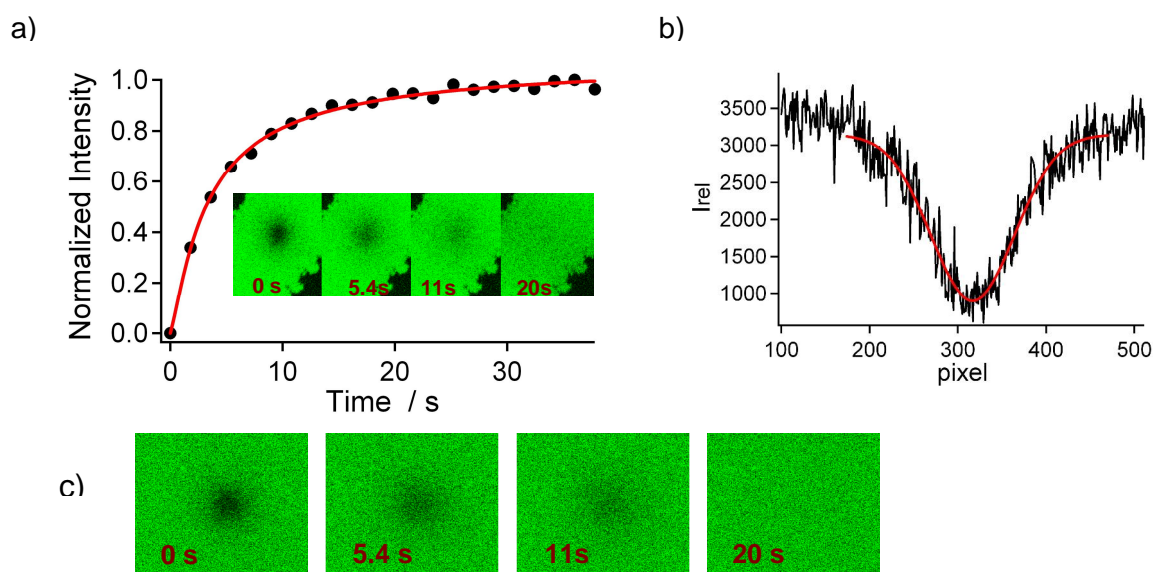


Fig.8.8 a) Recovery curve of the fluorescence intensity inside of the bleached spot on a lipid bilayer (labeled with β -Bodipy C_{12} -HPC) microstructured on glass substrate with gold nanorods. The inset represents fluorescence images from a series taken during the recovery of the fluorescence in the photobleached area (0s, 6.4s, 10s and 20s after photobleaching); b) the intensity profile of Gaussian shape ($4\mu\text{m}$ radius) of the bleached spot; c) FRAP performed on extended lipid bilayers supported by glass with gold nanorods. Fluorescence images are from a series recorded during fluorescence recovery at different times after photobleaching. The size of each image is $25 \times 25 \mu\text{m}^2$. The diffusion coefficient is on average $0.6 \mu\text{m}^2/\text{s}$ higher than that measured for microstructured bilayers in similar conditions.

A slight increase in the diffusion coefficients of lipids ($0.6 \mu\text{m}^2/\text{s}$ average increase) was measured when FRAP was performed on fully extended membranes as compared to microstructured bilayers. The faster recovery of fluorescence on extended membranes is the result of spatially unrestricted diffusion of fluorophores from all directions of the planar surroundings of the bleached spot. For microstructured bilayers, this diffusion is partially constrained to the geometry of the membrane pattern. The fraction of mobile lipids was not affected by the presence of the underlying gold nanoparticles and remained close to 100%. Similar values of the diffusion coefficients and no significant immobile fraction of lipids were found under similar conditions for lipid membranes that were spread on amine functionalized glass surfaces with gold nanorods (Table 8.1).

Substrate	SND (mm^{-2})	D ($\mu\text{m}^2/\text{s}$)
SiO_2	0	4.61 ± 1.4
SiO_2	645×10^3	5.18 ± 1.3
SiO_2	732×10^3	3.9 ± 1.6
NH_2	0	5.21 ± 1.3
NH_2	438×10^3	5.77 ± 1.9
NH_2	879×10^3	4.82 ± 1.2

Table 8.1 Diffusion coefficients at room temperature of β -Bodipy C_{12} HPC in lipid membranes (POPC/POPS 4:1) that were microstructured on glass substrates with gold nanorods at different surface number densities (SND). The substrates were either clean hydrophilic glass or NH_2 -functionalized glass. Each value is the average of three independent measurements.

FRAP experiments do, however, not reveal directly the detailed configuration of the lipid membrane interacting with the gold nanoparticles immobilized on the glass substrate. The nanorods can be regarded either as ellipsoidal objects that are coated with lipid membrane or as fixed obstacles imbedded in the lipid membrane. If the membrane is draping the nanorods, the independency of the experimentally measured diffusion coefficients on the presence of the nanoparticles is mainly due to undetectable effects induced by low area fractions of the underlying nanorods on the long range translational mobility of lipids.

If the gold nanoparticles are regarded as obstacles imbedded in the lipid bilayer, one can deduce, on the analogy of the integral proteins that are known to lower the diffusion coefficients of the lipids, that the effective size of the obstacles is larger than the size of the nanorods. This is because a favorable interaction of the particles with the surrounding acyl chains impedes the mobility of the closely located lateral lipids. If contrarily, the nanorods repel the surrounding acyl chains, a restricted free lipid area would be created around each particle and this area should increase until the line tension of the membrane defect is minimized.

Computer simulations of FRAP experiments on lipid membranes¹⁰⁶ revealed a linear dependency of the diffusion coefficients with the area fraction ξ of the obstacles up to $\xi=0.5$ when the percolation threshold, defined as the obstacle area fraction at which the fluid phase becomes disconnected, is reached. This situation is experimentally achieved and presented in Fig.8.7.

8.2.2 Imaging with AFM

While epifluorescence microscopy allows only for a global characterization of the supported lipid bilayers draped over the nanorods on glass substrates, AFM permits a detailed analysis on the nanometer scale of the sample topography.

AFM imaging of gold nanoparticles in a small scanning area supposes a conveniently high surface number density of nanorods that are interacting strong enough with the substrate to withstand subsequent washing steps without causing their detachment from the surface. This was obtained, as previously described, by immobilizing gold nanoparticles on amino functionalized glass substrates. Following the nanoparticles immobilization step, the sample was washed thoroughly with Milli-Q water and dried under the nitrogen stream. On this substrate the suspension of large unilamellar vesicles of POPC/POPS 4:1 lipid composition was incubated for about 20 minutes to form the supported lipid membrane. The excess of vesicles that did not adhere to the surface was rinsed away and the sample was imaged in contact mode (Fig.8.9). Imaging was performed with Nanowizard II BioAFM (JPK Instruments, Berlin) using Veeco MLCT-C cantilevers with a nominal spring constant of 0.01N/m.

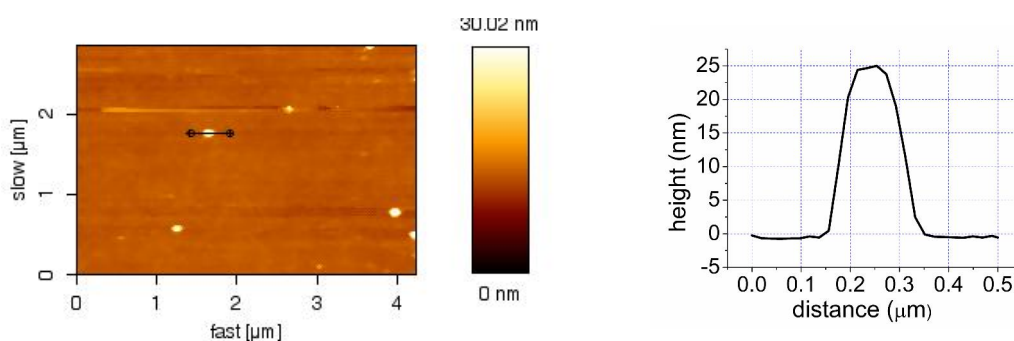


Fig.8.9 a) CM-AFM image in liquid of lipid membrane (POPC/POPS 4:1) spread on the glass substrate with gold nanorods. The glass substrate was previously functionalized with amine terminal groups. b) Line cross section of the nanoparticle draped with lipid membrane

For lipid membranes spread on a hydrophilic glass surface to which the gold nanorods are only weakly attached, TM-AFM was preferred since in CM-AFM the lateral forces are high enough to alter the sample, change the position or even remove the particles from the surface.

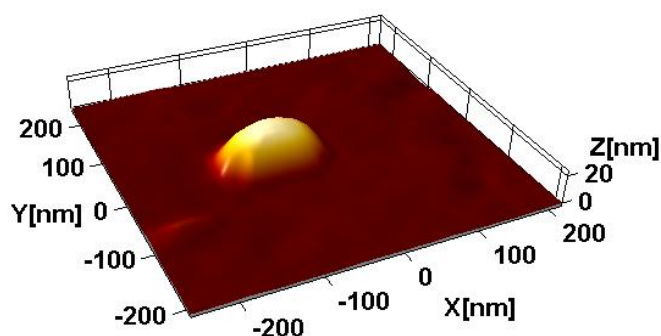


Fig.8.10 TM-AFM image in liquid of a lipid membrane coated gold nanorod previously immobilized on hydrophilic glass surface. The lipid membrane composition is 95%POPC, 5%biotin.

TM-AFM imaging was performed with Dimension 3100 Nanoscope III (Veeco, Santa Barbara), using Olympus OMCL-TR400PSA cantilevers (34KHz res. frequency in air and 7.4KHz in liquid). Height information is correct and in agreement with the mean value of the nanorods diameter measured with TEM. Because of the tip convolution effects the lateral dimensions of the particle are overestimated.

No defects around the nanorods can be observed, leading to the hypotheses that the membrane is either coating the particle or, if the particle is embedded into the membrane, the acyl chains of the surrounding lipids are closely following the nanoparticle contour. To probe the continuity of the lipid membrane, phase imaging with AFM is further (in Chap. 10) employed such that, based on tip-sample interaction, one can differentiate the nature of the scanned substrate (gold or SLB).

8.3 Sensing the lipid membrane with single particle spectroscopy

Based on the refractive index sensing properties of gold nanoparticles one can efficiently employ single particle spectroscopy to probe the continuity of the lipid membrane draped over the nanorods immobilized on the glass substrate. The change in the dielectric properties of the immediate neighborhood resulting from coating the plasmonic particle with lipid bilayer is perceived in the scattering spectra as a red-shift of the long axis plasmon resonance. An example of individual scattering spectra recorded before and after coating the same nanorod with lipid membrane is represented in Fig. 8.16. The long-axis surface plasmon resonance peak shifted obviously with 6.38nm, from 646.28nm to 652.66nm.

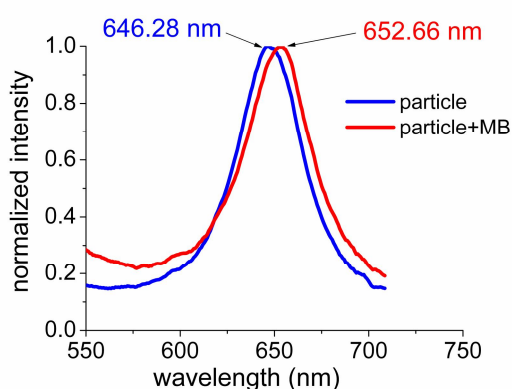


Fig. 8.16 Individual scattering spectra of the same gold nanorod previously immobilized on the glass substrate, before (blue line) and after (red line) coating with lipid bilayer (94%POPC; 5% biotin-DHPE, 1% β -Bodipy C_{12} -HPC). Spectral shift of the longitudinal surface plasmon resonance peak is 6.38 nm.

The spectral shift due to the coating with lipid membrane of a nanorod having 56nm/26nm along the long/short axes (the same dimensions as the mean size values of the nanorods used in the spectral measurements) was theoretically estimated at 7.40nm in the electrostatic approximation considering the minimization of the denominator of polarizability (longitudinal component) for a coated prolate ellipsoid ²⁷:

$$\alpha = v \frac{(\epsilon_c - \epsilon_m)[\epsilon_c + (\epsilon - \epsilon_c)(L - fL_c)] + f\epsilon_c(\epsilon - \epsilon_c)}{[\epsilon_c + (\epsilon - \epsilon_c)(L - fL_c)][\epsilon_m + (\epsilon_c - \epsilon_m)L_c] + fL_c\epsilon_c(\epsilon - \epsilon_c)} \quad (8.1)$$

Here, v is the gold particle's volume, f is the fraction of the total particle volume corresponding to the lipid shell, L and L_c are the depolarization factors of the uncoated and coated ellipsoids, while ϵ , ϵ_c and ϵ_m are, respectively, the dielectric functions of

the gold particle, of the lipid shell and of the surrounding medium (aqueous buffer). In this calculation, the nanorod was considered to be fully wrapped with a lipid bilayer of 5nm thickness while the influence of the glass substrate which is in contact with the coated nanorod was taken into account by introducing ϵ_m as an averaged dielectric function of the glass (2.25) and of the aqueous solution (1.76)²⁷. The calculation is expected to be, however, an overestimation of the real spectral shift. This is because the lipid membrane is draping the nanoparticle, coating it only partially. Simple electrostatic approximation based calculus may not count accurately for the complexity of the actual local dielectric interface of the nanorod. Moreover, the degree of coating the particle with lipid membrane is dependent on the capacity of the bilayer (elastic properties) to follow the nanoparticle contour as well as on its adhesive properties with respect to the substrate.

The morphology and the size of nanoparticles resulted from the same preparation and used for spectroscopic measurements can be observed and statistically characterized with TEM. Key structural parameters such as the aspect ratio, the cap-end shape and the volume are seen to vary from particle to particle. These variations determine, in the spectroscopic measurements, the inhomogeneity of the optical response with respect to the local changes in the dielectric interface of the plasmonic particles. In consequence, one can not perform a precise quantitative comparison between the calculated scattering spectra and the experimental spectra of one single nanoparticle selected on the sample.

Simultaneous detection of individual scattering spectra of several particles on the same sample was possible due to the replacement of the entrance slit of the spectrometer by an LCD (electronically addressable liquid crystal device) in the spectroscopic setup (see Section 2.5). Therefore, membrane coated and uncoated nanorods previously immobilized on the glass substrate were analyzed with respect to the wavelength of their long-axis SPR (λ_{res}). The lipid bilayer was fluorescently labeled and microstructured on the glass substrate with gold nanorods such that one could visually, select, and differentiate the particles from uncovered and membrane covered areas (see Fig.8.6 as an example). The probability distributions of the resonance wavelengths corresponding to two distinct populations namely naked and lipid membrane coated nanorods that were selected on the same sample are shown in Fig.8.17, for two samples ("a" and "b") that were prepared under identical conditions but using nanorods resulted from different stock solutions (stock A and stock B respectively).

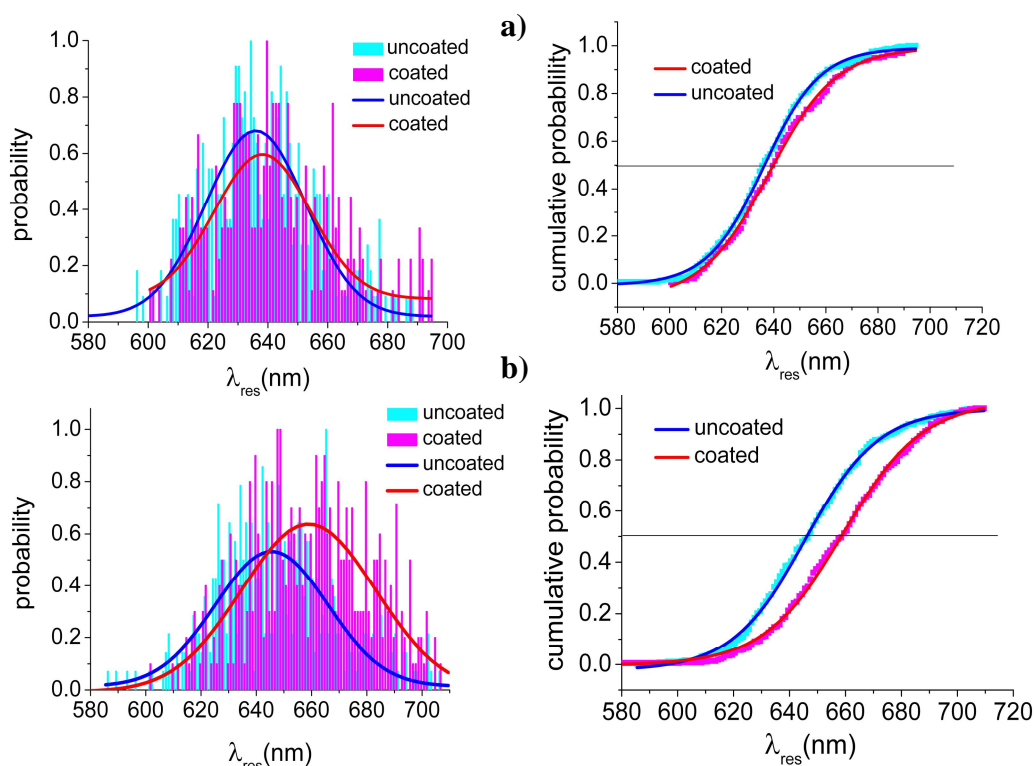


Fig.8.17 Probability distributions and cumulative probabilities of two λ_{res} data sets corresponding to uncoated and membrane coated particles on the sample "a" (a) and on the sample "b" (b). The samples were prepared with nanorods resulted from two different stocks, stock A and stock B respectively. Numerical values provided by the statistical analysis are presented in Table 8.2.

Table 8.2: Statistics of two λ_{res} data sets (coated/uncoated particles) for sample "a" and for sample "b"

	sample "a"		sample "b"	
spectral shift (nm)	4.46		10.56	
	uncoated	coated	uncoated	Coated
λ_{res} mean value (nm)	637.59	642.06	647.60	658.17
SD (nm)	19.13	20.02	21.51	23.18
sample size	255	333	392	373

For sample "a", the measured resonance wavelengths exhibit normal distributions with mean values of 637.59nm and 642.06nm corresponding, respectively, to uncoated nanorods and membrane coated nanorods. These two populations are statistically different at $p=0.01$ level of significance according to Welch's unpaired t test. Since λ_{res} values are highly dependent on the geometry of the plasmonic particles, standard deviations of both λ_{res} data sets (SD=20.02nm for coated and SD=19.13nm for uncoated rods) reflect the size and shape polydispersity of the employed nanoparticles.

A statistically significant difference at 0.001 level was also established between λ_{res} data sets measured for coated and uncoated particles on sample "b". Although for the sample "b", the normality test (Shapiro-Wilk) did not find a normal distribution of λ_{res} data measured for coated nanorods, since the sample size is large enough, ($N_c \gg 100$), in agreement with the central limit theorem, one can consider that the sample mean follows the normal distribution even if the respective variable is not normally distributed in the population. Therefore a parametric method i.e. Welch's unpaired t test may be sufficient to decide whether there is a significant difference, with regard to λ_{res} values, between the group of particles selected from the membrane coated areas and the group of uncoated particles. The larger λ_{res} mean value (647.60nm) of uncoated particles as well as the larger spectral shift (10.56nm) of membrane coated particles lead to the conclusion that the nanorods from stock B are characterized, statistically, by a higher aspect ratio. Although the sensitivity of these nanorods with respect to interfacial changes in the refractive index is higher, the λ_{res} values of coated particles are loosely distributed around the mean value (658.17nm) and they hardly follow a normal distribution. This considerable increase of data scattering for particles selected from the membrane coated areas of the sample "b" has the origin in the higher size polydispersity of the employed nanorods which may have different resonance wavelength in buffer and may exhibit different spectral shifts when coated with membrane or, may simply show no spectral shift if, due to an unfavorable geometry, the lipid membrane fails to coat the particle. The influence of nanorods geometry on their interaction with the lipid membrane is investigated in the following section.

8.4 Configurational limitations of membrane-nanoparticle interaction

Highly curved lipid membranes are found in many functionally distinct regions of the cellular plasma membrane such as caveolae, clathrin-coated pits, microvilli, endocytic and secretory vesicles, the internal membranes of endosomes, and parts of the endoplasmic reticulum and Golgi apparatus. During the membrane trafficking, the curvature of the membranes changes by tubulation, budding, fission or fusion. The capacity of biological membranes to adopt various configurations is easily reproducible in experimental studies employing model membranes such as small or giant lipid vesicles, solid supported or pore suspended lipid bilayers. The extent to that the lipid membrane can faithfully follow a certain nanometer scaled profile on solid supports is however a complex matter of debate and experimental investigation in the relatively recent literature. While some studies do claim that irregularities in the silica surface may prevent lipid bilayer spreading¹⁰⁷⁻¹⁰⁹, it was demonstrated by cryoelectron microscopy that silica beads with diameters of 110 nm can be entirely coated with continuous lipid bilayers⁵. Real time deformations of wrinkled elastomers used as substrates revealed the membrane compliancy with the underlying topography when the constituent lipids are in the fluid (POPC) and, more remarkably, in the gel (DPPC) phase¹¹⁰. A quantitative understanding of the degree of wetting sub-micrometer features of the underlying substrate is generally advanced in experimental approaches in terms of a simplified balance between adhesion and bending energies of the lipid membranes^{14, 111, 112}. Pure theoretical studies have

shown that compared to a planar, homogenous surface, the sinusoidal surfaces, trenches and pits act to reduce the membrane adhesion energy ¹⁰². For a spherical colloidal particle interacting with a fluid membrane, comprehensive numerical calculations of the structural wrapping phase diagram points to the influence of the particle size on the wrapping behavior in relation to the adhesion energy and elastic properties of the lipid membrane ¹¹³. Larger particles (>10nm) appear to be easier engulfed by the lipid membrane.

In the present work, nanorods resulted from different stock solutions were employed such that the size, the aspect ratio and even the shape of the particles were different from sample to sample. As described previously, the nanorods were immobilized on hydrophilic glass surfaces and on this substrates fluorescently labeled POPC lipid membranes were spread by vesicle fusion. For samples that were prepared with nanorods characterized by increased size and shape polydispersity or with nanorods in a backbone shape (see Fig.3.6a), fluorescence microscopy revealed numerous pore-like defects in the lipid membrane. The location of these defects coincides with the location of the gold particles as shown in the example from Fig.8.18 that correlates the DF and fluorescent images of the same sample area. The dark spots in the fluorescence image indicate defects in the lipid membrane while the bright spots of the DF image localize, via scattering signal, the plasmonic particles. To better visualize the corresponding positions, the same mask (consisting of blue and yellow ellipses) was overlapped on both pictures. Only few particles (identified with blue ellipses) appear to be coated with membrane while most of the nanorods (identified with yellow ellipses) seem to induce local structural defects in the lipid bilayer.

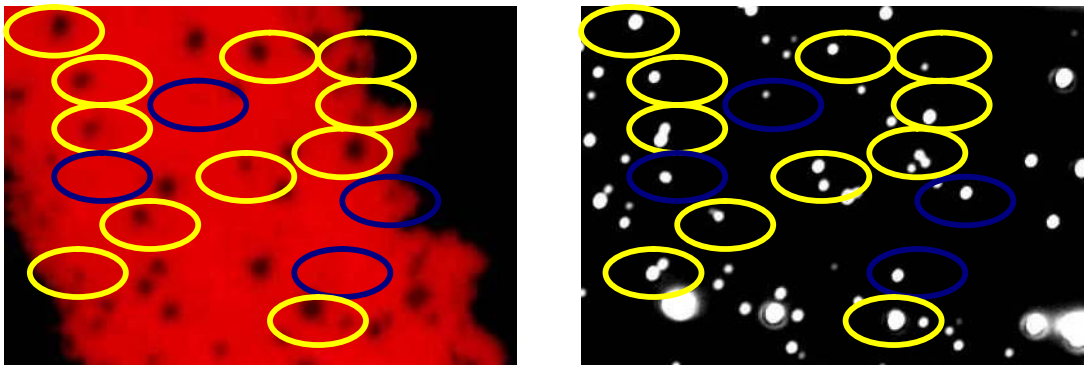


Fig.8.18 Fluorescence image (left) and DF image (right) of the same area of a lipid membrane microstructured over the glass substrate with gold nanorods. The dark spots in the fluorescence image indicate defects in the lipid membrane while the bright spots of the DF image localize, via scattering signal, the plasmonic particles. The same mask (consisting of blue and yellow ellipses) is overlapped on both images to allow a better visualization of the corresponding positions. The particles that appear to be coated with membrane are identified with blue ellipses while uncoated particles are identified with yellow ellipses. The nanorods used for this sample are polydispersed in size and shape, with a preponderant backbone configuration.

Once a local breakage is induced in the lipid membrane upon the interaction with the gold particle, the bilayer tends to reorganize in order to minimize its configurational energy that includes now the line tension (γ_L) arising from the defect edges¹¹⁴. A pore of radius R formed in a planar membrane has the energy $F_{\text{pore}}=2\pi R\gamma_L - \pi R^2\gamma$ and the radius R will increase until the lateral tension in the membrane (γ) is relieved such that the equilibrium is reached ($dF_{\text{pore}}/dR=0$). This relaxation through the pores enlargement makes the defects visible in the fluorescent images at high magnification.

Single particle spectroscopy measurements on samples prepared with nanorods from the same bulk (mostly backbone shaped) confirmed the previous observations. No statistically significant difference was found between λ_{res} values measured for a population of uncoated nanorods and a population of nanorods that were supposed to be coated with membrane after microstructuring the lipid bilayer on the sample surface.

For the cases when the membrane is draping the nanoparticles and no breakage occurs, it is questionable the extent to that the lipid membrane may adjust its shape in order to follow faithfully the nanorods contour. Considering the cylindrical geometry of the nanoparticle with both ends modeled as spherical caps (Fig.8.19), one can calculate the bending energies per unit area according to Helfrich's formula

$E_{\text{bend}} \approx k_{\text{bend}}(1/R_1 + 1/R_2)^2$, where the bending modulus of a PC bilayer is $k_{\text{bend}} \approx 2 \times 10^{-19} \text{ J}$ ^{115, 116}. The nanorods employed in spectroscopic measurements that shown a spectral shift due to the coating with lipid membrane are characterized by the mean values of $56 \pm 5 \text{ nm}$ length and $26 \pm 5 \text{ nm}$ width. For this geometry, along the length of the nanorod, the bending energy ranges between $2.6 \times 10^{-4} \text{ J/m}^2$ and $6 \times 10^{-4} \text{ J/m}^2$ while at the ends, the contribution of the second finite radius of curvature increases the bending energy which takes values between 10^{-3} J/m^2 and $2.4 \times 10^{-3} \text{ J/m}^2$.

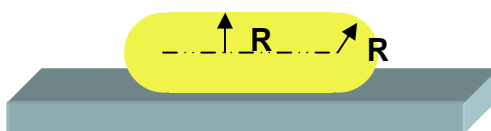


Fig.8.19 Schematic of a gold nanorod on glass surface. The nanorod has a cylindrical geometry with both ends modeled as spherical caps ($R_1=R_2=R$).

For a favorable bilayer spreading on a surface exhibiting topographic irregularities, the adhesion energy should overwhelm the bending energy costs. The interaction between the lipid bilayer and the particles surface is an interplay between the van der Waals, electrostatic and steric hydration forces as a function of the lipid bilayer composition and of the electrolyte properties. In the simplest case for that van der Waals forces are solely responsible for the membrane adhesion, one can calculate the difference between the bending and van der Waals energies for different spacing D between the lipid bilayer and the particle having a cross section radius from 5 to 30 nm (Fig.8.20). In this calculation, since the membrane is supposed to roll around the particle, the van der Waals energy is considered to approximate the energy between two planar surfaces:

$E_{\text{vdW}} = -A/(12\pi D^2)$. The Hamaker constant A of gold/water/hydrocarbon was

estimated at about 3.35×10^{-20} J according to the combining relation 11.24 of Israelachvili⁴⁷ applied to the Hamaker constant values previously reported: 2.5×10^{-19} J for gold/water/gold¹¹⁷ and 4.5×10^{-21} J for hydrocarbon/water/hydrocarbon⁴⁷.

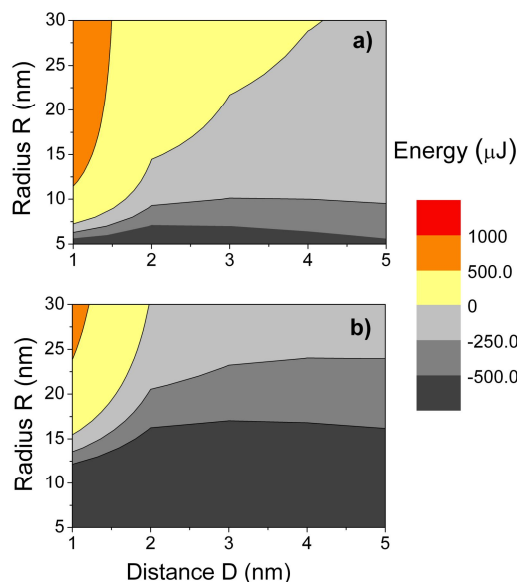


Fig.8.20. Contour plot of the absolute difference between the adhesion and bending energies per unit area of a lipid membrane that is supposed to coat a gold nanorod modeled as a cylinder of radius R , with spherical caps at the ends. D is the distance between the membrane and the particle surface. The representation of the interaction energy is differentiated for two cases: a) along the length of the nanorod; b) at the ends of the nanorod.

Although the calculation is based on a rough approximation of the adhesion energy and therefore does not supply highly accurate numerical values, the data from Fig.8.20 demonstrate the tendency of the lipid membrane that is supposed to coat the nanorod to deviate its conformation from the particle's contour in the regions of the nanorod terminations where the bending energy cost is higher. This tendency is accentuated for decreasing radius of the nanorod cross section.

Depending on the lipid composition of the membrane and/or on the properties of the surrounding electrolyte, the border between the repulsive regime (gray areas) and the more favorable coating regime (yellow areas), is variable. For instance, membranes containing cholesterol are more rigid (since k_{bend} is 4 folds larger) and therefore less amenable to adopt highly curved configurations. By contrast, insertion of PS lipids in the PC bilayer may favor the membrane to bend at higher curvatures due to less steric hindrance of fewer hydration water molecules that are associated with each PS headgroup. Increased values of the buffer pH (basic conditions) may induce ordering of the water molecules at the substrate interface and therefore change the hydration forces while modifications of the buffer ionic strength may tune, by charge screening, the contribution of electrostatic interactions.

In conclusion, the experimental observations point to the importance of the particles geometry that may favor or prevent the breakage of the overlaying lipid membrane. A simplified calculation based on the balance between the membrane adhesion and elastic energies estimates that the coating is less favorable at the nanorods terminations where the bending energy cost is higher.

8.5 Conclusions

I present in this chapter the proof of concept for the construction of an optical biosensor using gold nanorods as sensing elements for monitoring lipid membrane mediated recognition events. To this end, the plasmonic particles are immobilized on glass substrates and covered completely with lipid membrane such that the plasmon resonance shifts caused by changes in the dielectric properties at the membrane interface could be detected with single particle spectroscopy.

A detailed analysis of the nanorods deposition on hydrophilic and amine-functionalized glass surfaces is performed in relation to various factors (such as the pH and ionic strength of the colloidal suspension, nanorods concentration, incubation time) in order to find the optimal conditions for obtaining a homogenous distribution of particles at the desired surface number density. As expected, the surface coverage increases with increasing concentrations of nanorods in solution but this increase is hampered in the presence of excess CTAB. Functionalization with amine terminal groups of the glass surface or of the gold nanorods favors the adsorption of particles to the substrate. Remarkably, one can tune the affinity of the gold nanorods for EDSPA functionalized surfaces by adjusting the pH of the colloidal solution.

The possibility of successfully draping lipid membranes over the gold particles immobilized on the glass substrate was demonstrated with complementary techniques of investigation such as AFM imaging, fluorescence microscopy (including FRAP) and single particle spectroscopy. Coating with the lipid membrane was sensed in the scattering spectra of individual nanorods as 4.46nm average red shift of the long-axis SPR, which means a refractive index sensitivity of about 26nm/RIU. Higher sensitivities (i.e. 62nm/RIU) were measured for nanorods of slightly different geometry. The surface number density and distribution of the nanoparticles on the glass substrate proved to be important for the bilayer formation through the vesicle fusion procedure. At high surface coverage with gold nanorods the membrane exhibits fluid disconnected phases and several large defect areas, mostly as a consequence of the decreased adhesion of the lipid vesicles to the substrate.

The experiments that correlate DF and fluorescence microscopy under identical conditions point to the importance of the nanorods geometry that may favor or prevent the breakage of the overlaying lipid membrane. A simplified calculation based on the balance between the membrane adhesion and elastic energies estimates that the coating with lipid bilayer is less favorable on sharp nanorods, at the extremities, where the bending energy cost is higher.

Chapter 9

Protein-membrane interaction probed by single plasmonic nanoparticles

Motivation for single particle based detection of membrane-protein interactions is provided by the contemporary interest in the construction of miniaturized, high throughput screening devices to detect noncovalent binding events (e.g. for the selection of drug candidates from large libraries of molecules that potentially recognize specific surface receptors). Moreover, detection in the small area regime may exploit valuable information about all involved rate constants as produced by equilibrium coverage fluctuations⁷. Since based on their refractive index sensing properties single gold nanoparticles can be used as sensors for their local environment, the particles may be employed for the investigation of lateral organization in biological membranes. Particularly, elucidation of occurrence and function of nanodomains (also termed rafts) that are required for general membrane function are challenging targets for the proposed detection scheme based on membrane coated particles. Employing particles as nanoscopic reporters for biomolecular interactions on the level of few (<50) proteins offers the possibility to screen lateral inhomogeneities of native membranes.

Proper functionalization of nanoparticles remains an issue if it comes to real world applications, in particular, biological relevant samples such as membrane associated proteins and peptides. In this context, membrane mimics are an attractive solution to achieve an almost native environment with high surface coverage and miniscule nonspecific adsorption. Solid supported membranes are among the most versatile sensing platforms to study both molecular recognition events usually taking place at cellular membranes and ionic transport across bilayers¹¹⁸. A large variety of different model systems have been successfully established, and the approaches include simple self-assembled lipid bilayers on various supports such as glass, metal electrodes, or semiconductors⁷⁹. Lately, more advanced systems were created employing porous supports or using tethered lipids that allow functional insertion of membrane proteins⁴. Only few studies report on particles successfully covered with lipid bilayers^{5,6}. This is mostly because parameters such as membrane curvature and adhesion properties need to be carefully adjusted, as it was shown in the previous chapter.

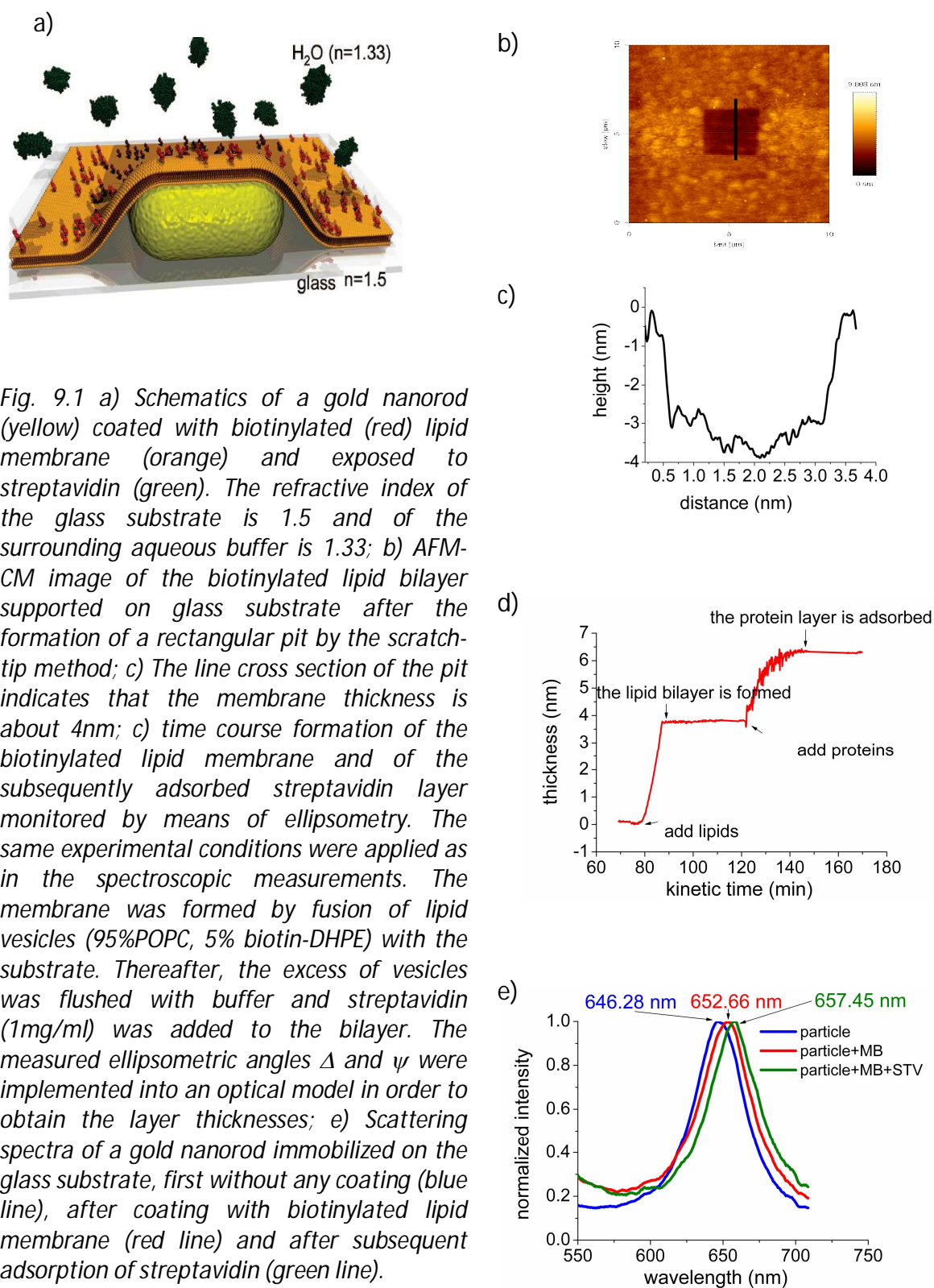
9.1 Sensing the adsorption of streptavidin to biotinylated lipid membranes

The sensing elements are individual gold nanorods immobilized randomly on a hydrophilic glass substrate and coated entirely with fluid membrane (POPC) displaying biotin moieties (5% Biotin-DHPE). The adsorption of streptavidin to the biotinylated bilayer is detected with single particle spectroscopy as a red-shift of the longitudinal SPR wavelength for each single plasmonic particle whose scattering spectra is measured.

The schematic of a gold nanorod draped with lipid membrane and exposed to protein adsorption is shown in Fig. 9.1a. Successful coating of gold particles with fluid lipid bilayer composed of POPC lipids doped with Biotin-DHPE was previously checked with complementary experimental techniques (fluorescence microscopy, FRAP analysis and atomic force microscopy) as described in the previous chapter. The diffusion coefficients determined by FRAP analysis have the same values as in the control experiments (performed in the absence of gold nanoparticles) and demonstrate that the lateral mobility of lipids in the supported membrane is preserved.

The scattering spectra of a single nanorod show a resonance red-shift of 6.38nm after coating the particle with lipid membrane and an additional shift of 4.79nm after subsequent adsorption of streptavidin (Fig. 9.1b). With this LSPR sensing technique, binding/adsorption events can be highly localized within the range of the decay length of the evanescent field (about 20 nm).

LSPR shift is not only dependent on the refractive index of the adsorbed layers but also on the layers thicknesses (the amount of adsorbed molecules). This dependency decreases exponentially from the nanorod surface with any intermediate functionalization layer that places the interacting sites further from the particle interface. As ultrathin films, the lipid membranes that are coating directly the plasmonic particles do not affect considerably the detection sensitivity for protein adsorption. The thickness of the biotinylated membrane was measured with AFM and ellipsometry. A scratch- tip method was applied with AFM-CM to create a rectangular pit in the glass supported lipid bilayer. Subsequent imaging of a larger area of the membrane including the pit indicates that the bilayer has a thickness of about 4 nm (Fig.9.1d-e). The same value of the biotinylated membrane thickness was determined by means of ellipsometry. Kinetic measurements with this technique indicate that, after addition of streptavidin to the lipid membrane, the protein adsorption reaches the equilibrium after 20 minutes when a stable protein layer of 2.34nm thickness is formed (Fig.9.1c). Similar ellipsometric measurements were performed for the adsorption of streptavidin to POPC lipid membranes doped with biotin-X-DHPE lipids. The protein layer thickness was this time 3.12nm (data not shown).



9.2 Detection sensitivity

Using the single particle spectroscopy setup equipped with an electronically addressable shutter, 29 particles on the sample were analyzed simultaneously during a single experiment. Considering all investigated particles, a median shift of $3.6 \pm 1.5 \text{ nm}$ is observed for the longitudinal SPR wavelength, which is caused by coating the particles with biotinylated (biotin-DHPE) lipid membrane (Fig.9.2a). Binding streptavidin to the membrane determined a second spectral shift of $2.9 \pm 1.8 \text{ nm}$. Removal of both adsorbed layers (lipids and proteins) from the nanorods surface, by washing the sample with Triton X-100 solution (4% v/v), changed the direction of the resonance shifts toward smaller values of the wavelengths. The initial position of the resonance peaks was recovered with an accuracy of $0.5 \pm 2.7 \text{ nm}$.

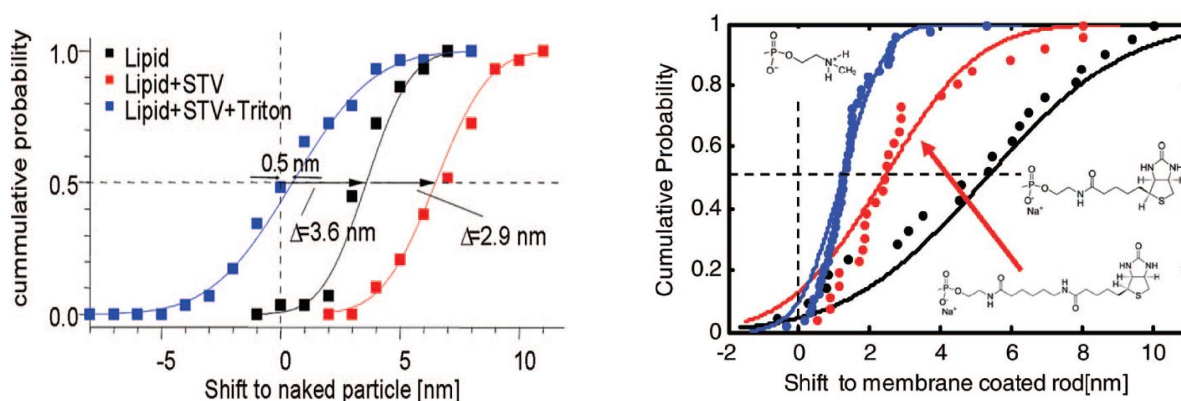


Fig.9.2 a) Cumulative probabilities of spectral shifts derived from observing simultaneously 29 particles with single particle spectroscopy during their coating with biotinylated lipid membrane, adsorption of streptavidin and washing with Triton X-100 solution. The solid lines show the cumulative probability for the Gaussian distributions having the experimental median values and standard deviations; b) Cumulative probabilities of the spectral shifts caused by the adsorption of streptavidin to three different lipid bilayers: POPC membrane doped with biotin-DHPE (black), POPC membrane doped with biotin-X-DHPE (red), non-biotinylated POPC membrane (blue). The solid lines show the cumulative probabilities for Gaussian distributions having the experimental median values and standard deviations.

To further test the sensitivity of the method, similar measurements were performed under identical conditions as in the previous experiment, making only a small change in the composition of the lipid membrane: biotin-DHPE (that has biotin directly attached to the lipid group) was substituted with biotin-X-DHPE (for that biotin is attached via a C_6 spacer). A smaller median shift caused by the adsorption of streptavidin was in this case recorded, namely $2.4 \pm 2.1 \text{ nm}$. The presumed increase of separation between the streptavidin molecules and membrane lipids may serve as an explanation for the smaller spectral shift of the resonance wavelength since it is well known that the plasmon sensitivity decreases with the distance from the nanoparticles surface. Control experiments performed with lipid membranes containing no biotin shown an

insignificant mean spectral shift of the particles' plasmonic resonance when streptavidin was added to the sample.

In order to compare the experimental findings with the theory, the plasmon resonance shifts were estimated in the framework of quasi-static approximation (Fig.9.3).

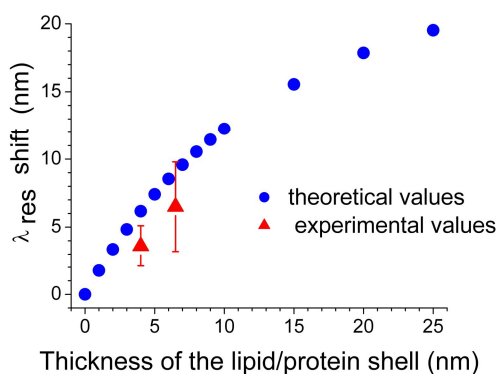


Fig.9.3 Calculated spectral shift versus the thickness of the lipid/ protein coating layer. The calculation is done in the framework of the quasi-static approximation for a prolate spheroid corresponding to a gold nanorod having, respectively, 56nm and 26nm along the major and minor axes. The coated particles are placed on a glass substrate. The mean values of the experimentally measured spectral shifts are represented for comparison

The calculation is done for a prolate spheroid corresponding to a gold nanorod having 56nm and 26nm along the major and minor axes, respectively. These are the mean dimensions (resulted from TEM analysis) of the nanorods used in the spectroscopic measurements. The lipids and protein layers are considered to have the same dielectric constant and to wrap completely the particle, forming a shell of variable thickness. The influence of the underlying glass substrate which is in contact with the coated nanorod was taken into account by introducing an averaged dielectric function of the glass and of the aqueous solution²⁷. The experimental and theoretical results are closely comparable. A smaller spectral shift is however always measured in experiments due to the fact that in reality the lipid membrane drapes only the upper surface of the nanorods and than leaves the nanoparticles contour when the bending energy becomes unfavorable.

9.3 Potential extension of the nanosensor applicability

Based on the capability of detecting highly localized changes in the dielectric properties of the nanorods environment, the sensing platform arranged in a 2D array format as described previously, may find a potential application in the analysis of shape fluctuations of giant unilamellar vesicles (GUVs) and even cells. In fluid phase, the lipid membrane of giant liposomes (typically tens of micrometers in size) and of the erythrocyte membrane prove to have low resistance toward bending and shearing, exhibiting pronounced thermal shape fluctuations¹¹⁹⁻¹²¹. In living cells, form fluctuations are not only thermally driven but can be actively pursued by energy-consuming activities of the cellular cytoskeleton¹²². Different techniques such as flicker spectroscopy¹²³, defocusing microscopy¹²⁴, phase contrast microscopy¹²⁵ or combined reflection interference and phase contrast microscopy¹²⁶ have been employed and adapted to study the shape fluctuations of GUVs or cells such as erythrocytes or macrophages¹²⁴.

The fluorescent image of a giant unilamellar liposome consisting of POPC/POPS 4:1 lipids labeled with sulforhodamine-DHPE (1%) is shown in Fig.9.3a. In dark field microscopy the light scattered from the walls makes the vesicle contour visible (Fig.9.3b). The Brownian motion of the membrane surface causes rapid fluctuations of the scattered light.

By gentle hydration method, GUVs of various shapes could be formed and thermal fluctuations were observable in DF microscopy for the entire range of the adopted shapes. In Fig.9.3b the vesicle is locally attached to the amine-functionalized substrate but simultaneously exhibits a repulsive long range disjoining pressure caused by the undulation forces. Employing their local refractive index sensing properties, the plasmonic particles may perceive the nearby membrane bending oscillations through changes in the dielectric properties of the local environment and transduce them into fluctuations of the longitudinal plasmon resonance frequency that may be recorded by single particle spectroscopy. Simultaneous monitoring of several particles may provide a large amount of data containing information about the local dynamic behavior of the lipid membrane.

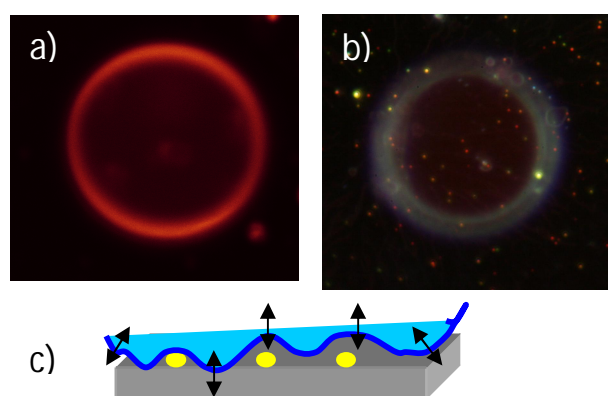


Fig.9.3 a) Fluorescent image of a single GUV (24 μ m diameter) consisting of POPC/POPS 4:1 lipids labeled with sulforhodamine-DHPE (1%); b) DF image of the GUV placed on amine functionalized glass surface with gold nanorods. The light scattered from the walls makes the vesicle contour visible; c) Thermally induced shape fluctuations schematically illustrated for a GUV fragment (blue) interacting with the solid substrate (grey) with gold nanorods (yellow).

From the analysis of GUVs shape fluctuation, one can extract relevant parameters describing mechanical properties of the lipid membranes (i.e. bending modulus) as a function of their composition (cholesterol or charged lipids content, inserted proteins), temperature, viscosity or osmolarity of the outer medium. Although in living cells the plasma membrane is coupled to the actin cortex of the cytoskeleton, on a local scale, the membrane is often decoupled and exhibits small scale undulations with wavelengths of the order of 0.5 μ m and amplitude of 10nm¹²⁷. For living cells, additional factors such as aging, pathological transformations or subtle changes in the membrane structure caused by diseases and drugs can affect the mechanical properties of the plasma membranes and may be reflected in the cell shape fluctuations

9.4 Conclusions

Adsorption of streptavidin to biotinylated membranes coating gold nanoparticles was successfully detected by means of DF single particle spectroscopy.

Membrane coated plasmonic nanoparticles provide a sensing platform that combines single particle sensing with a perfectly functionalized native coating. In this way, nanoparticles can serve as reporters for cellular reactions taking place on and within biological membranes. Lateral heterogeneity of cellular membranes can be probed with nanometer resolution employing monoclonal antibodies to detect small lipid domains or protein clusters on the membrane surface. Furthermore, membrane coated particles offer the advantage to suppress unwanted nonspecific interactions because of the presence of the membrane, while providing an extremely small active area.

Hence, it will be conceivable to create sensors based on the detection of equilibrium coverage fluctuations that would circumvent problems arising from mass transport and drift of the sensor signal. As a consequence, complex processes such as cooperative adsorption, adsorption to heterogeneous surfaces, and slowly evolving systems can be addressed by fluctuation analysis.

Chapter 10

Phase imaging with AFM reveals increased activity of PLA₂ on highly curved membranes

While height images acquired with AFM are sufficient to accurately characterize the successful reconstitution of lipid membranes on flat solid supports, they may not allow the recognition of small defects in the lipid membranes that are spread on rough surfaces exhibiting nanometer scale irregularities (i.e. immobilized gold nanorods on glass substrates). Complementary information to the sample topography is provided in TM-AFM by simultaneously mapping the phase lag of the cantilever oscillations relative to the signal sent to the cantilever's piezoelectric driver. The phase contrast, which arises from variations in the composition of the sample surface, is therefore considered in this work to differentiate the nature of the substrate and to identify potential breakdowns of the lipid membrane draping the nanorods.

Known for its catalytic activity on lipid hydrolysis, phospholipase PLA₂ was used to induce local depletion of lipids from the substrate in order to probe, by comparing the AFM phase images recorded before and after the enzymatic activity, the initial continuity of the lipid membrane coating the gold nanorods. The motivation for using PLA₂ in these experiments was mostly conducted by the hypothesis that the hydrolytic activity of the enzyme would be initiated at the points where the cleavage sites of the lipids are better exposed due to the high curvature of the membrane, namely at the locations where the bilayer bends over the particles. An increased activity of PLA₂ on lipid micelles and vesicles than on planar membranes was suggested in previous studies^{128, 129}, but not directly demonstrated because of the difficulty to compare the enzymatic activity in two different systems (i.e. vesicles suspensions and solid supported lipid bilayers) via the same investigation technique, maintaining the same experimental conditions (i.e. the concentrations of the enzyme or of the lipids, identical buffer conditions, etc).

In the present work, the samples consist in lipid bilayers that are draped over nanoparticles immobilized on glass substrate and expose simultaneously to the enzymatic activity, under identical conditions, flat and locally curved regions. This experimental platform is subjected to the investigations via complementary techniques (AFM, fluorescence microscopy and ellipsometry) such that a straightforward conclusion is drawn on the influence that the membrane curvature has on the enzymatic activity of PLA₂.

10.1 Structure and function of phospholipase PLA₂

Phospholipase A₂ (PLA₂) catalyzes the hydrolysis of the *sn*-2 acyl bond of phospholipids to produce lysophospholipids and free fatty acids (Fig. 10.1). Over the last decade, the superfamily of PLA₂ enzymes has been characterized as comprising fifteen groups, including four main types: secreted sPLA₂, cytosolic cPLA₂, calcium independent iPLA₂ and lipoprotein associated lp-PLA₂. The enzyme plays a prominent role in several physiological processes including phospholipid digestion and metabolism, host defense and signal transduction.

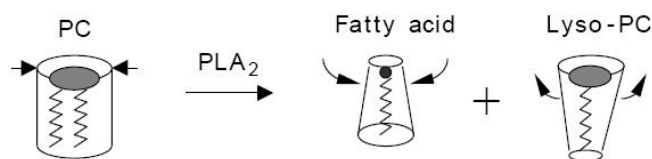


Fig. 10.1 Schematics of PLA₂ catalyzed hydrolysis of a diacyl lipid (PC) into a fatty acid and a lysophospholipid (according to Hoyrup et al.¹³⁰).

The activity of secretory PLA₂ is strongly enhanced upon binding to the substrates that are present in aggregates such as lipid bilayers or micelles, as compared to the activity on isotropically dispersed phospholipids. Studies on bee venom PLA₂ have determined that the primary attachment site to a lipid bilayer is near the active site of the enzyme that acts according to the "scooting model": the enzyme remains attached and moves among sites to cut the phospholipids^{131, 132}. The physicochemical properties of the lipid membranes play a major role in modulating the PLA₂ activity. Structural defects and fluctuations that occur near phase transition temperatures are known to increase the activity of the enzyme¹³³. It has been shown that, following the phospholipid hydrolysis, the lysophospholipids are preferentially removed from the lipid bilayer while the fatty acids accumulate in the membrane and modify its morphology and stability¹³⁴.

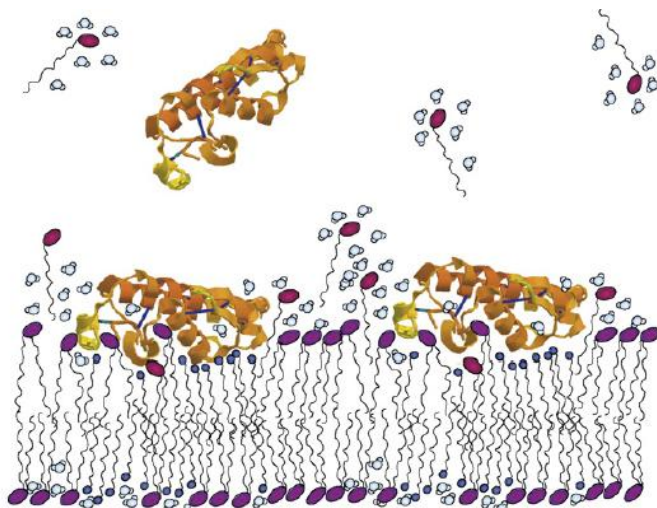


Fig. 10.2 Schematics of PLA₂ interaction with the lipid membrane according to Wacklin et al. Fatty acids (small blue head group) accumulate in the bilayer as the lyso-phospholipids (large red head group) partition into the solution¹³⁴.

Secretory PLA₂ isolated from bee venom was used in this work. This phospholipase belongs to the large family of extracellular PLA₂ that is widespread in various mammalian cells and tissues, as well as in snake, lizard and insect venom. The enzyme is small, consisting of a single polypeptide chain of approx. 123 aminoacids and perform phospholipid hydrolysis using a His-Asp doublet plus a conserved water molecule as a nucleophile, and a calcium ion as a cofactor.

10.2 Characterization of PLA₂ activity with ellipsometry

The enzymatic activity of PLA₂ on solid supported lipid membranes in fluid phase (POPC) and in gel phase (DPPC) was characterized at room temperature by means of ellipsometry. This technique is especially suited for sensitive and noninvasive detection of the lipase activity. PLA₂ is interfacially activated and induces structural modifications of the lipid bilayer. These modifications (of the membrane thickness and/or of the surface coverage) can be derived from the time course variation of the ellipsometric angles, as average values for selected areas on the sample. The lipid membranes were microstructured on freshly oxidized silicon wafers such that it was possible to select and monitor simultaneously several regions of interest either on the bare silicon surface or on the supported lipid membrane. Fig.10.3 shows that, under similar conditions, the phospholipase PLA₂ catalysed the hydrolysis of lipids in both membranes, POPC and DPPC bilayers, but manifested a lag in the case of gel phase lipids (DPPC).

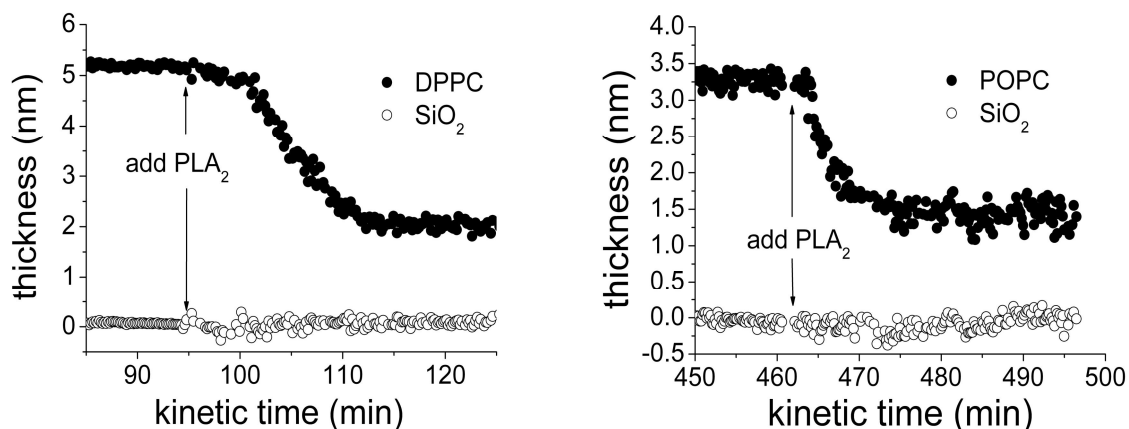


Fig.10.3 Time course dependences of the lipid bilayer thickness during the hydrolysis of DPPC (left) and POPC (right), under similar conditions (same buffer containing 5mM CaCl₂, pH=8.9, 0.3μM final concentration of PLA₂). In order to detect possible adsorption or/and agglomerations of the hydrolysis products to the solid substrate, regions of interest were selected for each sample on the bare silicon (o) and on the lipid membrane covered substrate (●).

The lag phase observed in the hydrolysis of lipids in gel phase is most probably a consequence of the initial state of the membrane consisting of well organized and tightly packed lipids that do not allow the bound enzymes to access their cleavage sites. It was recently suggested by Wacklin et al.¹³⁴ that, besides the adsorption to the lipid-water interface, a partial subsequent penetration of the enzyme into the lipid hydrocarbon core

of the membrane is required, and this constitutes a second rate limiting step for the catalytic activity of the enzyme. It is therefore conceivable that the phospholipase starts its hydrolyzing activity at a much lower rate, most probably from the edges and defects of the microstructured bilayer. The resulting hydrolysis products (fatty acids and lysolipids which are known to be membrane permeabilisation agents) induce changes in the state of the membrane and determine the reorganization of the nonhydrolysed lipids. Modifications of the membrane state and accumulation of the adsorbed PLA₂ during the lag phase trigger the burst in the enzyme behavior that changes suddenly from a regime of low activity to a regime of rapid hydrolysis. AFM measurements revealed a similar lag phase of about 8-10 min. in the activity of snake venom PLA₂ on DPPC bilayers supported on mica¹²⁸. As compared to the gel phase lipids, under identical experimental conditions, the ellipsometry measurements show that the hydrolysis of the lipids in fluid phase (POPC) started almost immediately after the injection of the enzyme.

The extent of the enzymatic activity (expressed as the ratio between the amount of lipids that are gradually removed from the silicon-buffer interface during the hydrolysis process and the initial amount of supported lipids), in a selected region of interest of the lipid membrane is plotted as a function of time, in Fig. 10.4a, for the bilayers in fluid (POPC) and in gel (DPPC) phase.

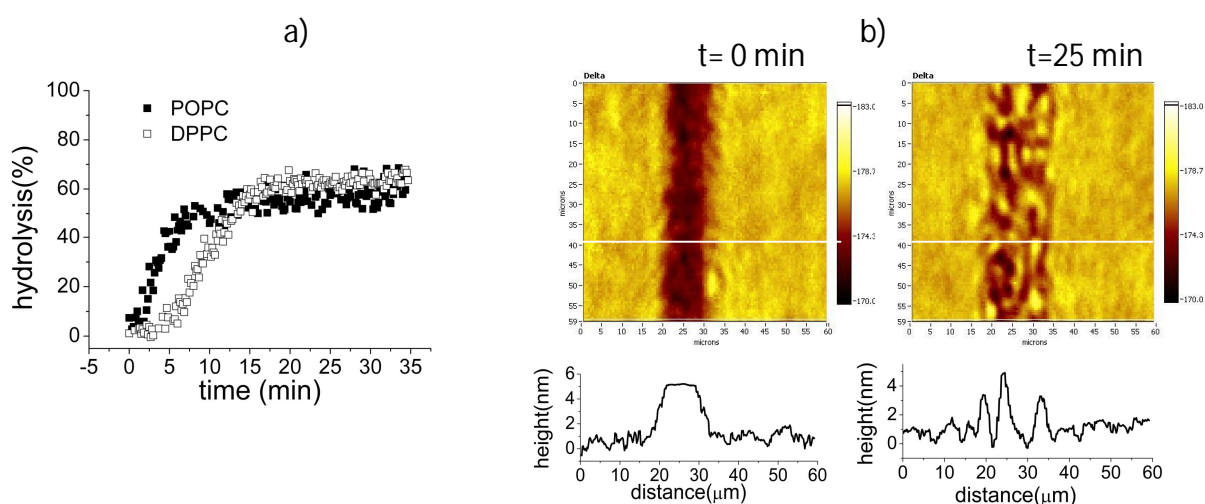


Fig. 10.4 a) Time course dependency of the apparent hydrolysis of POPC and DPPC bilayers, expressed as the percentage of lipids that dissociate from the membrane; b) Delta maps ($60 \times 60 \mu\text{m}^2$ image size) of the DPPC microstructured membrane before the addition of PLA₂ and 25 minutes later. The corresponding membrane thickness profile along the line cross sections (white line) of delta maps are obtained after implementing the delta values into the optical model and represented beneath the delta maps.

One can see that both bilayers (in gel and fluid phase) are hydrolysed up to about 65% of their total volume, independent on the previous time course of the hydrolysis. This percentage gives however only the apparent dimension of the maximal extent of the lipid hydrolysis because a part of the resulting reaction products, especially fatty acids, may accumulate in the membrane. Delta map of a DPPC bilayer that was microstructured on the oxidized silicon substrate was recorded before the addition of PLA₂ and 25 minutes

later, when the hydrolysis process ended (Fig. 10.4b). It is interesting to observe that, following the enzyme activity, the lipid membrane was completely removed from the substrate only on certain areas that seem to follow a kind of channel pattern. This result supports the “scooting model” hypothesis that was advanced to characterize the activity of PLA₂ and confirms previous observations from AFM measurements¹³⁵, which show that the enzyme forms initially small holes in the lipid bilayer and these holes elongate in a channel shape that extends and gets more and more enlarged.

As the Delta map shows (Fig. 10.4b) at the end of the hydrolysis process, regions of bare silica substrate that were completely depleted of lipid membrane, one can deduce that, besides the lysolipids, at least a part of the fatty acids resulting from the lipase activity are solubilized in the buffer solution. The efflux of the degradation products from the lipid membrane is dependent on the transport conditions existent in the fluid phase which is in contact with the membrane. A continuous flow (0.5ml/min) of the PLA₂ containing buffer was insured in the measuring cell of the ellipsometer during the kinetic measurements. The solubilization of the hydrolysis products was yet limited to the same volume of buffer (1.3ml) that was recirculated through the flow cell during the hydrolysis process. This limitation in the solubility of the degradation products may explain why the maximal extent of the apparent hydrolysis activity (expressed as the maximal percentage of lipids that dissociates from the membrane) had the same value (65%) for both, DPPC and POC bilayers under identical experimental conditions.

The end point of the hydrolysis may be achieved when the lipid-product mixture reaches a certain composition/ratio at which the PLA₂ becomes catalytically inactive. In a first stage, the accumulation of the hydrolysis products increases the interfacial disorder and facilitates the enzyme adsorption and its access to the cleavage sites, triggering in this way the burst in the lipase activity, in the following step, the lipase activity may be blocked by the considerable accrual of fatty acids into the membrane. It was demonstrated that the negative potential of lipid vesicles and planar bilayers increases in the presence of PLA₂ under catalytic conditions¹³⁶ due to the accumulation of fatty acid into the membrane. The enzyme, which is known to have several cationic residues that participate in the interaction with the lipid bilayer, may exhibit stronger electrostatic interaction with the anionic lipids. When high fractions of fatty acids are present in the membrane, they may laterally segregate and form negatively charged patches that sequester the phospholipase into catalytically inactive aggregates via strong electrostatic interactions.

10.3 Phase imaging with AFM

The incipient stage of PLA₂ activity on supported lipid bilayers spread on glass substrates with gold nanorods was monitored by phase imaging with atomic force microscopy. In TM-AFM, the phase shift between the excitation and the response of the cantilever is generated as a material-dependent signal, complementary to the sample topography. According to the phase shift caused by changes in the adhesive and viscoelastic properties of the scanned surface, the AFM phase image reveals nanometer scale information about the membrane heterogeneities induced by the enzymatic hydrolysis. Fig. 10.5 shows height and phase images recorded before and few minutes after addition of the enzyme into the measuring cell. Shortly after injecting the lipase (to a final

concentration of $0.3\mu\text{M}$ in Tris buffer pH=8.9), the sample was gently washed with lipase-free buffer to remove the degradation products from the surface vicinity. To allow a direct comparison of the phase images, the sample was scanned based on similar TM-AFM operation parameters.

One of the major issues is to probe the integrity of the lipid membrane that is supposed to coat the gold nanorods on the glass substrate. Since the phase lag reflects the interaction between the scanning tip and the material of the sample surface, an uncoated gold particle (which is considerably more rigid in comparison to the rest of the surface covered with lipid bilayer) would generate a strong local phase shift in the phase image. In Fig. 10.5a, the nanorods are obviously signalized as high features in the height image, but the corresponding phase image shows almost no phase shift as compared to the rest of the surface. This observation attests the continuity of the lipid membrane that was draping the nanoparticles on the glass substrate before the enzymatic activity of PLA_2 . Few minutes after the addition of the enzyme, the phase image shows an evident positive phase shift across the imaged nanorods (Fig.10.5 b and c) indicating that the surface properties of the particles and of a small area around them changed with respect to the rest of the sample.

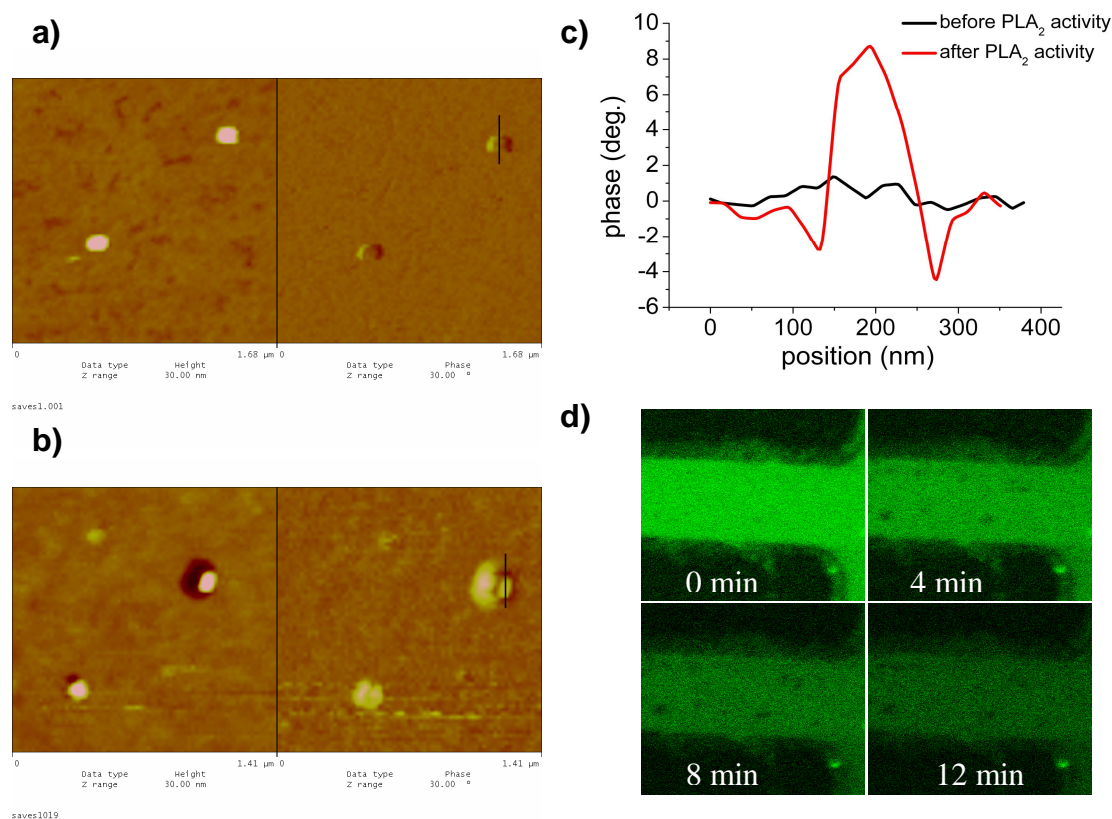


Fig. 10.5 a) TM-AFM images (left: height channel and right: phase channel) of gold nanoparticles on glass substrate draped with POPC lipid membrane. The images were recorded at room temperature prior to (a) and after (b) adding the phospholipase PLA_2 to a final concentration of $0.3\mu\text{M}$. Before imaging, the sample was each time washed thoroughly with buffer, to remove either the excess of lipid vesicles or the excess of unbound PLA_2 and hydrolysis products. To allow a direct comparison of the phase images, the sample was

scanned based on similar TM-AFM operation parameters. c) The change in the phase profile of the line cross sections of the nanorods imaged before and after adding the lipase to the sample; d) Fluorescence images (29x29 μm^2) taken during the hydrolysis activity of PLA₂ on the POPC lipid membrane (labeled with β -Bodipy C₁₂-HPC) that was microstructured on hydrophilic glass substrate on top of gold nanorods.

The AFM images demonstrate that the membrane degradation starts and extends from the top of the particles where the membrane exhibits high local curvatures that facilitate the access of the lipase to the cleavage sites of the lipids. The bright phase contrast that is visible in the phase image (Fig. 10.5 b) is caused by the repulsive interaction between the scanning tip and the small area of the substrate (including the nanoparticle) that was stripped of the lipid membrane.

The observation that PLA₂ exhibits increased enzymatic hydrolysis of lipids located in highly curved regions of the lipid membranes is supported by fluorescence images of a labeled POPC bilayer that was exposed to the same concentration of phospholipase as in the AFM experiments. The membrane was microstructured on a hydrophilic glass substrate with gold nanorods and imaged during its degradation with PLA₂ (Fig. 10.5d). Shortly after the addition of the enzyme (4min later), one can notice the appearance of few black spots on the previously intact membrane, as a result of fast local degradation of the lipids only in certain positions. The enzymatic activity continues slower and extends from these "access points" that most probably correspond to the location of the nanorods that were previously underlying the continuous lipid bilayer. While the hydrolysis process advances, the degradation products start to accumulate either in the membrane or in its immediate vicinity. This process is favored by the absence of a fluid flow and by the small volume of buffer in the measuring cell. Accumulation of the residual fluorophores close to the sample surface alters the background of the fluorescence images that become hazy and miss the necessary contrast for monitoring further the membrane hydrolysis process.

The AFM and fluorescence images recorded in this study for monitoring the incipient activity of PLA₂ on solid supported lipid membranes corroborate to the conclusion that the hydrolysis of lipids is initiated faster at the sites where the membrane bends over irregularities such as nanoparticles immobilized on the substrate. This observation is in agreement with previous findings that PLA₂ exhibits higher activity on micelles and vesicles in comparison to planar bilayers^{128, 129, 135}. Higher PLA₂ activity was also found toward ripple phase membranes characterized by a corrugated morphology as compared to the gel phase lipid bilayers¹³³. The preferential hydrolysis of highly curved membranes resides in the prerequisite interfacial activation of the enzyme that seems to be sensitive to the strength of PLA₂ binding to the membrane as well as to the depth of membrane insertion.

10.4 Conclusions

Phase imaging with AFM confirm, based on the interaction of the scanning tip with the surface material, the continuity of the lipid membrane drapped on the gold nanorods. Corroborated evidence from AFM and fluorescence images recorded during the incipient activity of phospholipase PLA₂ on solid supported lipid bilayers demonstrate that the hydrolysis of lipids is initiated faster at the sites where the membrane bends over irregularities such as nanoparticles immobilized on the substrate. It is therefore confirmed the hypothesis of increased hydrolytic activity of PLA₂ on highly curved regions of membranes due to facilitated acces of the lipase to the cleavage site of the lipids.

Chapter 11

Influence of the nano-scale gold surface topography on the lipid vesicles adhesion

11.1 Introduction

The interactions of lipid vesicles with solid substrates are essentially dependent on the surface properties, on the nature of the lipids that constitute the vesicles, as well as on the environmental conditions. The main interactions consist of van der Waals and electrostatic interactions to that one can add the undulation (entropic) repulsions and the hydration repulsion¹¹⁴. Theoretical studies by Lipowsky and Sackman¹¹⁴ suggested that the progression between the vesicle adhesion to the rupture and bilayer formation is determined by the balance between the net attractive energy of membrane-substrate interaction and the elastic properties of the lipid membrane. In some cases, the interactions between the adhered vesicles that reach a certain critical surface concentration may also contribute to the vesicle fusion and spreading^{14,137}.

There are three regimes that one can distinguish in relation to the interaction between the lipid vesicles and the solid substrates: i) the interaction is too weak or even repulsive such that no vesicle adhesion takes place; ii) the interaction is moderate, vesicles adhere to the substrate but they remain intact; iii) the interaction is strong enough such that the energy of the adsorbed membrane patch is more favorable than that of the adsorbed vesicle and therefore the vesicle ruptures on the surface.

On planar gold substrates the regime iii) is generally reached if the metal surface is initially functionalized with charged self assembled molecules (such as MEA or MPA)² which allow the adsorption of oppositely charged lipid membranes^{118,138}. Alternatively, lipid membranes can be covalently anchored on gold if they contain lipids that are functionalized with thiol anchors attached to the head groups either directly or via a hydrophilic spacer. Untreated gold surfaces exhibit very little affinity toward the formation of lipid membranes that do not contain functionalized lipids. Bare gold micro-

² MEA=mercapto ethylammonium hydrochloride (positively charged); MPA=3-mercaptopropionic acid (negatively charged)

patterns on hydrophilic silica substrates were proved to act as highly effective barriers to lipid diffusion in the supported membranes. It seems that on bare gold, lipid vesicles do not adhere at all or, once the vesicles are adhered to a certain extent, they spread into lipid bilayers that lacks completely their long range fluidity¹³⁹. The mechanism by which gold substrates function as barriers to lipid diffusion is not clear yet and may be very much dependent on the previously applied cleaning procedures or storage conditions. Lipid bilayer formation by fusion of small vesicles was recently observed on gold surfaces that were previously annealed with hydrogen-oxygen flame to obtain atomically flat (111) terraces in the surface structure¹⁴⁰. Adsorption of liposomes that remain intact on bare gold substrates was also reported¹⁴¹ although it is not clear to what extent this adsorption is significant in terms of surface coverage. Only sparse adhesion of lipid vesicles that eventually fused with the substrate in a proportion of 80% was observed on bare gold surfaces while under identical conditions lipid vesicles of similar composition adhered and remained stable on acetyl-cysteine modified gold substrates¹⁴². Stable adsorption of intact phosphatidylcholine vesicles of very small size (25-30nm radius) on gold was experimentally observed with quartz crystal microbalance (QCM) technique when the gold surface was previously oxidized to render it more hydrophilic^{143, 144}.

I will show in the following that, without any chemical treatment, topographic modifications on a nanometer scale of the gold surface change drastically the adhesion properties of gold for large unilamellar lipid vesicles. The evidence is given by an increased fluorescent signal acquired from the fluorescently labeled liposomes that adhere preferentially and remain intact on the gold substrates the topography of which was modified on a nanometer scale.

11.2 Experimental

Preparation of the substrates: Glass coverslips were used as solid supports after consecutive cleaning by sonication in Helmanex and Milli-Q water as described in Section 3.2.1. The first level of structuring consisted in the deposition on these substrates of thin (20nm) gold stripes (900mm length and 100 μ m or 500 μ m width) via thermal evaporation through a metallic mask, using a Vacuum Coating System BAE 250. A thin layer of chromium (5 nm) was used to promote the adhesion of the gold film to the underlying glass substrate. Gold nanorods were afterwards immobilized on these samples. Either the entire surface was covered with a homogenous distribution of particles or, by means of soft lithographie, a micropattern (stripes of 15 μ m width) was formed. This second level of structuring was achieved via micromolding the nanorods suspension into capillaries formed by conformal contact between the substrate and PDMS stamps (see Section 3.5 for the procedure details). After each step of incubation with the nanorods suspension or with lipid vesicles suspension, the samples were thoroughly washed with Milli-Q water or with buffer (20 mM Tris/HCl, 100 mM NaCl, 1mM CaCl₂, pH 7.4).

Gold nanorods were obtained from Nanopartz. The average sizes of the particles as result from TEM (and in agreement with the product description) are 60nm length and 30nm diameter. Before immobilization, the gold nanorods were washed two times by consecutive centrifugation and resuspended in Milli-Q water.

Large unilamellar lipid vesicles (LUVs) were prepared by the extrusion procedure (described in Section 3.3) from uncharged lipids (POPC) or mixtures of charged lipids (4:1

POPC/POPS) that were fluorescently labeled either with β -Bodipy C12-HPC or with sulforhodamine-DHPE (1%mol).

DF and Fluorescence imaging was performed with an Olympus upright microscope using 10x, 40x, 100x water immersed objectives. Images were acquired either with a commercial camera Canon Power Shot A95 that replaced one of the microscope's oculars or with ColorView II digital microcamera Olympus.

FRAP measurements were performed with a Leica LCS SL confocal laser scanning microscope according to the procedure described in Section 3.6.

11.3 Results and discussion

For a direct comparison between the interaction of lipid vesicles with glass and with gold substrates, gold was thermally evaporated on clean glass coverslips through metallic micro-structured masks that were overlaid on their surface such that parallel gold stripes (100 μ m or 500 μ m width) were formed. The nanoscale topography of the sample was modified by adsorption of gold nanorods at a controlled surface number density. After immobilization of particles, the samples were thoroughly washed with Milli-Q water to remove the nanorods that did not adhere to the surface. The dark field (DF) images of these samples are shown in Fig.11.1.

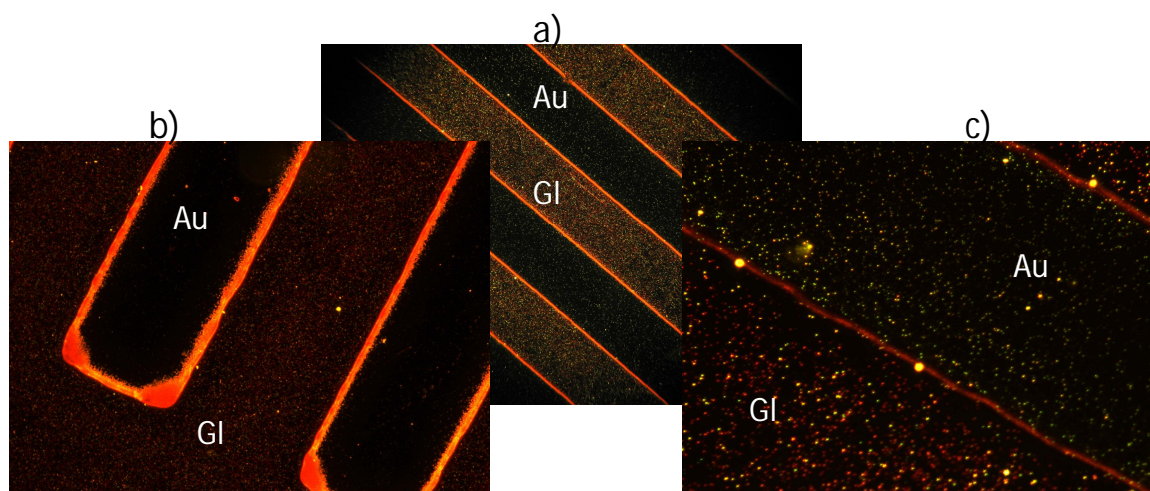


Fig. 11.1 DF images in transmission mode (real colors). The samples consist of gold stripes (20nm out of plane) on glass substrates, with gold nanorods on top (see text). a) The gold stripes are 100 μ m wide, the image was acquired using a 10x water immersed objective, with a commercial Canon camera that replaced one of the microscope's oculars; b) The gold stripes are 500 μ m wide, the image was acquired by a 10x water immersed objective with Olympus color camera; c) The gold stripes are 100 μ m wide, the image was acquired by a 40x water immersed objective using a digital microcamera ColorView II Olympus. "Au" and "Gl" are used to mark the gold stripes and the glass substrates respectively.

Under dark field illumination, the gold particles on glass appear as red spots due to their LSPR wavelength which is spectrally located in the visible range (average $\lambda_{res} = 628$ nm). On the gold substrates however the plasmonic particles are not well visible because of

their reduced scattered light intensity. Reduced visibility of the nanorods placed on the planar gold surfaces is also due to the fact that the DF images are acquired in transmission mode and therefore the illumination coming from the DF condenser passes additionally through the gold films of 20 nm thicknesses. (Practically the gold substrates are optically transparent since the skin depth of gold is about 23nm in visible range).

It is interesting to notice the tendency (mostly visible in Fig.11.1c) of the plasmonic particles placed on the gold films to scatter light in the green range of the visible spectra, maybe as a consequence of the inter-particle coupling intermediated by the underlying gold layer. Also intriguing is the spectral behavior (red scattered light) in DF of the gold stripe edges. Unless another phenomenon is present, it may be possible that to the brightness of the red lines contribute gold nanorods which, due to the step change in the surface topography, could align themselves along the edges of the gold stripes. Any particle aggregates or dust particles would scatter white light according to their size and shape without exhibiting a spectral characteristic.

The samples shown in Fig.11.1 were incubated for about 20-25 min with a suspension of 0.5mg/ml large unilamellar lipid vesicles (4:1 POPC/POPS) fluorescently labeled with β -Bodipy C12-HPC. After incubation, the samples were thoroughly washed with the same buffer as used for the lipid vesicle suspension. Fluorescence images of these samples before and after incubation with lipids are shown in Fig. 11.2.

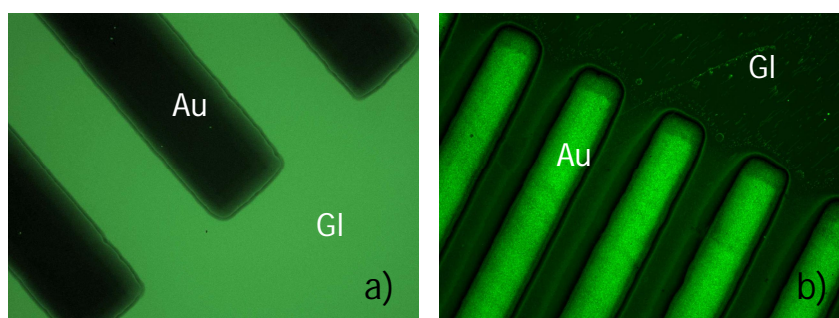


Fig. 11.2 Fluorescence images (false colors) of the samples shown in Fig.11.1 taken before (a) and after (b) incubation with lipid vesicles (see text). The gold stripes (100 μ m wide) are marked by "Au" and the glass substrate is indicated by "Gl". The images are acquired with an upright fluorescence microscope using 40x (a) and 10x (b) water immersed objectives.

Fluorescence images obtained after incubating the sample with lipid vesicles (Fig.11.2b) reveal an obviously increased fluorescence signal coming from the gold stripes (marked with "Au") as compared to the fluorescence signal of the glass substrate (marked with "Gl"). Before the addition of the fluorescent lipids, the gold stripes appear dark while the bright background is due to the known auto-fluorescence of the glass substrate (Fig.11.2a). Because of potentially different illumination conditions, a comparison between the fluorescence intensities may be only valid within the same image and not between two separate fluorescence images. To see what is the effect of the gold nanoparticles that were immobilized on the sample surface, two samples were prepared under identical conditions but one of them had no gold nanorods (NR) adsorbed on the

surface. After incubation with fluorescently labeled lipid vesicles and subsequent washing, the samples were observed under the fluorescence microscope. The images are shown in Fig. 11.3, for both samples, with NR (a) and without NR (b).

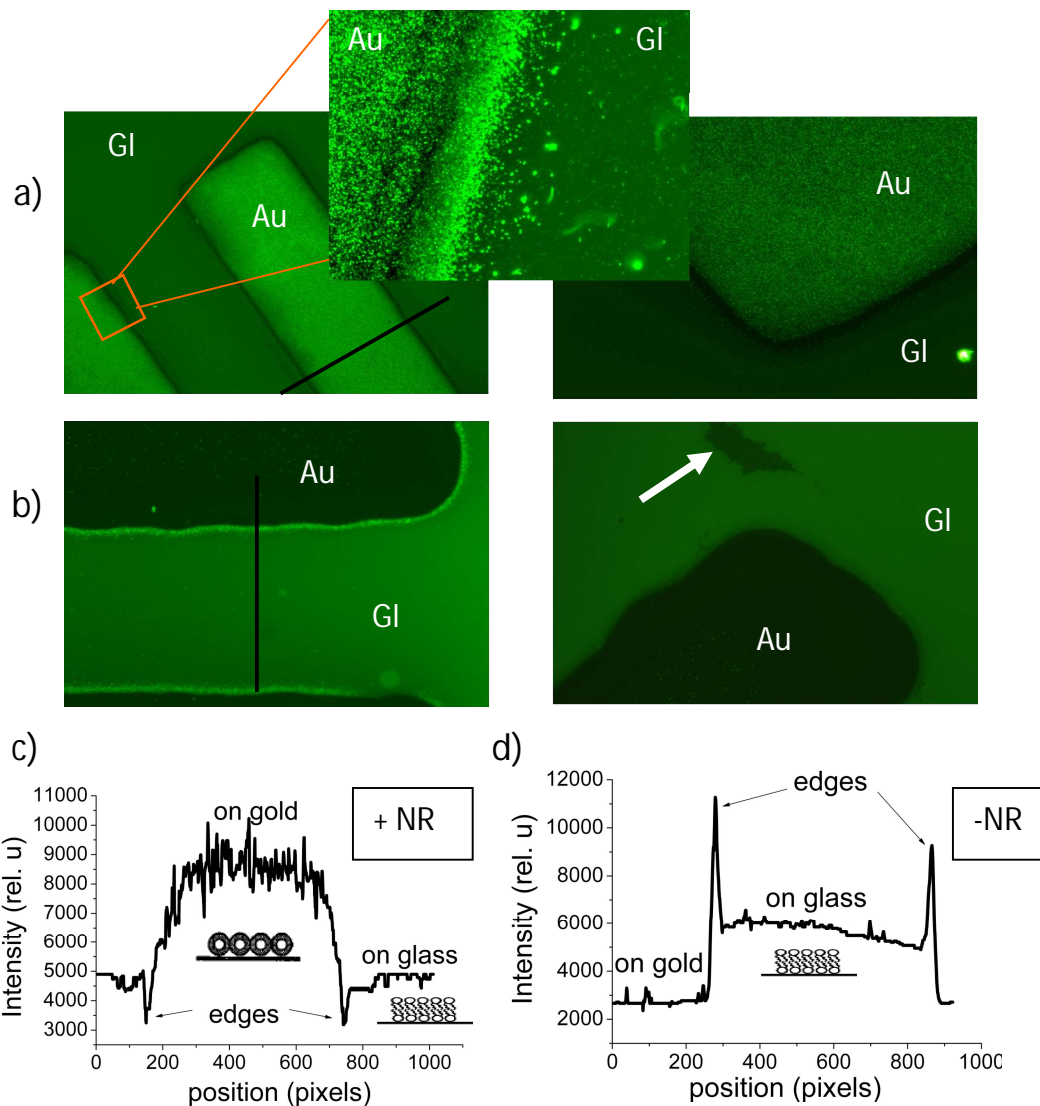


Fig.11.3 a) Fluorescent images of the sample prepared with gold nanorods (+NR) after incubation with lipid vesicles. The gold stripes are $500\mu\text{m}$ wide, the images are acquired with water immersed objectives: 10x (left), 40x (right), 100x (the inset); b) Fluorescent images of the sample prepared without gold nanorods (-NR) after incubation with lipid vesicles. The gold stripes are $100\mu\text{m}$ wide, the images are acquired with a 40x water immersed objective. The white arrow points to a defect into the lipid bilayer that is formed on the glass surface demonstrating that the fluorescent signal is given by the fluorescent lipids and not by the glass autofluorescence as it was the case shown in Fig.11.2a. "Au" and "Gl" are used to mark the gold stripes and the glass substrates respectively; c) Intensity profile of the fluorescence (relative units) along the line cross section drawn in (a) on the sample prepared with gold nanorods (+NR); d) Intensity profile of the fluorescence (relative units) along the line cross section drawn in (b) on the sample prepared without gold nanorods (-NR).

Following the incubation with lipid vesicles and the subsequent washing, no fluorescent signal was detected from the gold stripes of the sample that was prepared without gold nanorods. The gold areas appear dark in comparison to the fluorescence of the glass substrates on that the lipid vesicles were spread into a lipid bilayer. By contrast, the gold stripes of the sample prepared with gold nanorods on top exhibit a strong fluorescence signal, considerably higher than that of the glass substrate on which a lipid bilayer is formed. Most probably this increased fluorescence is due to fluorescent lipid vesicles that adhere without fusion on the gold surface, the topography of which was modified by previously adsorbed gold nanoparticles.

A detail fluorescence image (inset in Fig. 11.3a) recorded with a very sensitive camera through a 100x water immersed objective shows on the gold substrate not only a considerably higher intensity but also a granular distribution of the fluorescent signal as compared to the signal from the glass substrate. This may suggest that the adhered vesicles on gold may, possibly, cover incompletely the surface, maintaining a certain distance one from the other. However, the image is taken (for comparison reasons) very close to the stripe edge and because of the high magnification, only a very small area is visible. It may be possible that incomplete coverage with lipid vesicles is specific or mostly visible at the edges of the gold stripes where the nano-scale topography and the roughness achieved during the thermal deposition of gold may differ to a certain extent from that obtained further from the edges.

Formation of a continuous and fluid lipid bilayer on the glass substrates with or without gold nanorods is proved by the complete recovery of the fluorescence after photobleaching in FRAP experiments (Fig.11.4). The measured diffusion coefficients of the fluorescent lipids on both samples are in the same range, $D=4.5\pm 1.3\mu\text{m}^2/\text{s}$, in agreement with the values already obtained in Section 8.2.1.

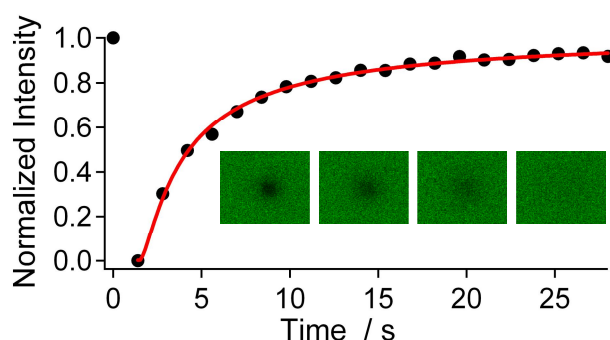


Fig. 11.4 Time course recovery of the fluorescence intensity inside of the photobleached spot during FRAP experiments on the lipid membranes spread on the glass substrate with gold nanorods.

The differences in the fluorescent signals observed on glass and gold areas of each sample (with and without NR) are well demonstrated by the intensity profiles (arbitrary units) of the cross line sections shown in Fig.11.3c) and d). On the sample prepared without NR, the intensity of the fluorescent lipid bilayer formed on glass is two times higher than the average signal received from the gold surface (which is in fact a residual

signal). One can observe in the right fluorescence image shown in Fig.11.3b that the defect in the lipid bilayer formed on the glass substrate appears as dark as the gold stripes. However, on the planar gold areas one can observe, at high imaging magnification, isolated bright spots as a sign that, accidentally, some lipid vesicle may still adhere to the surface. One can not exclude even the hypothesis that, to a certain extent, as former literature reported¹⁴², some lipid vesicles adhered and fused with the planar gold surface that may be eventually covered in part with immobile lipid bilayers. Nevertheless, no fluorescence from such membranes would be visible due to the proximity with the gold surface which is known to quench the fluorescence on a Förster radius of about 5nm, exactly the average thickness of a lipid bilayer. In most cases of the samples prepared without NR, the fluorescence intensity is increased along the edges of the gold stripes, most probably because, due to the change in the surface topography (20nm out of plane, comparable let say with the average diameter of the nanorods), the adsorption of vesicles, but not fusion, is facilitated.

Oppositely to the samples prepared without NR, the intensity cross section obtained from the fluorescent image of the sample prepared with NR exhibits increased fluorescence across the gold stripe, the average signal being about two times higher than the fluorescence signal of the lipid bilayer formed on the glass (Fig.11.3c). This increased fluorescence is most probably due to the intact lipid vesicles that adhere on the planar gold surface with gold nanorods on top. The granular aspect of the fluorescence emitted from the gold areas (inset in Fig.11.3a) and also the larger local fluctuations of the intensity cross section in the gold region than in the glass region support the hypothesis of intact adsorption of lipid vesicles on gold. It is not possible to estimate, however, from the intensity of the fluorescence signal, what is the degree of surface coverage with lipid vesicles. This is mainly due to the fact that the bottom part of the adhered lipid vesicles comes very close into contact with the gold substrate, and the contact area may even increase if the vesicles tend to adopt a flattened shape. For these reasons, a certain percent of the potential fluorescence is quenched (over a distance of 5-10nm from the substrate) due to the proximity to the gold interface. It is also known that fluorophors that are placed at an appropriate distance from the gold surface (nanorods as well) exhibit enhanced fluorescence under certain conditions (namely an overlap of the absorption or emission band of the dye with the SP resonance). If these conditions are fulfilled, the fluorescent lipids from the top part of the adhered vesicles may exhibit enhanced fluorescence. On a scale of few tens of nanometers, quenching and enhancing of the fluorescence would be therefore dependent on the relative position of the fluorophors in the lipid vesicles.

A direct comparison between the different adhesive affinities of the lipid vesicles towards flat gold surfaces and gold surfaces decorated with gold nanorods was possible by introducing the second level of sample structuring. On the first level, planar gold stripes (20nm thick, 100µm wide) were formed on the glass substrates by thermal evaporation. On the second level, via micromolding in capillaries (in a similar manner as lipid membranes are microstructured on solid supports - see section 3.5), gold nanorods were immobilized on the sample surface according to the pattern (stripes of 15µm width) formed by the employed PDMS stamps. After incubation with lipid vesicles and subsequent washing, the samples were examined in DF and fluorescence microscopy.

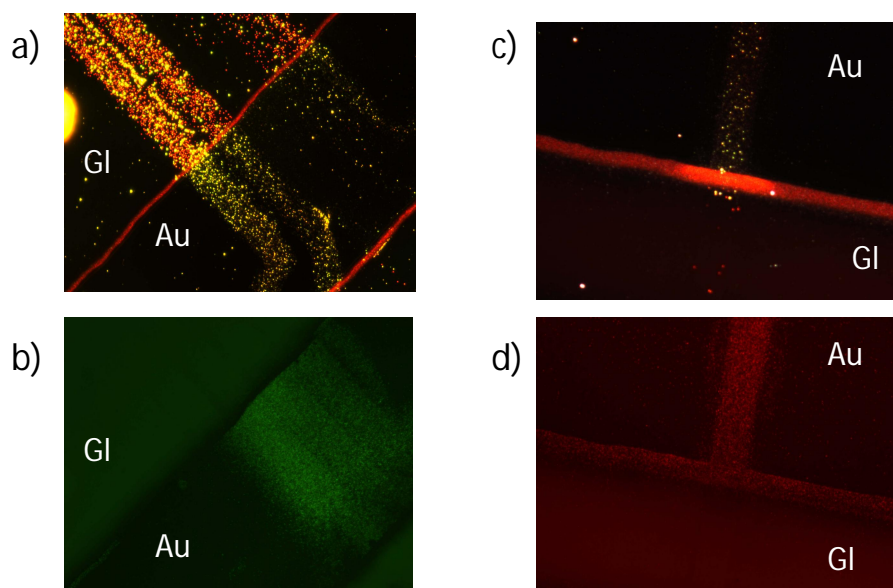


Fig. 11.5 (a) and (b) are, respectively, DF and fluorescent images of the same area selected on a two levels structured sample after incubation with lipid vesicles that were labeled with β -Bodipy C12-HPC (green fluorescence). (c) and (d) are, respectively, DF and fluorescent images of the same area selected on a two levels structured sample after incubation with lipid vesicles that were labeled with sulforhodamine-DHPE (red fluorescence). "Au" and "Gl" are used to mark the gold and the glass substrates respectively. Distinct patterns (stripes of $15\mu\text{m}$ width) of immobilized gold nanorods are visible in the DF images. On the gold substrates, they correspond in the fluorescence images to the areas of intense fluorescence

The same experiment was performed with lipid vesicles that were fluorescently labeled with β -Bodipy C12-HPC (blue excitation, green emission) and with lipid vesicles of the same lipid composition but labeled with sulforhodamine-DHPE (green excitation, blue emission). DF and fluorescence images taken from the same area of the samples are shown in Fig.11.5. In both cases an increased fluorescence signal is selectively detected only from the regions on the gold areas that were decorated with gold nanorods (as indicated by DF images). The rest of the gold areas, which are flat, appear dark. A weaker fluorescence signal is also observable from the lipid bilayers formed on the glass substrate. These experiments confirm the previous observation that lipid vesicles adhere preferentially to the gold substrates whose surface topography was modified by the adsorption of gold nanoparticles.

The surface number density of the nanorods seems to be important for the adhesion of the liposomes. When particles form large agglomerates or cluster on the gold substrate, the adherence of the vesicles is hindered. This aspect is especially observable on samples with two levels of structures (like those shown in Fig.11.5) because during the second level of structuring (micromolding of particles suspension into capillaries) is relatively easy to obtain agglomerations of nanorods on the surface due to the fact that the fluid flow is perturbed by the inappropriate sealing between the support and the PDMS stamp. Some studies that have approached the topic of interaction between the lipid vesicles and gold substrates issued the hypothesis of image charge effects¹⁴² according to that

charged vesicles should show a stronger attraction to gold surfaces than the uncharged vesicles. The preferential adhesion of lipid vesicles to the gold surfaces exhibiting modified nanoscale topography was not dependent on the charged lipid content of the vesicles. Similar experimental results were obtained when, instead of negatively charged lipid vesicles, pure zwitterionic (POPC) lipid vesicles were used (data not shown).

11.4 Conclusions

Many applications or experimental techniques require the formation of monolayers of lipid vesicles on gold substrates. This is because lipid vesicles may serve for instance as good media for embedding proteins that need to be further studied while gold is known for its conductive and optical properties (well exploited in experimental techniques such as QCM or SPR)

Although extensive literature exists so far in relation to the adhesion of lipid vesicles and bilayer formation on functionalized gold substrates, little is known and contradictory results were reported for unmodified (chemically untreated) gold substrates.

I have shown in this chapter that without any chemical treatment, topographic modifications on a nanometer scale of gold surfaces change drastically the adhesion properties of gold for large unilamellar lipid vesicles. The evidence is given by an increased fluorescent signal acquired from the fluorescently labeled liposomes that preferentially adhered and remain intact on the gold substrates, the topography of which has been previously modified by adsorption of gold nanorods. This phenomenon was observed equally for charged (4:1POPC/POPS) and zwitterionic (POPC) lipid vesicles. When particles form large agglomerates or cluster on the gold substrate, the adherence of lipid vesicles is hindered.

The possibility to form monolayers of intact lipid vesicles on gold substrates decorated with gold nanoparticles may present an additional interest due to the potential sensing applications that involve metal enhanced fluorescence mechanisms. By modifying the aspect ratio of the nanorods, their SPR band can be tuned in accordance with the excitation or emission band of the employed fluorophore, while the size of the lipid vesicles may be chosen to fit the optimal distance required for having maximal fluorescence enhancement.

Summary

Adsorption of proteins and lateral organization of multicomponent lipid membranes are approached in this work from two different perspectives. On one side, new insights are brought about the domain formation and the reversibility of binding of specific proteins using conventional experimental techniques such as AFM, ellipsometry and fluorescence microscopy. On the other side, a new, nanosized, and addressable sensing platform is proposed for the detection of membrane-mediated interactions based on less conventional sensing properties of plasmonic particles. This is the first experimental approach that combines successfully the lipid membranes to the concept of LSPR sensing with gold particles. Motivation for single particle detection of membrane protein interactions is additionally conferred by the possibility to screen this interaction over the lateral inhomogeneities of the membrane as a consequence of the highly localized sensitivity of detection.

In the first part of this work, atomic force microscopy is employed in order to analyze the formation of bilayer patches on oxidized silicon substrates and to investigate the dependency of lateral phase separation as a function of membrane composition. It is shown that the tendency for phase segregation in gel and fluid phase lipid mixtures is accentuated in the presence of divalent calcium ions for membranes containing anionic lipids as compared to neutral bilayers. The occurrence of "entropically trapped" nano-domains imaged in mixtures of 1:1 DPPC/POPC lipids is discussed.

Adsorption of annexin A1 on multicomponent lipid bilayers is investigated by means of AFM imaging. Annexin A1 proves to adsorb irreversibly in a Ca^{2+} dependent manner on PS enriched lipid domains. Ternary lipid bilayers containing mixtures of charged and uncharged lipids in gel and fluid phase were employed in order to discriminate between calcium-induced and potentially protein-induced lateral segregation of lipids. It is clearly shown that in homogenous membranes with low anionic lipid content AnnexinA1 can induce clustering of acidic lipids into areas with high binding affinity. The kinetics and calcium dependency of prothrombin adsorption to negatively charged lipid membranes are characterized by means of ellipsometry.

In the second part of this work (Chaps.8-9), the proof of concept for the construction of an optical biosensor using gold nanorods as sensing elements for monitoring lipid membrane mediated recognition events is presented. To this end, the plasmonic particles were immobilized on glass substrates and covered completely with lipid membranes such that the plasmon resonance shifts caused by protein induced changes in the dielectric properties at the membrane interface could be detected with single particle spectroscopy. A detailed analysis of the nanorods deposition on hydrophilic and amine-functionalized glass surfaces is performed in relation to various factors (such as the pH, ionic strength and concentration of the colloidal suspension, incubation time) in

order to find the optimal conditions for obtaining a homogenous distribution of particles at the desired surface number density. Noteworthy, one can easily tune the affinity of gold particles for amine-functionalized surfaces by adjusting the pH of the colloidal solution. The possibility of successfully draping lipid membranes over the gold particles immobilized on the glass substrate is demonstrated with complementary techniques of investigation such as phase imaging AFM, fluorescence microscopy (including FRAP) and single particle spectroscopy. The functionality and sensitivity of the proposed sensing platform is unequivocally certified by the resonance shifts of the plasmonic particles that were individually interrogated with dark field spectroscopy upon the adsorption of streptavidin to biotinylated lipid membranes.

As an alternative to the 2D array of gold nanorods, plasmonic gold nanostructures on glass substrates are built by means of colloidal nanolithography. Technical issues mainly related to the optimization of the mask deposition conditions are successfully addressed such that extended arrays of nanoholes or truncated tetrahedron shaped particles are achieved.

In Chap. 10, corroborated evidence from AFM and fluorescence images recorded during the incipient activity of phospholipase PLA₂ on solid supported lipid bilayers demonstrate that the hydrolysis of lipids is initiated faster at the sites where the membrane bends over irregularities such as nanoparticles immobilized on the substrate. It is therefore confirmed the hypothesis of increased hydrolytic activity of PLA₂ on highly curved regions of membranes due to facilitated access of the lipase to the cleavage site of the lipids.

The last part of this work (Chap.11) is a report on the experimental finding that topographic modifications on a nanometer scale of gold surfaces change drastically the adhesion properties for large unilamellar lipid vesicles. This observation unravels, at least in part, the controversial question about the behavior of lipid vesicles on bare gold substrates. The possibility of assembling monolayers of lipid vesicles on chemically untreated gold substrates decorated with gold nanorods opens new perspectives for biosensing applications that involve the radiative decay engineering of the plasmonic particles.

Bibliography

1. Brian, A. A. & McConnell, H. M. Allogeneic Stimulation of Cyto-Toxic T-Cells by Supported Planar Membranes. *Proceedings of the National Academy of Sciences of the United States of America-Biological Sciences* 81, 6159-6163 (1984).
2. McConnell, H. M., Watts, T. H., Weis, R. M. & Brian, A. A. Supported Planar Membranes in Studies of Cell-Cell Recognition in the Immune-System. *Biochimica Et Biophysica Acta* 864, 95-106 (1986).
3. Tanaka, M. & Sackmann, E. Polymer-supported membranes as models of the cell surface. *Nature* 437, 656-663 (2005).
4. Schmitt, E. K., Nurnabi, M., Bushby, R. J. & Steinem, C. Electrically insulating pore-suspending membranes on highly ordered porous alumina obtained from vesicle spreading. *Soft Matter* 4, 250-253 (2008).
5. Mornet, S., Lambert, O., Duguet, E. & Brisson, A. The formation of supported lipid bilayers on silica nanoparticles revealed by cryoelectron microscopy. *Nano Letters* 5, 281-285 (2005).
6. Roiter, Y. et al. Interaction of nanoparticles with lipid membrane. *Nano Letters* 8, 941-944 (2008).
7. Luthgens, E. & Janshoff, A. Equilibrium coverage fluctuations: A new approach to quantify reversible adsorption of proteins. *Chemphyschem* 6, 444-448 (2005).
8. Coban, O., Popov, J., Burger, M., Vobornik, D. & Johnston, L. J. Transition from nanodomains to microdomains induced by exposure of lipid monolayers to air. *Biophysical Journal* 92, 2842-2853 (2007).
9. Ramachandran, S., Laradji, M. & Kumar, P. B. S. Lateral Organization of Lipids in Multi-component Liposomes. *Journal of the Physical Society of Japan* 78 (2009).
10. Kiessling, V., Wan, C. & Tamm, L. K. Domain coupling in asymmetric lipid bilayers. *Biochimica Et Biophysica Acta-Biomembranes* 1788, 64-71 (2009).
11. Simons, K. & Ikonen, E. Functional rafts in cell membranes. *Nature* 387, 569-572 (1997).
12. Pike, L. J. The challenge of lipid rafts. *Journal of Lipid Research* 50, S323-S328 (2009).
13. Alberts, B. et al. *Molecular biology of the cell* (Garland Publishing, Inc. , New York & London, 1994).
14. Richter, R. P., Berat, R. & Brisson, A. R. Formation of solid-supported lipid bilayers: An integrated view. *Langmuir* 22, 3497-3505 (2006).
15. Castellana, E. T. & Cremer, P. S. Solid supported lipid bilayers: From biophysical studies to sensor design. *Surface Science Reports* 61, 429-444 (2006).
16. Czeslik, C. Desired and undesired - Protein adsorption on solid interfaces. *Chemie in Unserer Zeit* 40, 238-245 (2006).

17. Schaaf, P., Voegel, J. C. & Senger, B. Irreversible deposition/adsorption processes on solid surfaces. *Annales De Physique* 23, 1-+ (1998).
18. Adamczyk, Z., Siwek, B. & Zembala, M. Kinetics of Localized Adsorption of Particles on Homogeneous Surfaces. *Journal of Colloid and Interface Science* 151, 351-369 (1992).
19. Adamczyk, Z., Siwek, B., Zembala, M. & Weronki, P. Kinetics of Localized Adsorption of Colloid Particles. *Langmuir* 8, 2605-2610 (1992).
20. Flory, P. J. Intramolecular reaction between neighboring substituents of vinyl polymers. *J. Am. Chem. Soc.* 61, 1518-1521 (1939).
21. Widom, B. Some Topics in Theory of Fluids. *Journal of Chemical Physics* 39, 2808-& (1963).
22. Dickman, R., Wang, J. S. & Jensen, I. Random Sequential Adsorption - Series and Virial Expansions. *Journal of Chemical Physics* 94, 8252-8257 (1991).
23. Ramsden, J. J., Bachmanova, G. I. & Archakov, A. I. Kinetic Evidence for Protein Clustering at a Surface. *Physical Review E* 50, 5072-5076 (1994).
24. Adamczyk, Z., Siwek, B., Szyk, L. & Zembala, M. Fluctuations in the number of particles adsorbed under the influence of diffusion and flow. *Journal of Chemical Physics* 105, 5552-5561 (1996).
25. Adamczyk, Z. & Weronki, P. Density fluctuations in irreversible adsorption processes: Hard ellipses in two dimensions. *Journal of Chemical Physics* 107, 3691-3697 (1997).
26. Jung, L. S., Campbell, C. T., Chinowsky, T. M., Mar, M. N. & Yee, S. S. Quantitative interpretation of the response of surface plasmon resonance sensors to adsorbed films. *Langmuir* 14, 5636-5648 (1998).
27. Bohren, C. F. & Huffman, D. r. Absorption and scattering of light by small particles (Wiley-VCH Verlag GmbH & Co. KGaA, 2004).
28. Cole, R. M. et al. Understanding plasmons in nanoscale voids. *Nano Letters* 7, 2094-2100 (2007).
29. Maier, A. S. Plasmonics: Fundamentals and Applications (Springer Science+Buisness Media LLC, 2007).
30. Prikulis, J., Hanarp, P., Olofsson, L., Sutherland, D. & Kall, M. Optical spectroscopy of nanometric holes in thin gold films. *Nano Letters* 4, 1003-1007 (2004).
31. Rindzevicius, T. et al. Plasmonic sensing characteristics of single nanometric holes. *Nano Letters* 5, 2335-2339 (2005).
32. Dahlin, A. et al. Localized surface plasmon resonance sensing of lipid-membrane-mediated biorecognition events. *Journal of the American Chemical Society* 127, 5043-5048 (2005).
33. Rindzevicius, T. et al. Nanohole plasmons in optically thin gold films. *Journal of Physical Chemistry C* 111, 1207-1212 (2007).
34. Link, S. & El-Sayed, M. A. Shape and size dependence of radiative, non-radiative and photothermal properties of gold nanocrystals. *International Reviews in Physical Chemistry* 19, 409-453 (2000).
35. Kreibig, U. & Vollmer, M. Optical properties of metal clusters (eds. Gonser, U., Osgood, R. M., Panish, M. B. & Sakaki, H.) (Berlin -Heidelberg, 1995).

-
36. Jensen, T., Kelly, L., Lazarides, A. & Schatz, G. C. Electrodynamics of noble metal nanoparticles and nanoparticle clusters. *Journal of Cluster Science* 10, 295-317 (1999).
 37. Haes, A. J. & Van Duyne, R. P. Nanoscale optical biosensors based on localized surface plasmon resonance spectroscopy. *Plasmonics: Metallic Nanostructures and Their Optical Properties* 5221, 47-58 232 (2003).
 38. Haes, A. J., Zou, S. L., Schatz, G. C. & Van Duyne, R. P. A nanoscale optical biosensor: The long range distance dependence of the localized surface plasmon resonance of noble metal nanoparticles. *Journal of Physical Chemistry B* 108, 109-116 (2004).
 39. Haes, A. J., Zou, S. L., Schatz, G. C. & Van Duyne, R. P. Nanoscale optical biosensor: Short range distance dependence of the localized surface plasmon resonance of noble metal nanoparticles. *Journal of Physical Chemistry B* 108, 6961-6968 (2004).
 40. Binnig, G., Quate, C. F. & Gerber, C. Atomic Force Microscope. *Physical Review Letters* 56, 930-933 (1986).
 41. Ducharme, D., Max, J. J., Salesse, C. & Leblanc, R. M. Ellipsometric Study of the Physical States of Phosphatidylcholines at the Air-Water-Interface. *Journal of Physical Chemistry* 94, 1925-1932 (1990).
 42. Howland, M. C., Szmodis, A. W., Sanii, B. & Parikh, A. N. Characterization of physical properties of supported phospholipid membranes using imaging ellipsometry at optical wavelengths. *Biophysical Journal* 92, 1306-1317 (2007).
 43. Szmodis, A. W. et al. Direct visualization of phase transition dynamics in binary supported phospholipid bilayers using imaging ellipsometry. *Soft Matter* 4, 1161-1164 (2008).
 44. Stroumpoulis, D., Parra, A. & Tirrell, M. A kinetic study of vesicle fusion on silicon dioxide surfaces by ellipsometry. *Aiche Journal* 52, 2931-2937 (2006).
 45. Tompkins, H. G. *A User's guide to Ellipsometry* (Academic Press, Inc., San Diego, 1993).
 46. Becker, J., Schubert, O. & Sonnichsen, C. Gold nanoparticle growth monitored in situ using a novel fast optical single-particle spectroscopy method. *Nano Letters* 7, 1664-1669 (2007).
 47. Israelachvili, J. N. *Intermolecular and surface forces* (Academic press inc, London, 1992).
 48. Rosengarth, A., Rosgen, J., Hinz, H. J. & Gerke, V. A comparison of the energetics of annexin I and annexin V. *Journal of Molecular Biology* 288, 1013-1025 (1999).
 49. Hendrickson, W. A. et al. Crystal-Structure of Core Streptavidin Determined from Multiwavelength Anomalous Diffraction of Synchrotron Radiation. *Proceedings of the National Academy of Sciences of the United States of America* 86, 2190-2194 (1989).
 50. Schmidt, A., Spinke, J., Bayerl, T., Sackmann, E. & Knoll, W. Streptavidin Binding to Biotinylated Lipid Layers on Solid Supports - a Neutron Reflection and Surface-Plasmon Optical Study. *Biophysical Journal* 63, 1385-1392 (1992).
 51. Reiter, R., Motschmann, H. & Knoll, W. Ellipsometric Characterization of Streptavidin Binding to Biotin-Functionalized Lipid Monolayers at the Water Air Interface. *Langmuir* 9, 2430-2435 (1993).

52. Perez-Juste, J., Pastoriza-Santos, I., Liz-Marzan, L. M. & Mulvaney, P. Gold nanorods: Synthesis, characterization and applications. *Coordination Chemistry Reviews* 249, 1870-1901 (2005).
53. Muskens, O. L. et al. Quantitative absorption spectroscopy of a single gold nanorod. *Journal of Physical Chemistry C* 112, 8917-8921 (2008).
54. Nikoobakht, B. & El-Sayed, M. A. Preparation and growth mechanism of gold nanorods (NRs) using seed-mediated growth method. *Chemistry of Materials* 15, 1957-1962 (2003).
55. Chiu, P. H., Huang, C. J., Wang, Y. H. & Chen, C. H. Synthesis of Gold Nanodogbones by the Seed Mediated Growth Method with Addition of Vitamin C Solvent. *Smart Materials* 55-57, 665-668 950 (2008).
56. Mayer, L. D., Hope, M. J. & Cullis, P. R. Vesicles of variable sizes produced by a rapid extrusion procedure. *Biochimica et Biophysica Acta* 858, 161-168 (1986).
57. Bagatolli, L. A., Parasassi, T. & Gratton, E. Giant phospholipid vesicles: comparison among the whole lipid sample characteristics using different preparation methods - A two photon fluorescence microscopy study. *Chemistry and Physics of Lipids* 105, 135-147 (2000).
58. Moscho, A., Orwar, O., Chiu, D. T., Modi, B. P. & Zare, R. N. Rapid preparation of giant unilamellar vesicles. *Proceedings of the National Academy of Sciences of the United States of America* 93, 11443-11447 (1996).
59. Janshoff, A. & Kunneke, S. Micropatterned solid-supported membranes formed by micromolding in capillaries. *European Biophysics Journal with Biophysics Letters* 29, 549-554 (2000).
60. Kastl, K. et al. Partially reversible adsorption of annexin A1 on POPC/POPS bilayers investigated by QCM measurements, SFM, and DMC simulations. *Chembiochem* 7, 106-115 (2006).
61. Seu, K. J. et al. Effect of surface treatment on diffusion and domain formation in supported lipid bilayers. *Biophysical Journal* 92, 2445-2450 (2007).
62. Seifert, U. & Lipowsky, R. Adhesion of Vesicles. *Physical Review A* 42, 4768-4771 (1990).
63. Reviakine, I. & Brisson, A. Formation of supported phospholipid bilayers from unilamellar vesicles investigated by atomic force microscopy. *Langmuir* 16, 1806-1815 (2000).
64. Reviakine, I., Simon, A. & Brisson, A. Effect of Ca²⁺ on the morphology of mixed DPPC-DOPS supported phospholipid bilayers. *Langmuir* 16, 1473-1477 (2000).
65. Hill, T. L. *An introduction to statistical thermodynamics* (Dover Publications, Inc., New York, 1986).
66. Kuzmin, P. I., Akimov, S. A., Chizmadzhev, Y. A., Zimmerberg, J. & Cohen, F. S. Line tension and interaction energies of membrane rafts calculated from lipid splay and tilt. *Biophysical Journal* 88, 1120-1133 (2005).
67. de Almeida, R. F. M., Loura, L. M. S., Fedorov, A. & Prieto, M. Lipid rafts have different sizes depending on membrane composition: A time-resolved fluorescence resonance energy transfer study. *Journal of Molecular Biology* 346, 1109-1120 (2005).

-
68. Tokumasu, F., Jin, A. J., Feigenson, G. W. & Dvorak, J. A. Nanoscopic lipid domain dynamics revealed by atomic force microscopy. *Biophysical Journal* 84, 2609-2618 (2003).
 69. Pike, L. J. Rafts defined: a report on the Keystone Symposium on Lipid Rafts and Cell Function. *Journal of Lipid Research* 47, 1597-1598 (2006).
 70. Perretti, M. & Flower, R. J. Annexin 1 and the biology of the neutrophil. *Journal of Leukocyte Biology* 76, 25-29 (2004).
 71. Futter, C. E., Felder, S., Schlessinger, J., Ullrich, A. & Hopkins, C. R. Annexin-I Is Phosphorylated in the Multivesicular Body during the Processing of the Epidermal Growth-Factor Receptor. *Journal of Cell Biology* 120, 77-83 (1993).
 72. Francis, J. W., Balazovich, K. J., Smolen, J. E., Margolis, D. I. & Boxer, L. A. Human Neutrophil Annexin-I Promotes Granule Aggregation and Modulates Ca²⁺-Dependent Membrane-Fusion. *Journal of Clinical Investigation* 90, 537-544 (1992).
 73. McNeil, A. K., Rescher, U., Gerke, V. & McNeil, P. L. Requirement for annexin A1 in plasma membrane repair. *Journal of Biological Chemistry* 281, 35202-35207 (2006).
 74. Rintala-Dempsey, A. C., Rezvanpour, A. & Shaw, G. S. S100-annexin complexes - structural insights. *Febs Journal* 275, 4956-4966 (2008).
 75. Schwalbe, R. A. et al. Protein Structural Requirements and Properties of Membrane-Binding by Gamma-Carboxyglutamic Acid-Containing Plasma-Proteins and Peptides. *Journal of Biological Chemistry* 264, 20288-20296 (1989).
 76. Zwaal, R. F. A., Comfurius, P. & Bevers, E. M. Lipid-protein interactions in blood coagulation. *Biochimica Et Biophysica Acta-Reviews on Biomembranes* 1376, 433-453 (1998).
 77. Resnick, R. M. & Nelsestuen, G. L. Prothrombin-Membrane Interaction - Effects of Ionic-Strength, Ph, and Temperature. *Biochemistry* 19, 3028-3033 (1980).
 78. Lim, T. K., Bloomfield, V. A. & Nelsestuen, G. L. Structure of Prothrombin - Blood-Clotting Factor-X-Membrane Complexes. *Biochemistry* 16, 4177-4181 (1977).
 79. Janshoff, A., Ross, M., Gerke, V. & Steinem, C. Visualization of annexin I binding to calcium-induced phosphatidylserine domains. *Chembiochem* 2, 587-+ (2001).
 80. Mayer, L. D. & Nelsestuen, G. L. Calcium-Induced and Prothrombin-Induced Lateral Phase-Separation in Membranes. *Biochemistry* 20, 2457-2463 (1981).
 81. Faiss, S., Kastl, K., Janshoff, A. & Steinem, C. Formation of irreversibly bound annexin A1 protein domains on POPC/POPS solid supported membranes. *Biochimica Et Biophysica Acta-Biomembranes* 1778, 1601-1610 (2008).
 82. Nelsestuen, G. L. Role of Gamma-Carboxyglutamic Acid - Unusual Protein Transition Required for Calcium-Dependent Binding of Prothrombin to Phospholipid. *Journal of Biological Chemistry* 251, 5648-5656 (1976).
 83. Chen, Q. & Lentz, B. R. Fluorescence resonance energy transfer study of shape changes in membrane-bound bovine prothrombin and meizothrombin. *Biochemistry* 36, 4701-4711 (1997).
 84. Wei, G. J., Bloomfield, V. A., Resnick, R. M. & Nelsestuen, G. L. Kinetic and Mechanistic Analysis of Prothrombin-Membrane Binding by Stopped-Flow Light-Scattering. *Biochemistry* 21, 1949-1959 (1982).

85. Ito, K. J., Uehara, Y., Ushioda, S. & Ito, K. Servomechanism for locking scanning tunneling microscope tip over surface nanostructures. *Review of Scientific Instruments* 71, 420-423 (2000).
86. Staub, R., Alliaata, D. & Nicolini, C. Drift Elimination in the Calibration of Scanning Probe Microscopes. *Review of Scientific Instruments* 66, 2513-2516 (1995).
87. Yang, Q. M. & Jagannathan, S. Atomic force microscope-based nanomanipulation with drift compensation. *International Journal of Nanotechnology* 3, 527-544 (2006).
88. Kodera, N., Sakashita, M. & Ando, T. Dynamic proportional-integral-differential controller for high-speed atomic force microscopy. *Review of Scientific Instruments* 77, - (2006).
89. Manalis, S. R., Minne, S. C., Atalar, A. & Quate, C. F. Interdigital cantilevers for atomic force microscopy. *Applied Physics Letters* 69, 3944-3946 (1996).
90. Lapshin, R. V. & Obyedkov, O. V. Fast-Acting Piezoactuator and Digital Feedback Loop for Scanning Tunneling Microscopes. *Review of Scientific Instruments* 64, 2883-2887 (1993).
91. Egawa, A., Chiba, N., Homma, K., Chinone, K. & Muramatsu, H. High-speed scanning by dual feedback control in SNOM AFM. *Journal of Microscopy-Oxford* 194, 325-328 (1999).
92. Knebel, D., Amrein, M., Voigt, K. & Reichelt, R. A fast and versatile scan unit for scanning probe microscopy. *Scanning* 19, 264-268 (1997).
93. Schitter, G., Menold, P., Knapp, H. F., Allgower, F. & Stemmer, A. High performance feedback for fast scanning atomic force microscopes. *Review of Scientific Instruments* 72, 3320-3327 (2001).
94. Viani, M. B. et al. Fast imaging and fast force spectroscopy of single biopolymers with a new atomic force microscope designed for small cantilevers. *Review of Scientific Instruments* 70, 4300-4303 (1999).
95. Ando, T. et al. A high-speed atomic force microscope for studying biological macromolecules in action. *Japanese Journal of Applied Physics Part 1-Regular Papers Short Notes & Review Papers* 41, 4851-4856 (2002).
96. Mertz, J., Marti, O. & Mlynek, J. Regulation of a Microcantilever Response by Force Feedback. *Applied Physics Letters* 62, 2344-2346 (1993).
97. Antognozzi, M., Szczelkun, M. D., Humphris, A. D. L. & Miles, M. J. Increasing shear force microscopy scanning rate using active quality-factor control. *Applied Physics Letters* 82, 2761-2763 (2003).
98. Ando, T. et al. High-speed atomic force microscopy for studying the dynamic behavior of protein molecules at work. *Japanese Journal of Applied Physics Part 1-Regular Papers Brief Communications & Review Papers* 45, 1897-1903 (2006).
99. Ando, T. et al. High-speed AFM and nano-visualization of biomolecular processes. *Pflugers Archiv-European Journal of Physiology* 456, 211-225 (2008).
100. Gizeli, E. & Glad, J. Single-step formation of a biorecognition layer for assaying histidine-tagged proteins. *Analytical Chemistry* 76, 3995-4001 (2004).
101. Haynes, C. L. & Van Duyne, R. P. Nanosphere lithography: A versatile nanofabrication tool for studies of size-dependent nanoparticle optics. *Journal of Physical Chemistry B* 105, 5599-5611 (2001).

-
102. Swain, P. S. & Andelman, D. The influence of substrate structure on membrane adhesion. *Langmuir* 15, 8902-8914 (1999).
 103. Swain, P. S. & Andelman, D. Supported membranes on chemically structured and rough surfaces. *Physical Review E* 6305, - (2001).
 104. Benda, A. et al. How to determine diffusion coefficients in planar phospholipid systems by confocal fluorescence correlation spectroscopy. *Langmuir* 19, 4120-4126 (2003).
 105. Almeida, P. F. F. & Vaz, W. L. C. in *Structure and Dynamics of Membranes, Handbook of Biological Physics* (eds. R., L. & E., S.) (Elsevier/North-Holland, Amsterdam, 1995).
 106. Schram, V., Tocanne, J. F. & Lopez, A. Influence of Obstacles on Lipid Lateral Diffusion - Computer-Simulation of Frap Experiments and Application to Proteoliposomes and Biomembranes. *European Biophysics Journal* 23, 337-348 (1994).
 107. Radler, J., Strey, H. & Sackmann, E. Phenomenology and Kinetics of Lipid Bilayer Spreading on Hydrophilic Surfaces. *Langmuir* 11, 4539-4548 (1995).
 108. Cremer, P. S. & Boxer, S. G. Formation and spreading of lipid bilayers on planar glass supports. *Journal of Physical Chemistry B* 103, 2554-2559 (1999).
 109. Muresan, A. S. & Lee, K. Y. C. Shape evolution of lipid bilayer patches adsorbed on mica: An atomic force microscopy study. *Journal of Physical Chemistry B* 105, 852-855 (2001).
 110. Sanii, B., Smith, A. M., Butti, R., Brozell, A. M. & Parikh, A. N. Bending membranes on demand: Fluid phospholipid bilayers on topographically deformable substrates. *Nano Letters* 8, 866-871 (2008).
 111. Jonsson, M. P., Jonsson, P., Dahlin, A. B. & Hook, F. Supported lipid bilayer formation and lipid-membrane-mediated biorecognition reactions studied with a new nanoplasmonic sensor template. *Nano Letters* 7, 3462-3468 (2007).
 112. Schonherr, H., Johnson, J. M., Lenz, P., Frank, C. W. & Boxer, S. G. Vesicle adsorption and lipid bilayer formation on glass studied by atomic force microscopy. *Langmuir* 20, 11600-11606 (2004).
 113. Deserno, M. & Bickel, T. Wrapping of a spherical colloid by a fluid membrane. *Europhysics Letters* 62, 767-773 (2003).
 114. Lipowsky, R. & Seifert, U. Adhesion of Vesicles and Membranes. *Molecular Crystals and Liquid Crystals* 202, 17-25 (1991).
 115. Sackmann, E., Duwe, H. P. & Engelhardt, H. Membrane Bending Elasticity and Its Role for Shape Fluctuations and Shape Transformations of Cells and Vesicles. *Faraday Discussions*, 281-+ (1986).
 116. Deserno, M. Elastic deformation of a fluid membrane upon colloid binding. *Physical Review E* 69, - (2004).
 117. Biggs, S. & Mulvaney, P. Measurement of the Forces between Gold Surfaces in Water by Atomic-Force Microscopy. *Journal of Chemical Physics* 100, 8501-8505 (1994).
 118. Janshoff, A. & Steinem, C. Transport across artificial membranes - an analytical perspective. *Analytical and Bioanalytical Chemistry* 385, 433-451 (2006).
 119. Brochard, F. & Lennon, J. F. Frequency Spectrum of Flicker Phenomenon in Erythrocytes. *Journal De Physique* 36, 1035-1047 (1975).

120. Dimova, R. et al. A practical guide to giant vesicles. Probing the membrane nanoregime via optical microscopy. *Journal of Physics-Condensed Matter* 18, S1151-S1176 (2006).
121. Fricke, K. & Sackmann, E. Variation of Frequency-Spectrum of the Erythrocyte Flickering Caused by Aging, Osmolarity, Temperature and Pathological-Changes. *Biochimica Et Biophysica Acta* 803, 145-152 (1984).
122. Lo, C. M., Keese, C. R. & Giaever, I. Monitoring Motion of Confluent Cells in Tissue-Culture. *Experimental Cell Research* 204, 102-109 (1993).
123. Zeman, K., Engelhard, H. & Sackmann, E. Bending Undulations and Elasticity of the Erythrocyte-Membrane - Effects of Cell-Shape and Membrane Organization. *European Biophysics Journal* 18, 203-219 (1990).
124. Agero, U., Monken, C. H., Ropert, C., Gazzinelli, R. T. & Mesquita, O. N. Cell surface fluctuations studied with defocusing microscopy. *Physical Review E* 67, - (2003).
125. Gruhn, T., Franke, T., Dimova, R. & Lipowsky, R. Novel method for measuring the adhesion energy of vesicles. *Langmuir* 23, 5423-5429 (2007).
126. Radler, J. O., Feder, T. J., Strey, H. H. & Sackmann, E. Fluctuation Analysis of Tension-Controlled Undulation Forces between Giant Vesicles and Solid Substrates. *Physical Review E* 51, 4526-4536 (1995).
127. Sackmann, E. Supported membranes: Scientific and practical applications. *Science* 271, 43-48 (1996).
128. Nielsen, L. K., Risbo, J., Callisen, T. H. & Bjornholm, T. Lag-burst kinetics in phospholipase A(2) hydrolysis of DPPC bilayers visualized by atomic force microscopy. *Biochimica Et Biophysica Acta-Biomembranes* 1420, 266-271 (1999).
129. Bell, J. D. & Biltonen, R. L. Thermodynamic and Kinetic-Studies of the Interaction of Vesicular Dipalmitoylphosphatidylcholine with Agkistrodon-Piscivorus-Piscivorus Phospholipase-A2. *Journal of Biological Chemistry* 264, 225-230 (1989).
130. Hoyrup, P., Jorgensen, K. & Mouritsen, O. G. Phospholipase A(2) - An enzyme that is sensitive to the physics of its substrate. *Europhysics Letters* 57, 464-470 (2002).
131. Jain, M. K. & Berg, O. G. The Kinetics of Interfacial Catalysis by Phospholipase-A2 and Regulation of Interfacial Activation - Hopping Versus Scooting. *Biochimica Et Biophysica Acta* 1002, 127-156 (1989).
132. Mouritsen, O. G. et al. Activation of interfacial enzymes at membrane surfaces. *Journal of Physics-Condensed Matter* 18, S1293-S1304 (2006).
133. Leidy, C., Mouritsen, O. G., Jorgensen, K. & Peters, N. H. Evolution of a rippled membrane during phospholipase A(2) hydrolysis studied by time-resolved AFM. *Biophysical Journal* 87, 408-418 (2004).
134. Wacklin, H. P., Tiberg, F., Fragneto, G. & Thomas, R. K. Distribution of reaction products in phospholipase A(2) hydrolysis. *Biochimica Et Biophysica Acta-Biomembranes* 1768, 1036-1049 (2007).
135. Grandbois, M., Clausen-Schaumann, H. & Gaub, H. Atomic force microscope imaging of phospholipid bilayer degradation by phospholipase A(2). *Biophysical Journal* 74, 2398-2404 (1998).
136. Cherny, V. V., Sikharulidze, M. G., Mirsky, V. M. & Sokolov, V. S. Potential Distribution on the Lipid Bilayer-Membrane Due to the Phospholipase-A2 Activity. *Biologicheskie Membrany* 9, 733-740 (1992).

-
137. Richter, R., Mukhopadhyay, A. & Brisson, A. Pathways of lipid vesicle deposition on solid surfaces: A combined QCM-D and AFM study. *Biophysical Journal* 85, 3035-3047 (2003).
 138. Steinem, C., Janshoff, A., Ulrich, W. P., Sieber, M. & Galla, H. J. Impedance analysis of supported lipid bilayer membranes: A scrutiny of different preparation techniques. *Biochimica Et Biophysica Acta-Biomembranes* 1279, 169-180 (1996).
 139. Groves, J. T., Ulman, N., Cremer, P. S. & Boxer, S. G. Substrate-membrane interactions: Mechanisms for imposing patterns on a fluid bilayer membrane. *Langmuir* 14, 3347-3350 (1998).
 140. Li, M. et al. AFM studies of solid-supported lipid bilayers formed at a Au(111) electrode surface using vesicle fusion and a combination of Langmuir-Blodgett and Langmuir-Schaefer techniques. *Langmuir* 24, 10313-10323 (2008).
 141. Reimhult, E., Zach, M., Hook, F. & Kasemo, B. A multitechnique study of liposome adsorption on Au and lipid bilayer formation on SiO₂. *Langmuir* 22, 3313-3319 (2006).
 142. Sofou, S. & Thomas, J. L. Stable adhesion of phospholipid vesicles to modified gold surfaces. *Biosensors & Bioelectronics* 18, 445-455 (2003).
 143. Keller, C. A. & Kasemo, B. Surface specific kinetics of lipid vesicle adsorption measured with a quartz crystal microbalance. *Biophysical Journal* 75, 1397-1402 (1998).
 144. Reimhult, E., Hook, F. & Kasemo, B. Intact vesicle adsorption and supported biomembrane formation from vesicles in solution: Influence of surface chemistry, vesicle size, temperature, and osmotic pressure. *Langmuir* 19, 1681-1691 (2003).

A. Annexes

A1 Materials

Chemicals: Tris(hydroxymethyl)aminomethane hydrochloride (Tris/HCl), sodium chloride (NaCl), methanol, aqueous hydrofluoric acid HF (35 wt %), ammonia solution $\text{NH}_3 \cdot \text{H}_2\text{O}$ (28 %), calcium chloride ($\text{CaCl}_2 \cdot 2\text{H}_2\text{O}$), 3-(Ethoxydimethylsilyl)propylamine, sodium hydroxide (NaOH) and aqueous hydrogen peroxide H_2O_2 (35 wt %), Triton X-100, were purchased from Sigma (Deisenhofen, Germany).

Ethylene glycol tetraacetic acid (EGTA) and methanol was from Fluka (New-Ulm, Germany)

Chloroform, ethanol and hydrochloric acid (HCl) were from Carl Roth (Karlsruhe, Germany). All chemicals were high-grade and used without further purification.

Lipids: Sulforhodamine101 1,2-dihexadecanoyl-*sn*-glycero-3-phosphoethanolamine (Sulforhodamine - DHPE), 1-palmitoyl-2-oleoyl-*sn*-glycero-3-phosphocholine (POPC), 1-palmitoyl-2-oleoyl-*sn*-glycero-3-phospho-L-serine (POPS), 1,2-dipalmitoyl-*sn*-glycero-3-phosphocholine (DPPC), 1,2-dipalmitoyl-*sn*-glycero-3-phospho-L-serine (DPPS) were purchased from Avanti Polar Lipids (Alabaster, AL, USA);

N-((6-(biotinoyl)amino)hexanoyl)-1,2-dihexadecanoyl-*sn*-glycero-3-phosphoethanolamine, triethylammonium salt (Biotin-X-DHPE) and *N*-(biotinoyl)-1,2-dihexadecanoyl-*sn*-glycero-3-phosphoethanolamine, triethylammonium salt ((Biotin-DHPE)) were from Invitrogen.

Streptavidin from streptomyces avidinii and phospholipase PLA_2 from bee venom (*apis mellifera*) were purchased from Sigma-Aldrich (Germany) and bovine prothrombin from Enzyme Research Laboratories (UK).

Polished prime silicon wafers were from Wacker Siltronic (Munich, Germany), the glass cover slips were from Plano GmbH (Wetzlar, Germany) and Hi-Grade Mica sheets were from Ted Pella Inc. (California USA).

Poly(dimethylsiloxane) (PDMS, Sylgard 184) was purchased from DowCorning (Midland, MI, USA).

Gold nanorods were from Nanopartz (Analytical Inc, Salt Lake City, USA)

A2 Instruments and auxiliaries

Atomic Force Microscopy

Dimension 3100 Nanoscope IIIa	Veeco, Santa Barbara, CA (USA)
AFM-MFP 3D	Asylum Research
Nanowizard II BioAFM	PK Instruments, Berlin (Germany)
OMCL-RC800PSA cantilever	Olympus Optical Co., Tokio (Japan)
OMCL-TR400PSA cantilever	Olympus Optical Co., Tokio (Japan)
MLCT cantilever	Veeco, Santa Barbara, CA (USA)

Nanosphere Litography

Latex beads, sulfate modified polystyrene (30nm, 50nm, 100nm, 500nm)	Sigma Aldrich
White microsphere sulfate (58nm, 110nm, 506nm)	IDC, Portland USA
Vacuum Coating System	Balzers BAE 250

Dark Field Microscopy and Single Particle Spectroscopy

Transmission dark field microscope	Olympus
Transmission dark field microscope	Zeiss
Dark-field condenser (NA 1.2-1.4 or 0.75)	Zeiss, Olympus
Back illuminated CCD camera Pixis 400	Princeton Instruments
Electronically addressable LCD LC2002	Holoeye

Fluorescence Microscopy

Confocal fluorescence microscope	Leica Microsystems, Wetzlar
Upright fluorescence microscope	Olympus
ColorView II digital microcamera	Olympus

Ellipsometry

EP3-SW Ellipsometer	Nanofilm Technology, Göttingen
Objective, 20x/0.35 CF-Plan	Nikon, Tokio (Japan)
Liquid handling system	Nanofilm Technology, Göttingen
Liquid measuring chamber	Nanofilm Technology, Göttingen
Peristaltic pumps	Ismatec, Wertheim-Mondfeld

A3 Abbreviations

AFM	Atomic Force Microscopy
Chol	Cholesterol
CTAB	Cetyl Trimethyl Ammonium Bromide
CM	Contact Mode
CLSM	Confocal Laser Scanning Microscopy
DDA	Discrete Dipole Approximation
DFM	Dark Field Microscopy
DLPC	Dilauroyl phosphatidylcholine
DOPC	Dioleoyl phosphatidylcholine
DOPS	Dioleoyl phosphatidylserine
DPPC	Dipalmitoyl phosphatidylcholine
DPPS	Dipalmitoyl phosphatidylserine
EDSPA	3-(Ethoxydimethylsilyl)propylamine
EGTA	Ethylene Glycol Tetraacetic Acid
FRAP	Fluorescence Recovery after Photobleaching
GUV	Giant Unilamellar Vesicle
Gla	γ -carboxyglutamic acid
LSP	Localized Surface Plasmon
LSPR	Localised Surface Plasmon Resonance
LUV	Large Unilamellar Vesicle
MC	Monte Carlo
NTA	Nitrilotriacetic acid
NSL	Nanosphere Litography
PEG	Poly ethylene glycol
PLA ₂	Phospholipase A ₂
PDMS	Poly Dimethyl Siloxane
POPC	Palmitoyl Oleoyl Phosphatidylcholine
POPS	Palmitoyl Oleoyl Phosphatidylserine
ROI	Region of Interest
RSA	Random Sequential Adsorption
SEM	Scanning Electron Microscopy
SLB	Supported Lipid Bilayer
SPR	Surface Plasmon Resonance
SM	Sphingomyelin
SPS	Single Particle Spectroscopy
TEM	Transmission Electron Microscopy
TM	Tapping

